UNIVERSITY OF SOUTHAMPTON

Department of Physics

Faculty of Science

Photorefractives for Fast Optics

by

Mathew John Deer

A thesis submitted for the degree of Doctor of Philosophy

September 2006

Contents

UNIVERSITY OF SOUTHAMPTON

ABSTRACT

FACULTY OF SCIENCE

PHYSICS

Doctor of Philosophy

PHOTOREFRACTIVES FOR FAST OPTICS

By Mathew John Deer

This thesis describes an experimental and theoretical study into the nonlinear optical properties of novel photorefractive materials and devices. The focus of the work is centred on bringing together the attractive attributes of inorganic and organic materials in a single hybrid device and to increase the photorefractive effect that is available from either material alone.

Consequently three novel photorefractive devices have been developed that are suitable for use as frequency agile optical filters and exhibit greater contrast ratios than previous passive photorefractive materials. Small signal gain co-efficients of up to 1600cm^{-1} are demonstrated in these hybrid devices, compared to less than 20cm^{-1} in a single photorefractive window without any inorganic-organic hybridisation. The fundamental understanding in an inorganic photorefractive hybrid has also been advanced.

Acknowledgements

I would like to thank my supervisors Dr Malgosia Kaczmarek and Dr Ken McEwan for their constant support and assistance throughout this study, and the assistance of Dr Chris Wyres and Dr Gary Cook during the early stages of this project.

I would like to acknowledge Dr David Smith and Dr James Gates for collaborating on the atomic force microscope work discussed in chapter 4 and for many useful and humorous discussions. Also, Dr Andriy Dyadyusha for collaborating on the off axis experimental work discussed in chapter 4 and allowing me to use his laboratory at the drop of a hat.

I am indebted to Dr Richard Hollins, Dr Stephen Till, and Dr Phillip Milsom for their constant encouragement through all the lows and highs that have made this study so rewarding.

Finally, I am always indebted to my family and wife to be for their support.

Chapter 1 Introduction to photorefractive materials and devices

1.1 Background

This thesis describes an experimental and theoretical study into the nonlinear optical properties of novel photorefractive materials and devices. The term photorefractive refers to a class of materials in which possess both photoconduction and the electro-optic effect. The photorefractive effect was discovered in 1966 by Ashkin [1] at Bell Labs but it is still an active field of research and new ideas and materials are still under development today. The large nonlinear properties of photorefractive crystals observed at moderate laser powers in both the visible and infrared wavelength ranges demonstrated huge potential for coherent beam amplification, phase conjugation and optical data processing, and demonstration that the photorefractive effect could last for many months in some cases prompted the use of photorefractive crystals for high density optical storage [2].

This chapter is used to provide an historical review on the field of photorefraction and to put the work in this thesis into context. The physical processes that give rise to the photorefractive effect are described, then some of the resulting nonlinear optical effects such as optical damage, beam-fanning and two beam coupling are reviewed. A multitude of applications have been proposed for photorefractive materials and some of the most interesting concepts are described. Photorefraction was originally discovered in inorganic crystals and a review of the materials is included. However more recently [3, 14] photorefraction has been demonstrated in organic materials and this is an active field of research with polymer and liquid crystal materials under development. Both inorganic and organic material systems are important to the work presented in this thesis as a large proportion of this thesis is dedicated to demonstrating the advantages of combining these materials.

1.2 The photorefractive effect

In this section I will introduce the photorefractive effect by considering the response to the interference of two laser beams derived from the same coherent laser source. Photorefractive materials are both electro-optic and photoconductive. When the two coherent laser beams are overlapped in a photorefractive material the two light waves interfere and produce a sinusoidal optical interference pattern consisting of periodic light and dark fringes, figure 1.1 (a). The distance between the peaks of the illuminated regions is called the grating spacing Λ [4] and is given by the equation:

$$\Lambda = \frac{\lambda}{2n\sin\theta} \tag{1.1}$$

where λ is the wavelength, n is the refractive index, and θ is the half angle between the beams.

When the material is illuminated with a sinusoidal intensity pattern, photocarriers (electrons/holes) are excited form trapping sites (donors/acceptors) within regions of high irradiance to the conduction/valence band. The photocarriers diffuse (figure 1.1a) or drift in an applied field until they recombine with an ionized donor/acceptor site. The charges undergo subsequent excitation/trapping processes until they migrate out of the brightly illuminated regions to the dark regions. The separation of the charges from their original trapping sites (figure 1.1b) gives rise to a space charge field (figure 1.1c). Equilibrium is reached when the tendency of the charges to diffuse from areas of high charge density in the regions of high illumination is balanced by the drift of the carriers in the induced space charge field. The induced field modulates the refractive index of the material via the linear electro-optic effect (figure 1.1d). Typical field strengths of a few 100 V/cm are generated [4]. The subsequent diffraction grating can be used to measure the strength of the photorefractive effect. This technique is used throughout this thesis to characterise materials of interest.

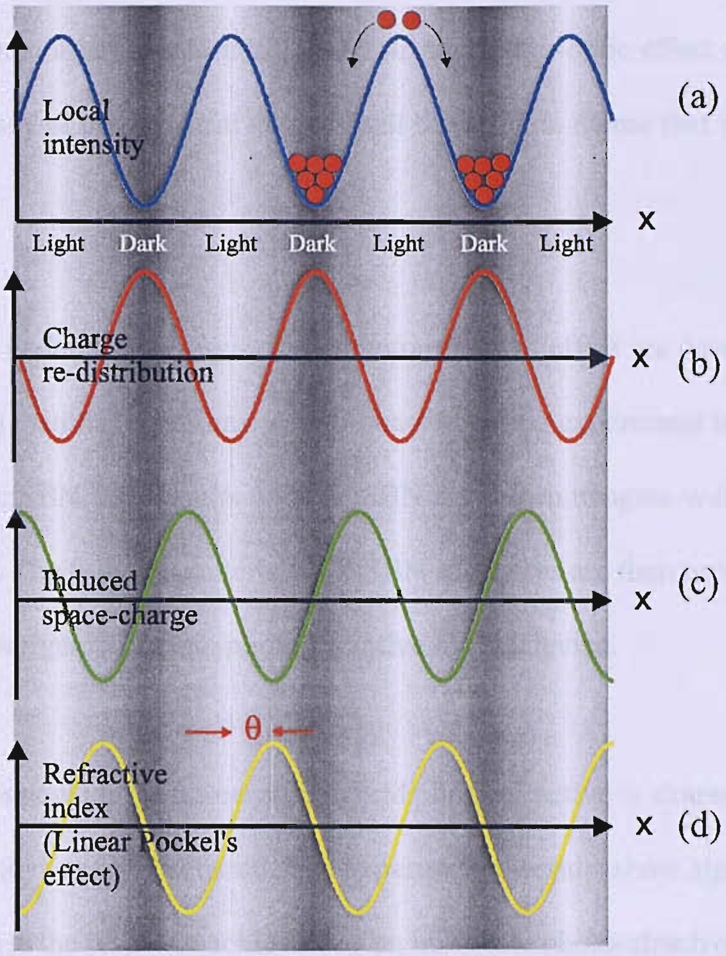

Figure 1.1 The photorefractive response to a sinusoidal intensity pattern.

A more thorough description of the photorefractive effect is introduced in chapter 2.

1.3 Thesis overview

In this chapter I introduce the photorefractive effect and describe some of the extraordinary optical effects that have been observed since photorefraction was first discovered in 1966. Many applications and materials have been studied and I give a brief review. Finally I introduce the idea of a hybrid device that exploits the phase-shift available in inorganic materials and the strong electro-optic effect of liquid crystals. The study of these hybrid devices will be the main theme that flows through my thesis.

In chapter 2 the underlying physics of the photorefractive effect are described using a set of governing material equations. A two-beam coupling experiment is designed and used to study Ce:SBN. The results with Ce:SBN are shown to agree well with the standard theory. The fully characterised Ce:SBN substrates are then used in chapter 3 to fabricate an inorganic-organic photorefractive hybrid device.

In chapter 3, this new inorganic-organic hybrid photorefractive is characterised and the underlying physics are discussed. The experimental results show significant enhancement over the response achieved by an inorganic photorefractive layer alone. However some of the off-axis results were unexpected. In particular, there is an absence of optical gain when the hybrid device was used under experimental conditions where gain was predicted by standard photorefractive theory.

To understand this unexpected result, the assumptions about the dominant driving mechanism in inorganic-organic photorefractives hybrid devices are challenged in chapter 4. Other possible mechanisms are investigated in order to gain greater understanding that will enable optimisation of the hybrid device. Through a combination of optical and atomic force microscope experiments the possible presence of another mechanism has been isolated to the Ce:SBN window rather than the liquid crystal layer. This is an important step towards the full understanding of the physics within the inorganic photorefractive hybrid and identifies a need for better theoretical treatments which are not available currently.

In order to improve the speed of the inorganic-organic hybrid device developed in chapter 3, a new hybrid photorefractive cell comprising a nematic liquid crystal layer in combination with an iron doped $KNbO_3$ window is described in chapter 5. The Potassium niobate hybrid is shown to exhibit faster response times than the Ce:SBN hybrid. This is an important result for my particular application.

Most of my studies have concentrated on the development of photorefractive hybrids for two-beam coupling but a potentially more compact solution is to use a counter propagating technique. In chapter 6, the reflection geometry photorefractive effect is introduced. The change in optical density and response times are measured for three crystals; a commercially grown piece of $Fe:LiNbO_3$, an in-house grown $Fe:KNbO_3$ crystal, and a commercially grown $Fe:KNbO_3$ crystal. $Fe:LiNbO_3$ and $Fe:KNbO_3$ are then used in tandem configuration to improve the response over that available with a single crystal.

In chapter 7, the work presented in this thesis is concluded with a summary and suggestions for further research. The publications arising from the work presented in this thesis are listed.

1.4 Optical effects that arise through photorefraction

1.4.1 Optical damage

Photorefractivity was discovered in 1966 as an optical damage mechanism in inorganic ferroelectric electro-optic crystals [1] that destroyed the spatial profile of a laser beam as it passed through a lithium niobate crystal. It was deduced that at high optical densities, two-photon absorption due to impurities within the crystal produced excited states that generated electrons. The electrons then migrated out of the illuminated regions and were trapped in the dark regions surrounding the beam. The inhomogeneity in the charge distribution produced a space charge field that induced a change in the refractive index across the beam penetrating the material and therefore destroyed the optical quality of the beams [4]. At high powers the photorefractive effect can lead to self-focussing and result in optical damage.

1.4.2 Two beam coupling in transmission geometry

A crucial property of photorefractives, which is exploited in the work presented in this thesis, is that the photorefractive grating can be phase shifted with respect to the initial optical interference pattern (see figure 1.1), resulting in asymmetric diffraction whereby one of the beams diffracts light into the other beam. One beam is amplified at the expense of the other which is attenuated. This process is known as two-beam coupling [3] and I use it extensively throughout my thesis to characterise materials.

This effect is best described by considering the effect that the induced grating has upon the interfering beams, figure 1.2, in what is referred to as transmission geometry, where the transmitted wave and the diffracted wave exit from the same side of the material.

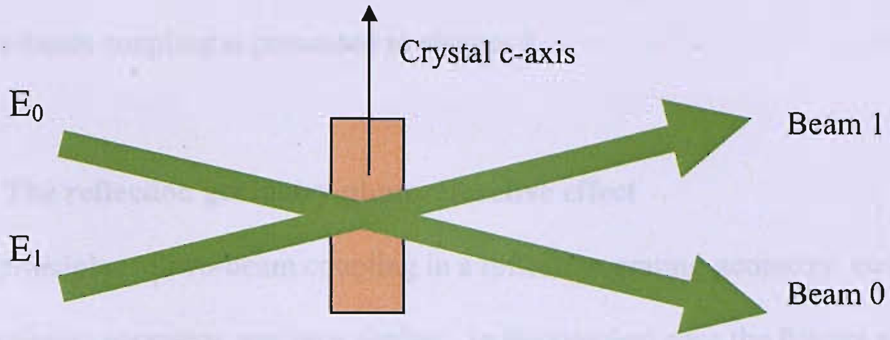

Figure 1.2. A schematic diagram of the two beam coupling geometry inside the crystal material.

The volume hologram written between beams 0 and 1 results in the diffraction of beam 0 into the path of beam 1, and vice-versa. In general the refractive index grating will be spatially phase shifted with respect to the intensity interference pattern by φ with respect to the fringe spacing Λ. In the arrangement shown in figure 1.2, the diffracted portion of beam 0 is advanced in phase by φ ahead of beam 1. The diffracted portion of beam 1 is retarded in phase by φ such that it lags behind beam 0. Each diffracted beam experiences an additional $\pi/2$ phase shift on Bragg diffraction as a result of energy conservation between the coupled waves. In materials in which the transport mechanism is dominated by diffusion $\varphi = \pi/2$. In this case beam 1 and the diffracted component of beam 0 constructively interfere, while beam 0 and the diffracted component of beam 1 destructively interfere. By this mechanism energy is transferred between the two beams as they propagate through the material. Energy is transferred in a direction defined by the orientation of the crystallographic axes and dominant photocarrier. The energy transfer process results in a variation of the modulation ratio of the intensity interference pattern, and therefore the refractive index profile, throughout the interaction region. A detailed mathematical description of two-beam coupling is presented in chapter 2.

1.4.3 The reflection geometry photorefractive effect

The principles of two-beam coupling in a reflection grating geometry, compared to transmission geometry, are very similar. In the simplest case the fringes are parallel to the b-axis, see figure 1.3. A wave incident along the c-axis will give rise to a Fresnel reflected wave from the back face i.e. a wave travelling in the negative c direction. The two waves then interfere and a grating is written. There is very little difference in principle between transmission and reflection gratings but there is a great difference in the actual magnitude of the grating spacing. As shown in figure 1.3, the resulting grating vector is now twice as large as the individual wave vectors, yielding $\Lambda = \lambda / 2$ [3].

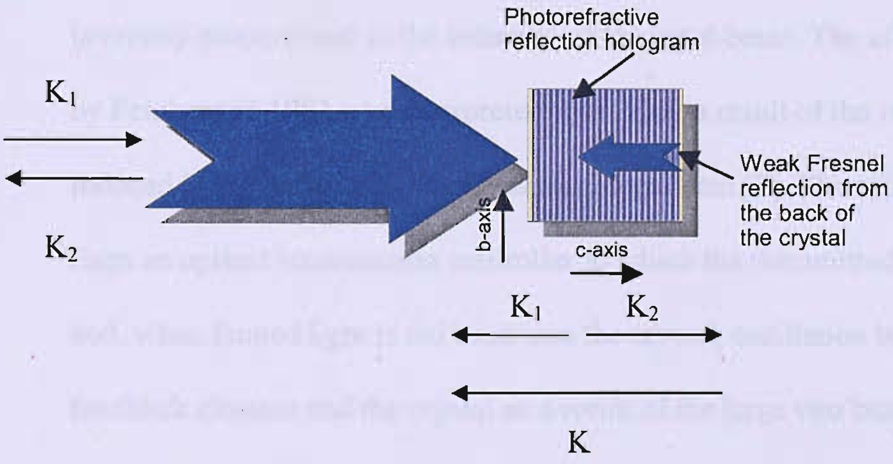

Figure 1.3. Diffraction from a reflection grating.

For a free-space wavelength of 0.5μm and a refractive index of 2.5 the grating spacing is as small as 100nm. Since the wavelength selectivity is inversely proportional to the number of periods transversed [3]. A material of 5mm thickness then contains 50 000 grating periods. This piece of material may then serve as a frequency filter. At the above wavelength of 0.5μm the wavelength sensitivity is 0.1Å. Such wavelength selectivity is ideal for use in practical filters.

1.4.4 Beam fanning

Beam fanning is an interesting effect that has been reported in very high gain photorefractive materials, such as SBN and BTO [4]. Beam fanning is a form of self-induced two-beam coupling. It is a dramatic effect that occurs when scattered light within a photorefractive crystal interferes with the main beam to form a photorefractive grating. The scattered light is amplified to such an extent that significant depletion of an input pump beam can occur and the scattered light forms an intense beam in the optimum gain direction [5]. The scattered beam emerges in a wide "fan" of light [6] giving the process its name. Up to 99% of the input beam power maybe deflected into the fan. The decay of the transmission is approximately inversely proportional to the intensity of the input beam. The effect was first observed by Feinberg in 1982 who interpreted it as being a result of the refractive index profile induced in the material by the Gaussian input beam [7]. The effect has been used to form an optical transmission controller in which the transmitted energy is limited [8] and, when fanned light is fed back into the crystal, oscillation builds up between the feedback element and the crystal as a result of the large two beam coupling gain available. This effect allows the construction of self starting oscillators and phase conjugate mirrors.

1.5 Applications of photorefractives

The large effective non-linearity available at low optical densities in photorefractive materials has attracted many uses. Soon after the discovery of photorefractive effect in 1966 it was reported by Chen in 1968 [2] that these new "laser damage" materials could be used for high density optical storage of data. The ferroelectric materials were referred to as "laser damage" materials because when subjected to intense focused radiation from pulsed lasers was found to induce local semi-permanent refractive index changes which ruined phase matching for second harmonic generation that was the subject of research. It then was proposed that the information contained in a patterned laser beam be stored in a photorefractive material using a hologram and Chen published the first charge migration model in 1969 specific to ferroelectric crystals. The model used the spontaneous polarisation, characteristic of such materials, combined with the illumination pattern, due to the interference of two beams within the medium, to explain the creation of high quality volume holograms in ferroelectrics [9]. Excitation of electron carriers and their migration by diffusion due to the mediums internal electric field would then induce a space charge field. A proportional refractive index grating is then produced by the electro-optic effect with the space period as the optical interference pattern. It was then discovered that flooding the crystal with a large region of uniform illumination re-excites the charge carriers so that their distribution becomes uniform again so that the refractive index profile is erased [10]. This first discovery meant that a hologram with read-write-erase capability can therefore be produced via the photorefractive effect. The importance of drift in charge transport on hologram storage was underlined by Thaxter who reported [11] the effects of externally applied field in SBN leading to the drift model for carrier migration. The charge transport was subsequently extended to include the effects of diffusion of charges by Ammodei [12], and the photovoltaic effect in Glass. The benefits of crystalline photorefractive materials include longer storage times than non-crystalline photorefractives and are considered for applications for long term data storage [13]. However more recently liquid crystals and polymers have been considered for dynamic holography [14].

The demonstration in 1979 of optical phase conjugation on the milliwatt pump power scale in BSO [15] earmarked photorefractives for low power continuous wave non-linear optical processes. The discovered generation of conjugate waves has attracted a lot of attention in the literature due to the fascination of the idea of time reversal and demonstrations in which severely distorted optical beams can be restored to their original unabberated state.

Photorefractives can also be used for image sensing through highly scattering media, as scattered photons with longer path lengths pass undetected through the material [4], as only photons that lie within the coherence length of the laser will contribute to the interference pattern. The ballistic photons that pass straight through the material arrive first and are used to form the image.

In summary, photorefractives have been proposed for many applications, those above and others such as coherent image amplification [16], edge enhancement and Fourier transform manipulation [17], and optical filtering [3].

However the work presented in this thesis is focussed towards an application that is classified and cannot be described in detail here, but further details can be found in reference [18]. For this application the photorefractive material must operate at high speed in a two-beam coupling geometry where energy transfer between the beams must be very efficient. In addition my devices must operate over a wide wavelength range, should not require any external field, and should be compatible with a tight focussing geometry [18].

Two beam coupling has a number of applications. A weak beam may be amplified up to 10^3 [19]. High gain allows the amplification of optical images [20] and the steering of laser beams [21]. The gain is reduced when incoherent light is incident allowing incoherent to coherent image conversion [22]. Transient two-beam coupling has been used to make optical tracking filters that only transmit the moving parts of an image [23]. Some of the most interesting effects of two wave mixing have been demonstrated in optical resonators and other schemes employing optical feedback [15]. The resonator systems rely on feeding of a light beam amplified by two wave mixing back to the input of the mixing region creating a positive feedback loop. Resonators using materials SBN and BTO have been demonstrated that operate at optical power densities as low as $\mu W/cm^2$ [15].

1.6 Inorganic photorefractive materials

In the next two sections I will describe some of the types of different materials that have been used as photorefractive materials including the materials used in this thesis. Table 1.1 below lists some of the common inorganic photorefractive materials and some of their material parameters.

Photorefractive material and symmetry	**Dielectric constant**	**Refractive index**	**Electro-optic coefficient (pm/V)**	**Functional wavelength range (µm)**	**$n^3 r_{ij}$**
SBN	$\varepsilon_1=450$	$n_1=2.37$	$r_{12}=47$	0.4-0.7	1018
4 mm	$\varepsilon_2=450$	$n_2=2.33$	$r_{23}=47$		
	$\varepsilon_3=820$		$r_{33}=420$		
			$r_{42}=42$		
			$r_{51}=42$		
$KNbO_3$	$\varepsilon_1=1000$	$n_1=2.28$	$r_{12}=28$	0.4-0.7	690
2 mm	$\varepsilon_2= 1000$	$n_2=2.329$	$r_{23}=1.3$		
	$\varepsilon_3=55$	$n_3=2.169$	$r_{33}=64$		
			$r_{42}=380$		
			$r_{51}=105$		
$BaTiO_3$	$\varepsilon_1=3600$	$n_1=2.404$	$r_{12}=8$	0.4-0.9	11300
4 mm	$\varepsilon_2= 3600$	$n_2=2.316$	$r_{23}=8$		
	$\varepsilon_3=135$		$r_{33}=28$		
			$r_{42}=1640$		
			$r_{51}=1640$		
BSO	$\varepsilon=56$	2.54	$r_{41}=5$	0.4-0.7	82
23					
BGO	$\varepsilon=47$	2.54	$r_{41}=3.22$	0.4-0.7	-
23					
GaAs	$\varepsilon=13.2$	3.6	$r_{41}=1.1$	0.8-1.8	43
$\bar{4}3m$					

$LiNbO_3$ 3 m	ε_1=43 ε_2= 43 ε_3=28	n_1=2.286 n_2=2.200	r_{13}=9.6 r_{22}=6.8 r_{33}=30.9 r_{51}=32.6	0.4-0.7	-
InP 32	ε=12.6	1.45	r_{41}=1.45	0.85-1.3	52

Table 1.1. Common photorefractive materials and their material parameters.

The quantity n^3r_{ij} is known as the dynamic range and governs the maximum possible change in refractive index, r_{ij} is the electro-optic susceptibility tensor and is discussed further in chapter 2. Table 1.1 shows that the dynamic range is greatest in $BaTiO_3$ followed by SBN. For strong two beam coupling, a large change in refractive index is important so $BaTiO_3$ is the obvious choice. However, $BaTiO_3$ is too slow to be of use for my application. My application requires a simple device that exhibits reasonable response times and therefore my work has focussed on the use of SBN as a simpler and faster system. SBN does not require the application of an external field and the charge migration mechanism, which will be discussed in detail in chapter 2, results in optimum energy transfer conditions. Optimum energy transfer conditions occur because the phase shift between the optical interference pattern and the refractive index grating is $\pi/2$.

Pure inorganic crystals do not usually possess a high sensitivity to light but doping them with transition metals can make them much more photosensitive. Transitional metals are used due to their ability to give electrons to the conduction band under the action of light. Different dopants can increase the functional wavelength of a photorefractive material. The most commonly available dopant for SBN is cerium and iron for $LiNbO_3$ and $KNbO_3$. These dopants have been used in the crystals described in this thesis. Cerium occupies the strontium sites in SBN (Ce^{3+} and Ce^{4+} are the oxidation states); whereas iron occupies the niobium sites in $KNbO_3$ (Fe^{2+} and Fe^{3+} are the oxidation states). As mentioned, the photorefractive effect relies upon the redistribution of charges in impurities. It is therefore highly desirable to control the type of traps and their concentrations. This is conveniently done by doping. When a material is doped with acceptors or donors they may reside anywhere in the forbidden energy band. An important factor is the energy or position of these trap levels within the forbidden band as this determines the spectral response of the photorefractive effect (figure 1.4). The photon energy therefore has to be larger than the energy difference between the trap level and the relevant band in order for the photon to be absorbed. Another important consideration is whether the traps are deep-level traps situated near the middle of the band gap or whether they are shallow traps located close to the conduction or valance bands. In the case of shallow traps, thermal excitation and optical intensity can play a major role in determining whether a particular level is active, any trap which is very close to a band will be completely ionised by thermal excitations.

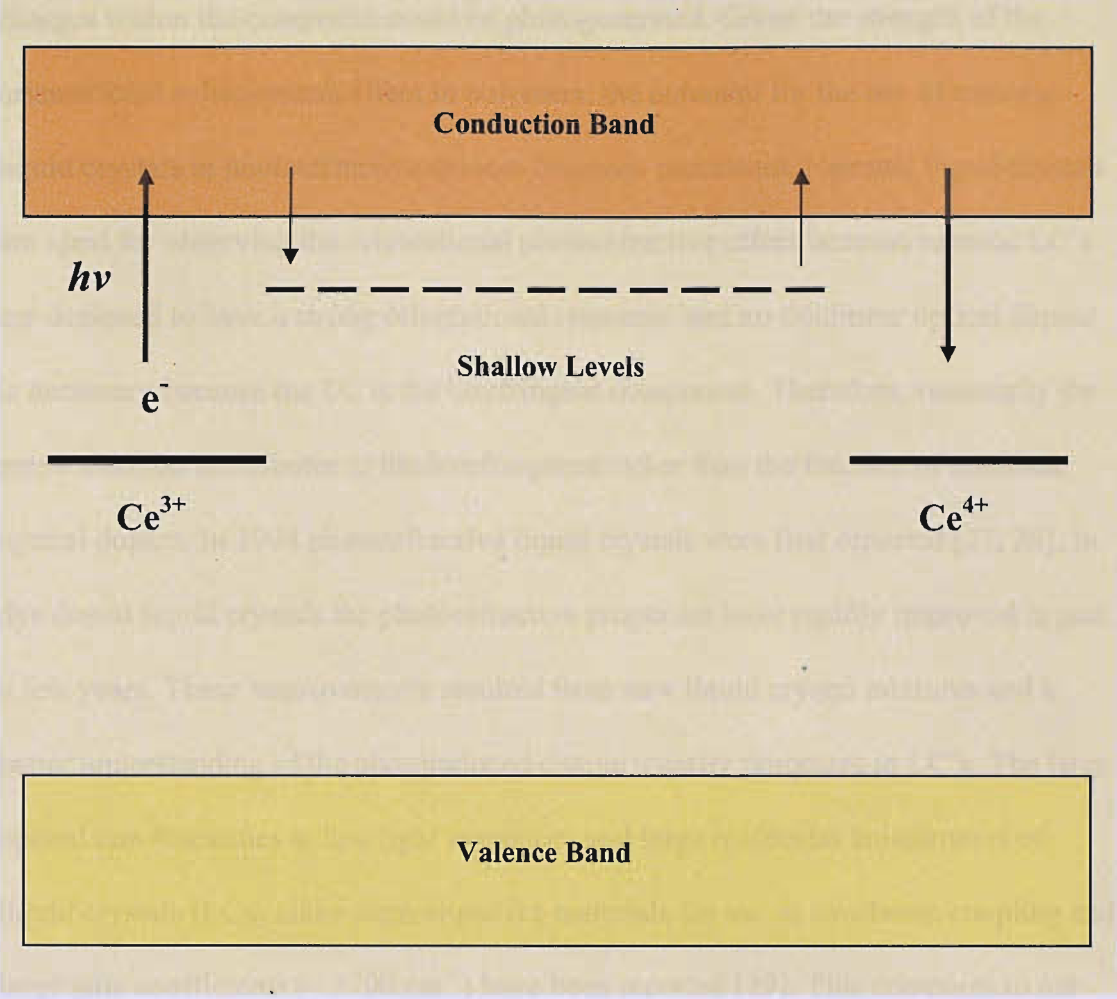

Figure 1.4. Band diagram of the charge-transport situation in cerium-doped strontium-barium niobate. Charge carriers are excited by light from Ce^{3+} into the conduction band. They are several times trapped and thermally re-excited at shallow levels. Finally, they recombine with the deep-level Ce^{4+}.

1.7 Organic photorefractives

In 1991 the photorefractive effect was reported in polymers [24]. Photorefractive polymers are generally composite materials possessing additives that induce the photorefractive effect [25, 26]. They initially consisted of photoconductive polymers doped with a high concentration (>30%) of a non-linear chromophore, and an electron acceptor that formed a charge transfer complex with the polymer so that mobile charges within the composite could be photogenerated. Given the strength of the orientational enhancement effect in polymers, the potential for the use of nematic liquid crystals in photorefractive devices becomes prominent. Nematic liquid crystals are ideal for observing the orientational photorefractive effect because nematic LC's are designed to have a strong orientational response, and no nonlinear optical dopant is necessary because the LC is the birefringent component. Therefore, essentially the entire medium contributes to the birefringence rather than the fraction of nonlinear optical dopant. In 1994 photorefractive liquid crystals were first reported [27, 28]. In dye doped liquid crystals the photorefractive properties have rapidly improved in just a few years. These improvements resulted from new liquid crystal mixtures and a better understanding of the photoinduced charge transfer processes in LC's. The large optical non-linearities at low light intensities and large molecular anisotropies of liquid crystals (LCs) make them attractive materials for use in two-beam coupling and large gain coefficients (~ 3700 cm^{-1}) have been reported [29]. This compares to net gain coefficients for polymers that range upwards of $200cm^{-1}$ and inorganic ferroelectric materials and semiconductors with gain coefficients of $10cm^{-1}$ to $40cm^{-1}$[4].

Conventional LC devices commonly comprise a thin LC layer between indium tin oxide (ITO) electrodes, figure 1.5. Surfactant or rubbed polymer coatings on the inner electrode surfaces cause the molecular directors to align (homeotropically or co-planar) to a common direction reducing light scattering and allowing modulation of the local refractive index by the photorefractive space-charge fields [30, 31]. Photoexcitation in a fullerene such as C_{60} followed by charge migration and trapping allows a space-charge field be to developed in the LC [30, 31]. In order to generate the mobile ions that can produce a space-charge field in liquid crystals, the LCs are doped with easily oxidised molecules, such as the laser dye R6G [30], that undergo photoinduced charge separation. For ion generation, photoexcitation of the donor molecule is followed by collisional interactions with the neutral electron acceptor molecules. This is followed by charge separation and generation of an ion pair. The critical final step is for a fraction of the ion pairs to form solvent separated ions. Only the solvent separated ions can diffuse through the LC to create an inhomogeneous spatial charge distribution over macroscopic length scales.

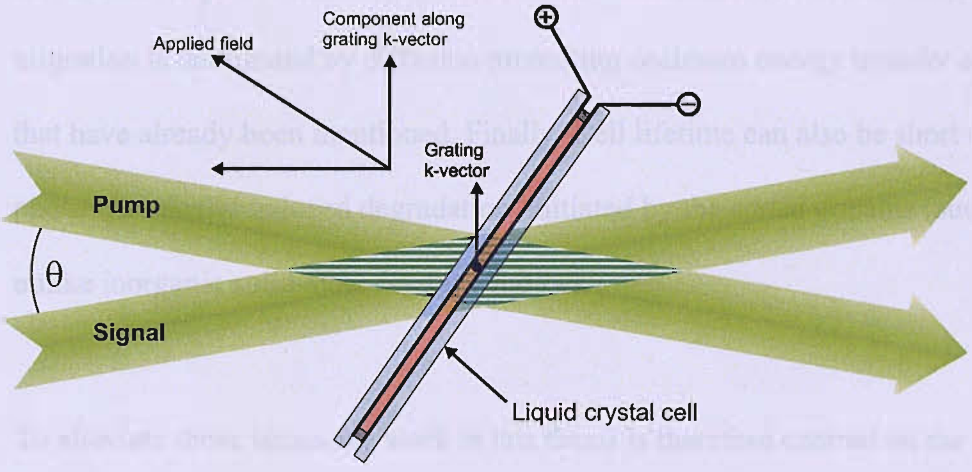

Figure 1.5. Schematic of a conventional photorefractive hybrid cell.

However, although the gain exhibited in these conventional hybrids (figure 1.5) is so large compared to inorganic materials, it presents too much of a compromise on device operation for my application. Photorefractive gratings in LC's operate in the Raman-Nath regime, producing multiple diffraction orders, unlike the Bragg regime that can be easily obtained using inorganic crystals. This is due to larger fringe spacings in LC's as a result of space-charge field formation through ion diffusion. Ion diffusion does not lend itself to small fringe spacings because of ion recombination issues [4], as the collective director orientational response necessitates larger fringe spacing. Also, to induce directional charge transport along the wave vector axis a small electric field (~0.01V/μm) has to be applied across the LC layer compared to some inorganic crystals such as SBN and $KNbO_3$ that are entirely passive (as well as promote Bragg diffraction conditions). The applied field is also needed due to the collective orientational response that produces the refractive index change. Since charge migration is dominated by drift, small (<< 90^o) phase shifts between the writing interference pattern and the resulting refractive index grating, which restricts the amount of power transferred between the beams. In SBN and $KNbO_3$ charge migration is dominated by diffusion promoting optimum energy transfer conditions that have already been mentioned. Finally, Cell lifetime can also be short due to photo-chemically induced degradation, initiated by the added dopants (such as C60) unlike inorganic solid-state crystal windows.

To alleviate these issues the work in this thesis is therefore centred on the development and characterisation of novel inorganic-organic photorefractive hybrid devices in which the nonlinear gain available from a liquid crystal layer is induced by the space-charge generation properties of an inorganic window. The concept of using an inorganic window to influence a LC layer is completely new. It will be shown that this hybrid approach alleviates many of the above problems associated with normal photorefractive liquid crystal cells and dramatically enhances the response compared with inorganic materials alone.

1.8 The Inorganic-organic photorefractive hybrid cell design

The hybrid cell is shown in figure 1.6. The cell windows are inorganic photorefractive crystals coated on the interior surfaces with an appropriate alignment layer to induce the desired alignment of the liquid crystal (LC). The windows are held together by clips. Copper foil spacers allow transverse electric fields to be applied and dictate the thickness of the liquid crystal layer that was chosen to be 12.5μm. Room temperature nematic liquid crystals were used in all of the cells investigated here so that no external temperature control was needed.

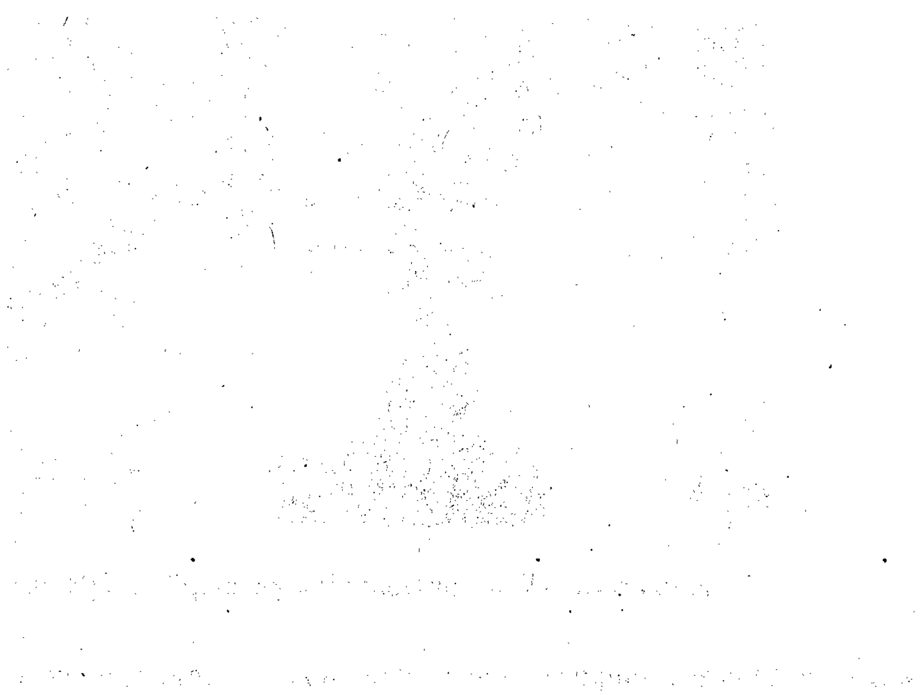

[illegible]

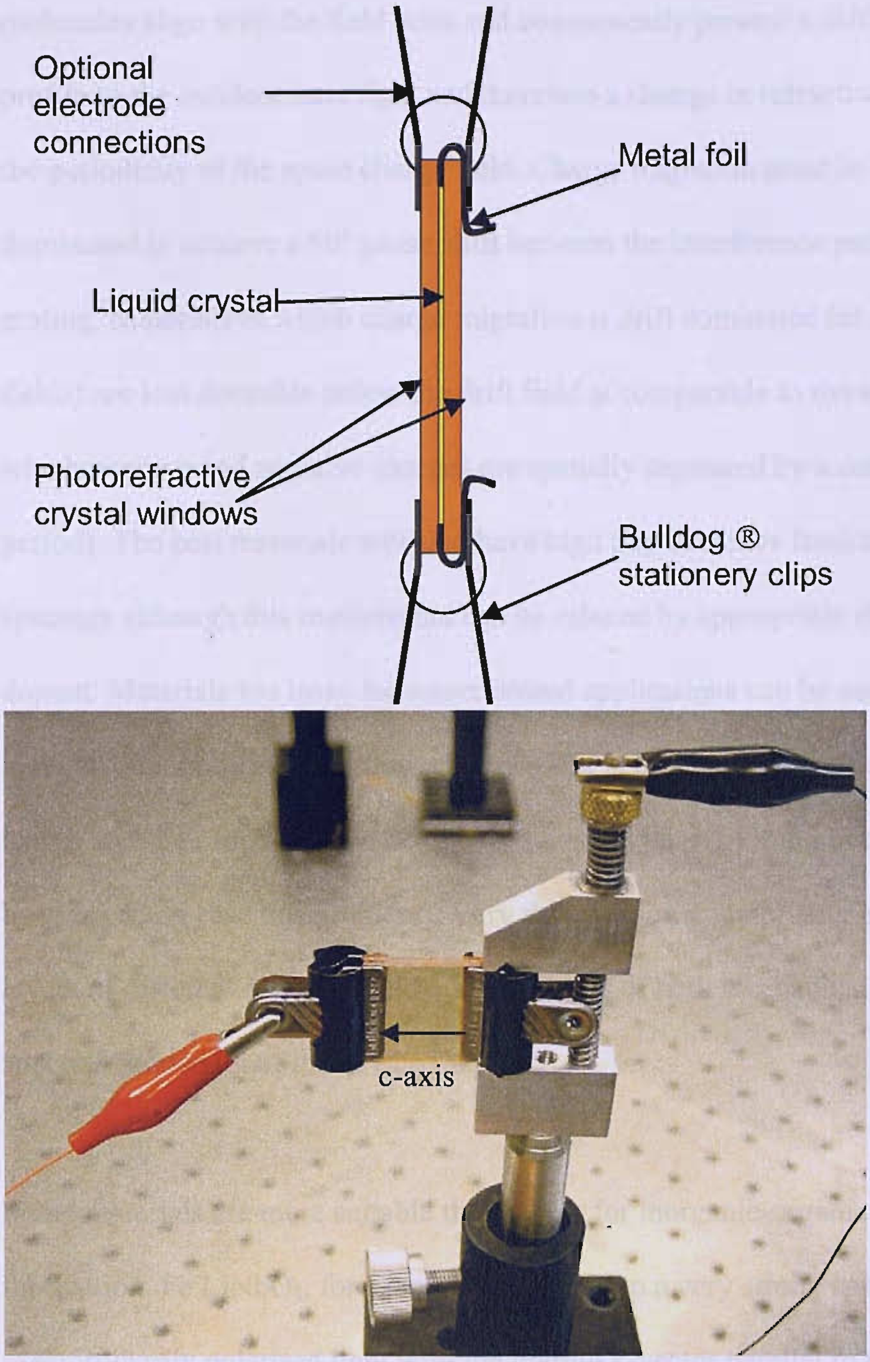

Figure 1.6. Hybrid liquid crystal / inorganic cell construction.

The basic window property required to exploit the liquid crystal layer for beam coupling is the ability to support a space-charge field through photoexcitation, charge migration and trapping. It should not be necessary that the space-charge field induces a local electro-optic response since modulation of the refractive index occurs in the LC. When the space charge field penetrates the liquid crystal layer, the dipolar molecules align with the field lines and consequently present a different dielectric profile to the incident laser light and therefore a change in refractive index that shares the periodicity of the space charge field. Charge migration must be diffusion dominated to achieve a 90° phase shift between the interference pattern and the grating. Materials in which charge migration is drift dominated (as a result of applied fields) are less desirable unless the drift field is comparable to the saturation field (in which positive and negative charges are spatially separated by a complete grating period). The best materials will also have high trap densities facilitating fine grating spacings although this requirement can be relaxed by appropriate choice of the dopant. Materials too lossy for conventional applications can be used since absorption loss can be minimized with thin windows and is limited only by the Debye screening length and their mechanical strength (although support of thin photorefractive wafers by glass could ease this problem). Very thin windows comprising epitaxially stacked layers of different crystals could address issues of both mechanical strength and spectral bandwidth of the device [32].

Some materials are more suitable than others for inorganic-organic hybrid cell fabrication. Fe:$LiNbO_3$, for example, can develop a very strong space-charge field for extraordinarily polarised light with the grating k-vector parallel to the crystal c-axis, aided by the photovoltaic effect. However, extraordinary polarised light causes beam fanning through the accumulation of bulk photovoltaic charges on either side of the pump and signal beams severely degrading device gain and resolution. Ordinary polarised light greatly reduces photovoltaic beam fanning but it also reduces the magnitude of the space-charge field. Other problems associated with Fe:$LiNbO_3$ are a relatively low sensitivity and very long grating lifetimes requiring intense optical exposure and/or thermal cycling for erasure. Optically active materials, such as the silenites (e.g. BTO and BGO), rotate the incident beam's polarisation necessitating very thin windows and careful adjustment of the input polarisation state according to laser wavelength and window thickness to prevent loss of beam coupling efficiency arising from accidental misalignment of the polarization and grating k-vector at the liquid crystal boundary [32]. For these reasons I have chosen to use SBN and later $KNbO_3$, which are not optically active, have short grating lifetimes, and are dominated by diffusion.

The advantages of using an inorganic window compared to a doped polymer layer or a semiconductor are:

- High trap densities can be exploited so that fine grating spacings can be realised.
- An optimum phase shift of 90^0 between the optical interference pattern and the diffraction grating can be reached for optimum power transfer between beams.
- Bragg-matched diffraction conditions.
- Gain contribution from both the crystal window and the liquid crystal layer.

The disadvantages are that inorganic windows are considerably more expensive to grow; they require cutting and polishing, and the crystal axes needs to be orientated, usually by x-ray diffraction. Good quality uniform inorganic windows are less readily available. Whereas, doped polymers are relatively simple to synthesise and can be spin coated on cheap glass substrates.

1.9 References

[1] A. Ashkin, GD Boyd, JM Dziedzic, RG Smith, AA Ballman, JJ Lexinstein, K Nassau, *Optically-induced change in refractive indices in $LiNbO_3$ and $LiTaO_3$*, Applied Physics letters. **9**, 72 (1966).

[2] FS Chen, JT La Macchia, DB Fraser, *Holographic storage in lithium niobate*, Applied Physics Letters. **13**, 223 (1968).

[3] P Gunter, JP Huignard, *Photorefractive Materials and their applications 1: Fundamental Phenomena*, Berlin: Springer-Verlag (1988).

[4] V Ramamurthy, KS Schanze, *Optical Sensors and Switches*, New York: Marcel Dekker (2001).

[5] VV Voronov, IR Dorosh, Yu.S. Kuzminov, NV Tkachenko, *photoinduced light scattering in cerium-doped barium strontium niobate crystals,* Soviet J. Quantum Electronics. **10**, 1346 (1981).

[6] J. Feinberg, *Asymmetric self-focusing of an optical beam from the photorefractive effect*, J.Opt.Soc.America. **72**, 46 (1982).

[7] J. Fienberg, *Asymmetric self-defocussing of an optical beam from the photorefractive effect*, J.Opt.Soc.Am. 72,46 (1982)

[8] M. Cronin-Golomb and A. Yariv, *Optical limiters using photorefractive nonlinearities*, J.Appl.Phys. 57, 11 (1985).

[9] F.S. Chen, *Optically induced change of the refractive indices. in LiNbO3 and LiTaO3*, J.Appl.Phys.40,3389-3396 (1969).

[10] T.J. Hall, R.Jaura, L.M. Connors, and P.D. Foote, *The photorefractive effect –a review*, Prog. Quantum. Elecronics. 10, 77-146 (1985).

[11] JB Thaxter, *Electrical control of holographic storage in strontium-barium niobate*, Applied Physics Letters. **15**, 210 (1969).

[12] JJ Amodei, *Electron diffusion effects during hologram recording in crystals*, Applied physics letters. **18**, 22 (1971).

[13] D Psaltis, F Mok, *Holographic memories*, Scientific American. **70**, (1995).

[14] B Kippenlen, SR Marder, E Hendrickx, JL Maldonado, G Guillemet, BL Volodin, DD Steel, Y Enami, Sandalphon, YJ Yao, JF Wang, H Rockel, L Erskine, N Peyghambarian, *Infrared Photorefractive polymers and their applications for imaging*, Science. **269**, 54 (1998).

[15] JP Huignard, JP Herriau, P Auborg, E Splitz, *Phase conjugate wavefront generation via real time holography in BSO crystals*, Optics letters. **4**, 21 (1979).

[16] Y Fainman, E Klanchik, SH Lee, *Optimal coherent image amplification by two wave coupling in photorefractive BTO*, Optical engineering. **25**, 228 (1986).

[17] JA Khoury, G Hussain, RW Eason, *Contrast manipulation and controllable spatial filtering via photorefractive two beam coupling in BTO*, Optics Communication. **70**, 272 (1989).

[18] G Cook, M Deer, C Wyres, L Taylor, *Photorefractives for fast optics*, Journal of Defence Science. **9**, 2 (2004).

[19] P. Refregier, *Two beam coupling in photorefractive $Bi_{12}SiO_{20}$ crystals with moving grating: theory and experiments*, Journal of Applied Physics, **58(1)**, 45-57 (1985).

[20] T. Tschudi, A. Herden, J. Goltz, H. Klumb, and F. Laeri, *Image amplification by two- and four-wave mixing in BTO photorefractive crystals*. IEEE J. Quantum Electronics, 22(8):1493-1502 (1986).

[21] D. Rak, I. Ledoux, and J.P. Huignard. *Two-wave mixing and energy transfer in BTO application to laser beamsteering.* Optics Comm, 49(4):302-306 (1984).

[22] A. Marrakchi. *two-beam coupling photorefractive spatial light modulation with reversible contrast.* Applied Physics letters, 8:634-636 (1988).

[23] N. Sze-Kwong, Y. Tamita, A. Yariv. *Optical tracking filter using transient energy coupling.* J. Optical Soc. B, 5:1788-1791 (1988).

[24] S Ducharme, JC Scott, RJ Twieg, WE Moerner, *Observation of the Photorefractive Effect in a Polymer*, Phys. Rev. Lett. **66,** 1846 (1991).

[25] WE Moerner, A Grunnet-Jepsen, CL Thompson, *Photorefractive polymer*, Annu. Rev.Mater.Sci. **27**, 585 (1997).

[26] SCW Hyde, NP Barry, R Jones, JC Dainty, PMW French, MB Klein, BA Wechsler, *Depth-resolved holographic imaging through scattering media by photorefraction*, Opt. Lett. **20**, 1331 (1995).

[27] IC Khoo, H Li, Y Liang, *Observation of orientational photorefractive effects in nematic liquid crystals*, Opt.Lett. **19,** 1723 (1994).

[28] EV Rudenko, AV Sukhov, *Photoinduced electrical conductivity and photorefraction in a nematic liquid crystal*, JETP Lett. **59**, 142 (1994).

[29] Bartkiewicz S, Matczyszyn K, Miniewicz A and Kajzar F, *High gain of light in photoconducting polymer-nematic liquid crystal hybrid structures*, Optics Communications. **187,** 257-261 (2001).

[30] I. C. Khoo, *Liquid Crystals,* John Wiley & Sons Inc, (1995).

[31] F. Simoni, *Nonlinear Optical Properties of Liquid Crystals and Polymer Dispersed Liquid Crystals,* Series on Liquid Crystals Volume 2, World Scientific Publishing Co. Ltd, (1997).

[32] G. Cook, C Wyres, M Deer, D Jones, *Hybrid organic-inorganic photorefractives*, SPIE, **5213** (2003).

Chapter 2 The Photorefractive effect and two beam coupling in Ce:SBN

In this chapter, the material response to intensity fringes in photorefractive crystals is considered. The physical phenomena taking place inside a photorefractive is introduced and then a set of material equations, that describe the photoinduced changes, are developed for a material where the charge being transferred is electrons rather than holes. The problems of solving these equations for grating formation are considered and solutions are obtained after reducing to one-dimension and assuming low intensity modulation. The resulting solutions of these material equations are then applied to cerium doped (0.01 molar %) strontium barium niobate (Ce:SBN) to predict the small signal gain characteristic as a function of grating spacing. The small signal gain is then measured for two Ce:SBN crystals and is shown to agree well with theory. The windows that are characterised in this chapter are used to fabricate an inorganic-organic photorefractive hybrid that is described in the next chapter.

The properties of SBN, a member of the tungsten bronze family, can be tailored by changing the growth parameters in the mix. The ferroelectric transition can be adjusted from 200^0C to 60^0C [1]; the crystal structure is tetragonal in both these phases and this allows the easy growth and poling of high quality crystals. Poling ensures that the domains are aligned. SBN is very hard and can be cut and polished to a very high optical quality. Also, the index change is large enough for photorefractive applications.

Chapter 1 considered how optical beams interact in photorefractive materials, such as Ce:SBN, to produce an intensity pattern that induces material changes to write a photorefractive grating. It would therefore appear that the optical beams must depend on time as well as position. Fortunately time and position dependencies can be separated in the following formulation because the time dependent material effects are slowly varying in time compared to the optical effects and the coupling along the propagation direction is slowly varying in space compared to the intensity fringes perpendicular to the propagation direction [1].

2.1 The Physics

A photorefractive material usually contains one type of mobile carriers, electrons, and two types of impurities, donors and acceptors. These impurities reside deep in the forbidden gap between the valence band and the conduction band. Some of the donor atoms and all of the acceptor atoms are assumed to be ionised. The ionised acceptors N_A^- are inactive.

2.1.1 Photoexcitation

When light, a stream of photons, passes through a doped photorefractive crystal absorption leads to the ionisation of donor sites. The ionisation energy of each donor is of the order of a few electron volts [1].Without this absorption; the light would pass through the crystal without photorefractive interactions occurring.

The photon energy $h\omega/2\pi$, where h is Plank's constant and ω is the wave angular frequency, must be more than sufficient for ionisation because each ionisation event is associated with the removal of one photon from the beam. Photo-ionisation therefore results in attenuation of the beams. Photons may also be taken from the beam by unwanted effects such as phonon creation. However the following analysis assumes that each absorbed photon results in an ionised donor plus an unbound electron. The photoionisation rate R_{ph} is given by [1,11]

$$R_{ph} = sI(N_D - N_D^+) \tag{2.1}$$

where s (cm^2) is the photoionisation cross-section of the unionised donors, I (J/scm^2) is the intensity, N_D is the donor density and N_D^+ is the ionised donor density [4].

2.1.2 Charge transfer mechanisms

While the ionised donors remain fixed in the crystal lattice, the photoinduced unbound electrons are free to propagate through the crystal in the conduction band. The driving mechanism may be diffusion down a concentration gradient of carriers, or drift in a static field (due to the resultant space charge field, or an externally applied field). The transfer of electrons results in a conduction current density $\boldsymbol{J}$ given by [11]

$$\boldsymbol{J} = e\mu n\boldsymbol{E} + \mu k_b T\nabla n = \mu k_b T\nabla n \tag{2.2}$$

Where the first term is due to drift and the second term due to diffusion; $\boldsymbol{E}$ is the externally applied field ($\boldsymbol{E}=0$ here because no applied fields are used in this thesis), μ is the effective drift mobility, e is magnitude of the electron charge, n is the free electron density, k_b is Boltzmann's constant and T is the absolute temperature.

2.1.3 Carrier recombination

Free electrons do not remain in the conduction band indefinitely; two-body electron ionised donor recombination can occur giving a neutral donor and a photon or a phonon. The recombination rate, R_r, depends on both the free electron density and the ionised donor density [11]:

$$R_r = \gamma_r n N_D^+ \tag{2.3}$$

where γ_r is a recombination coefficient.

In summary, electrons are optically excited out of un-ionised donor atoms into the conduction band where they diffuse before recombining elsewhere with ionised donors.

2.2 The material equations

The next stage in this theoretical approach is to formulate a set of self-consistent equations that will describe the material response so that the resulting optical effects can be related to the photorefractive material properties. A rate equation for ionised donors follows from the difference of photoexcitation and recombination rates [1,11]:

$$\frac{\partial N_D^+}{\partial t} = sI(N_D - N_D^+) - \gamma_r n N_D^+ \qquad (2.4)$$

Using the continuity equation $\nabla \cdot \underline{J} = -\partial\rho/\partial t$, that follows from Maxwell's equations $\nabla.\underline{D} = \rho$ and $\nabla \times \underline{H} = \underline{J} + \partial\underline{D}/\partial t$ (where $\underline{D}$ is the electric flux density, $\underline{H}$ is magnetic field intensity, and ρ is the charge density) and expressing ρ as $e(N_D{}^+ - n)$, we get:

$$\frac{\partial n}{\partial t} = \frac{\partial N_D^+}{\partial t} + \frac{1}{e}\nabla\underline{J} \qquad (2.5)$$

Finally to complete the set, using Poisson's equation (the static case of Maxwell's equation $\nabla.\underline{D} = \rho$):

$$\varepsilon_s \nabla.\underline{E_w} = \rho = e(N_D^+ - n) \qquad (2.6)$$

where ε_s is the static permittivity. The above equations were first proposed by Kukhtarev *et al.* in 1979 [2, 3].

2.3 Solutions of the material equations

Ideally, the material equations could be solved to give a relationship between the space charge field (the resulting electric field), $\underline{E_w} = \underline{E}(\underline{r},t)$, and the intensity $\underline{I}(\underline{r},t)$.

However, the material equations are a set of coupled partial non-linear differential equations with no general solution and can only be solved by making approximations. The solution depends on the driving intensity term, $I(\underline{r},t)$ so the first step is to define it in terms of the writing waves. Consider two beams incident on a crystal shown in figure 2.1. The electric fields of the beams can be represented as complex wave functions:

$$\underline{E_0} = A_0(\underline{r},t)\exp j(\omega_0 t - \underline{k_0}.\underline{r}) \tag{2.7}$$

$$\underline{E_1} = A_1(\underline{r},t)\exp j(\omega_1 t - \underline{k_1}.\underline{r}) \tag{2.8}$$

where A_0 and A_1 are field amplitude, ω_0 and ω_1 are the angular frequencies ($\omega_0 = \omega_1$ here), and $\underline{k_0}$ and $\underline{k_1}$ are the propagation vectors in the medium.

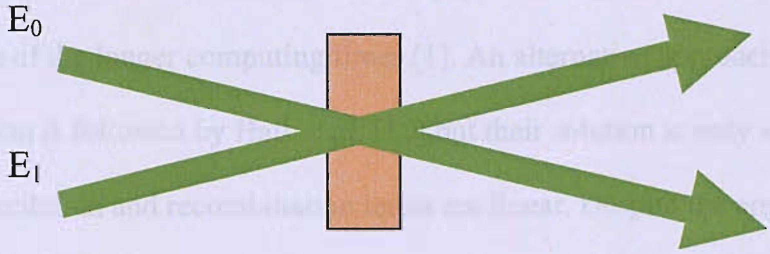

Figure 2.1. A schematic diagram of the two beam coupling geometry inside the crystal material.

With this complex representation the intensity is proportional to the product $\underline{E}(\underline{r},t)\underline{E}^*(\underline{r},t)$ and becomes:

$$I(\underline{r},t) = I_t(\underline{r},t)\left[1+\frac{1}{2}m_{0,1}(\underline{r},t)\exp j(\delta\omega_{01}t - \underline{K_{01}}.\underline{r})\right] + c.c \tag{2.9}$$

where $I_t \propto A_0A_0^* + A_1A_1^*$ is the mean intensity (the constant of proportionality is $c\varepsilon_0/4\surd(\varepsilon_r)$ [4]; where c is the speed of light in a vacuum, ε_0 is the permittivity of free space, and ε_r is the relative permittivity)), $m_{01}=2A_0A_1^*/I_t$ is the modulation index,

$\delta\omega_{01} = \omega_0 - \omega_1$ is the frequency difference (that is equal to zero here because there is no frequency difference) and $\underline{K}_{01} = \underline{k}_0 - \underline{k}_1$ is the grating vector.

The problem is now to express the resulting space charge field $\underline{E}$ in terms of the driving intensity (equation 2.9). This is difficult because the equations are nonlinear, therefore the general solution for the space charge field must be a Fourier expansion of the form [5-8]:

$$E(z,t) = \sum_{i=0}^{\infty} \frac{1}{2} E_i(t) \exp j(i \times (\delta\omega t - \underline{K}.\underline{r}) + c.c. \qquad (2.10)$$

The problem of finding the coefficients $E_i(t)$ is not easy; analytic solutions are only possible up to $i=2$ because the algebra becomes prohibitive [9]; Au and Solymar have obtained numerical solutions up to $i=15$ [5], including more terms is impractical because of the longer computing times [1]. An alternative approach to Fourier expansion is followed by Hall *et al.* [10] but their solution is only valid when the photoexcitation and recombination terms are linear. Despite the approximations, their approach shows clearly that the response to large modulation fringes is very nonlinear because a cosinusoidal intensity input generates periodic but clearly non-cosinusoidal electric fields.

A solution can be derived by ignoring the higher harmonic terms generated by the materials equation. The solution is then straightforward and is known as the low modulation solution because the higher harmonic terms are negligibly small only for low intensity fringe modulation [1] where the pump beam intensity is significantly larger than the signal beam intensity.

2.4 Low modulation solutions

Substituting the following trial solutions 2.11 to 2.14

$$N_D^+(\underline{r},t) = N_{D0}^+ + \frac{1}{2}N_{D1}^+(t)\exp j(\delta\omega t - \underline{K}.\underline{r}) + c.c. \tag{2.11}$$

$$n(\underline{r},t) = n_0 + \frac{1}{2}n_1(t)\exp j(\delta\omega t - \underline{K}.\underline{r}) + c.c. \tag{2.12}$$

$$J(\underline{r},t) = J_0 + \frac{1}{2}J_1(t)\exp j(\delta\omega t - \underline{K}.\underline{r}) + c.c. \tag{2.13}$$

$$E(\underline{r},t) = E_0 + \frac{1}{2}E_1(t)\exp j(\delta\omega t - \underline{K}.\underline{r}) + c.c. \tag{2.14}$$

into the material equations 2.4 to 2.6, and eliminating the conduction current density, and neglecting higher harmonic terms, and comparing spatially constant terms and terms in $exp j(\delta\omega t-\underline{K}.\underline{r})$, the following set of equations can be derived:

$$\frac{dN_{D0}^+}{dt} = \frac{dn_0}{dt} = sI_0(N_D - N_{D0}^+) - \gamma_\tau n_0 N_{D0}^+ \tag{2.15}$$

$$0 = n_0 - N_{D0}^+ \tag{2.16}$$

$$j\delta\omega N_{D1}^+ + \frac{dN_{D1}^+}{dt} = smI_0(N_D - N_{D0}^+) - sI_0 N_{D1}^+ - \gamma_\tau(n_0 N_{D1}^+ + n_1 N_{D0}^+) \tag{2.17}$$

$$j\delta\omega n_1 + \frac{dn_1}{dt} = j\delta\omega N_{D1}^+ + \frac{dN_{D1}^+}{dt} + jK\mu(n_0 E_1 + n_1(E_0 + jE_D)) \tag{2.18}$$

$$-jKE_1 = \frac{e}{\varepsilon_s}(N_{D1}^+ - n_1) \tag{2.19}$$

where $K=|\underline{K}|$ and $E_D=Kk_bT/e$. Here E_0 is the externally applied electric field, and E_D is a characteristic field caused by diffusion. From these governing equations the following steady state solutions can be obtained [1]:

$$E_w = \frac{-E_0 - jE_D}{1 + E_D/E_Q + \xi E_0/E_M + j(\xi - E_0/E_Q + \xi E_D/E_M)} \tag{2.20}$$

$$N_{Dw} = \frac{-E_0/E_Q + E_D/E_Q}{1 + E_D/E_Q + \xi E_0/E_M + j(\xi - E_0/E_Q + \xi E_D/E_M)} \qquad (2.21)$$

$$n_w = \frac{1 + j\xi}{1 + E_D/E_Q + \xi E_0/E_M + j(\xi - E_0/E_Q + \xi E_D/E_M)} \qquad (2.22)$$

where ξ is the detuning frequency (the difference in frequency of the input light waves in figure 2.1), and the following normalised quantities are introduced:

$$E_W = \frac{E_1}{m} \qquad N_{DW} = \frac{N^+{}_{D1}}{m} \qquad n_W = \frac{n_1}{m} \qquad (2.23)$$

and

$$E_Q = e\left(n - N_D^+\right)/\varepsilon_s K \qquad (2.24)$$

$$E_M = \gamma_t\left(n - N_D^+\right)/\mu K \qquad (2.25)$$

where *m* is the modulation index ($m = m_{01}$). For a given material the physics depends on the experimental conditions (applied electric field, grating spacing and detuning frequency) and fall into four distinct operating regimes:

- Saturation
- Diffusion
- Drift
- Drift-diffusion.

2.5 The characteristic fields E_D, E_Q, and E_M

The properties of the characteristic fields E_D, E_Q, and E_M need to be addressed at this point as all appear in the above solutions.

$$E_D = \frac{2\pi k_b T}{e\Lambda} \qquad E_Q = \frac{e\left(n - N_D^+\right)\Lambda}{2\pi\varepsilon_s} \qquad E_M = \frac{\gamma_\tau\left(n - N_D^+\right)\Lambda}{2\pi\mu} \qquad (2.26)$$

where Λ is the grating spacing. The diffusion field, E_D, is a function only of grating spacing and temperature: it is inversely proportional to grating spacing and linear in temperature. Both the saturation field, E_Q, and E_M are linear in grating spacing and each depends on a different set of material parameters.

2.6 Diffusion regime

When the applied electric field is much less than the diffusion field, $E_0 << E_D$, the physics is said to be in the diffusion regime. This is true for all my experiments reported in this thesis. Equation 2.20 for the space charge field then becomes (since $E_0 \sim 0$ and $\xi = 0$):

$$E_w = \frac{-E_0 - jE_D}{1 + E_D/E_Q + j\xi(1 + E_D/E_M)} = \frac{-jE_D}{1 + E_D/E_Q} \tag{2.27}$$

The phase angle between the intensity fringes and the space charge field is $\pi/2$ because charge migration is dominated by diffusion. This is shown by plotting equation 2.27 on an Argand diagram, the phase shift between the real and imaginary parts of the space charge field are $\pi/2$. This is the optimum phase angle for two beam coupling [1]. As such diffusion dominated materials have been exploited in this thesis.

2.7 Two beam coupling in Ce:SBN

From equation 2.27, in the absence of an applied field, the space-charge field is therefore determined by thermal diffusion and limited by saturation if the trap density is too low. The effective trap density can be estimated from the Debye screening length which corresponds to the grating spacing for maximum gain [12]:

$$N_A^- = \frac{\varepsilon_s k_B T}{(L_D e / 2\pi)^2} \tag{2.28}$$

where L_D is the Debye screening length. The change in refractive index resulting from an electric field may be expressed in terms of the index ellipsoid [11]. A cross section through this three dimensional surface allows the indices of refraction of two mutually orthogonal polarisations to be determined. The general expression for the index ellipsoid in the presence of an applied electric field takes the form:

$$\left(\frac{1}{n^2}\right)_1 x^2+\left(\frac{1}{n^2}\right)_2 y^2+\left(\frac{1}{n^2}\right)_3 z^2+2\left(\frac{1}{n^2}\right)_4 yz+2\left(\frac{1}{n^2}\right)_5 xz+2\left(\frac{1}{n^2}\right)_6 xy=1 \quad (2.29)$$

Where the change in the coefficients $(1/n^2)_i$ due to an electric field E_j, is defined as

$$\Delta\left(\frac{1}{n^2}\right)_i=\sum_{j=1}^{3} r_{ij}E_j \quad (2.30)$$

Where $i=1..6$ and $j=1..3$. The 6x3 tensor r_{ij} is called the electro-optic tensor. Substituting equation 2.30 into the following differential equation

$$dn=-\left(\frac{n^3}{2}\right)d\left(\frac{1}{n^2}\right) \quad (2.31)$$

And reducing the electro-optic tensor to a scalar quantity r_{eff}, and effective electro-optic coefficient which is a linear combination of the tensor elements, the refractive index change induced by an applied electric field of magnitude E may be written

$$\Delta n=-\frac{1}{2}r_{eff}n^3E \quad (2.32)$$

The exponential small signal gain coefficient, Γ, is given by [11]

$$\Gamma=-\frac{4\pi}{\lambda}\Delta n=\frac{2\pi}{\lambda}n^3 r_{eff}\, Im(E_w) \quad (2.33)$$

Where n is the refractive index and $Im(E_w)$ is the imaginary part of the space-charge field. The phase shift between the optical interference pattern and the refractive index grating is given by the argument of the space-charge field. For zero applied field, the phase shift in Ce:SBN is 90° for all grating spacings. The effective electrooptic coefficient, r_{eff}, for extraordinarily polarised light and the pump and signal beam bisector normal to the c-axis is given by [13]

$$r_{eff}=r_{33}\cos^2(\theta)-r_{13}\sin^2(\theta)+\left(\frac{n_e-n_o}{n_e}\right)(r_{33}-r_{13})\sin^2(2\theta) \quad (2.34)$$

where θ is the intersection half angle of the internal pump and signal beams. For SBN, $r_{33} = 235$pm/V and $r_{13} = 47$pm/V [14]. The gain, G, is defined as the signal amplitude with the pump beam present divided by the signal amplitude with the pump beam absent. In the undepleted pump regime, the small signal gain coefficient, Γ, is given by

$$\Gamma = \frac{1}{L_{SBN}} \log G = \frac{2\pi}{\lambda} n^3 r_{eff}\, Im(E_w)$$

$$\therefore G = \exp\left[\frac{2\pi L_{SBN}}{\lambda} n^3 r_{eff}\, Im(E_w)\right] \tag{2.35}$$

where L_{SBN}, is the optical path length of the Ce:SBN window. Using the above equations, the small signal gain characteristics of a Ce:SBN window have been calculated, figure 2.2. A Debye screening length of 1.6μm and an effective trap density of 4.3×10^{15} cm^{-3} have been used, based on values from [13].

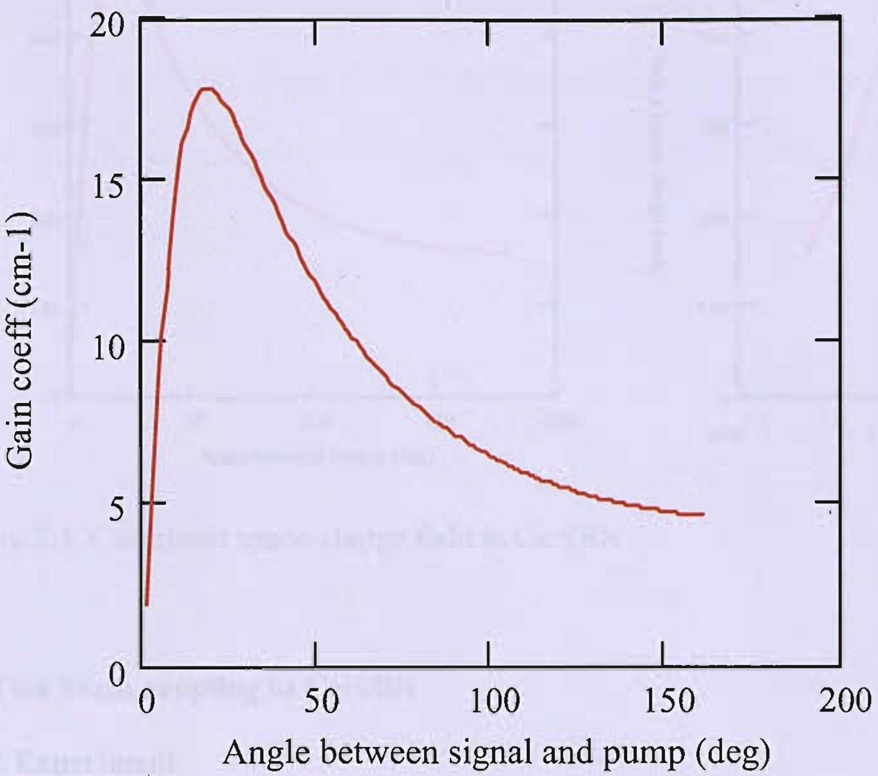

Figure 2.2. Small signal gain characteristics of a Ce:SBN window.

The gain characteristic can be explained in terms of the saturation field. Although the diffusion field, E_D, varies inversely with grating spacing, the saturation field, E_Q, varies proportionally with the grating spacing and limits the magnitude of the space-charge field explaining its reduction at higher beam angles (at finer grating spacings). A higher effective trap density would allow a stronger space-charge field to be achieved at finer grating spacings. From equation 2.35 and using the experimentally determined Debye screening length, the calculated Ce:SBN space-charge field as a function of beam angle and grating spacing for equal signal and pump powers is shown in figure 2.3.

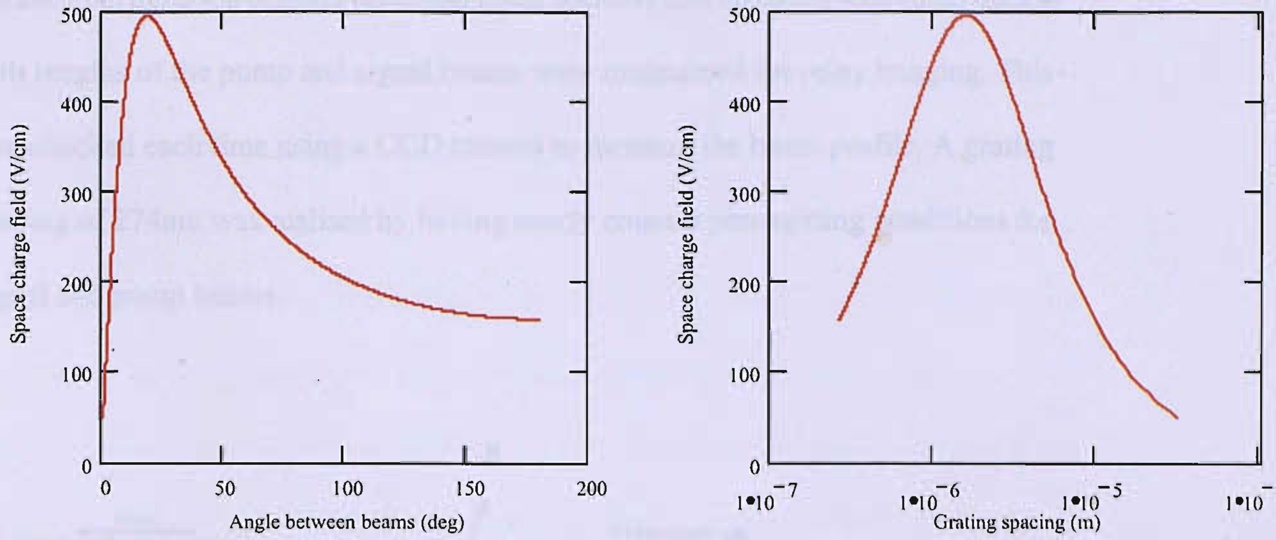

Figure 2.3. Calculated space-charge field in Ce:SBN

2.8 Two beam coupling in Ce:SBN

2.8.1 Experiment

The two beam coupling experimental arrangement is shown in figure 2.4. A relay imaging scheme was used to avoid variations in the transverse beam intensity profile. The 532nm continuous wave 5W Verdi laser (coherence length of ~5m) was first pre-expanded to overfill a 1mm diameter aperture, producing a uniform "top-hat" beam. This aperture was relay imaged with unity magnification using a 300mm focal length bi-convex lens placed 600mm (2f) from the uniformly illuminated aperture. The path lengths of the signal and pump beams between the relay image lens and the 1mm thick Ce:SBN window were matched and adjusted to 600mm to produce a diffraction free spot at the image plane (a "top hat" intensity profile). The laser power was adjusted with neutral density filters to produce a local signal intensity of 1W cm^{-2} at the input face. The ratio between the pump and signal beam was ~0.002. The crystal c-axis was parallel to the y-axis in figure 2.4. The laser light was p-polarised (also parallel to the y-axis). The angle between the beams was varied by changing the distance between the mirrors (after the beam splitter) and ensuring that equal optical path lengths of the pump and signal beams were maintained for relay imaging. This was checked each time using a CCD camera to measure the beam profile. A grating spacing of 274nm was realised by having nearly counter propagating conditions for signal and pump beams.

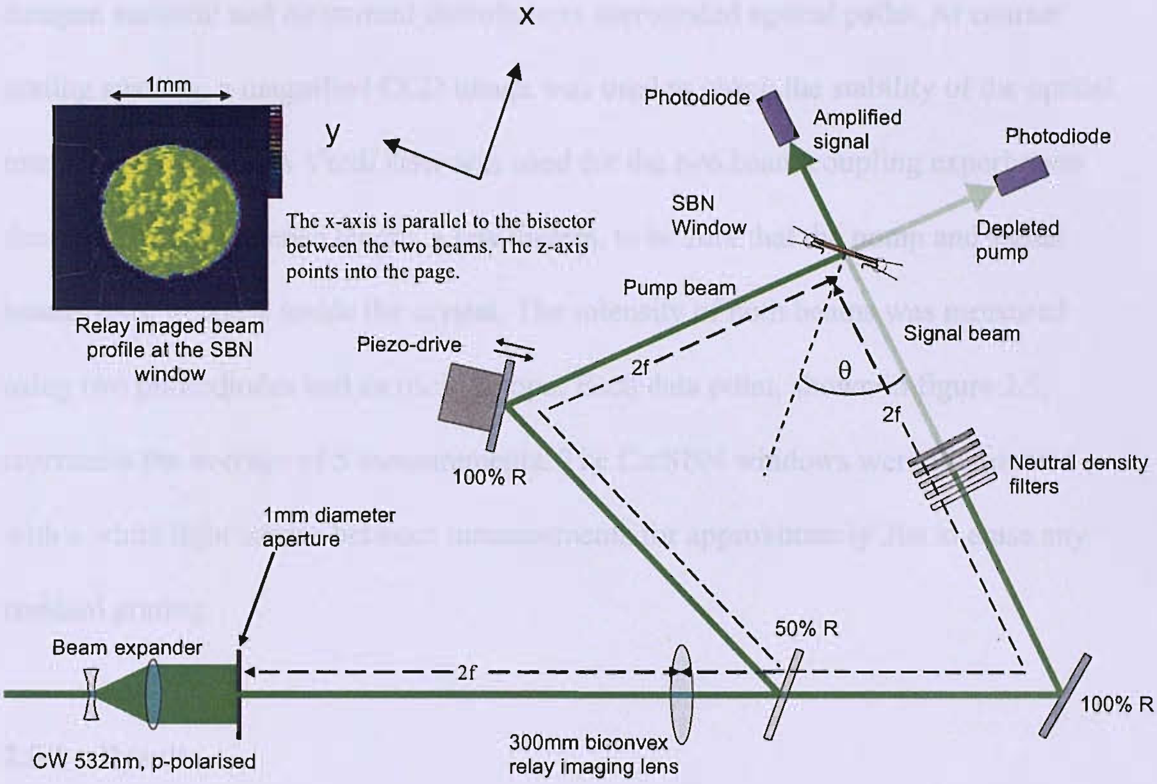

Figure 2.4. Experimental layout and the co-ordinate system used.

A piezo-electrically driven mirror imparts a controlled transient phase shift to the pump beam. The voltage required to move the intensity fringes by 2π was first determined for each grating spacing using a CCD camera to examine the fringes *in situ*. The maximum gain occurs for a π/2 phase shift. The actual grating phase shift was determined by measuring the mirror voltage required to maximize the gain and the intrinsic phase shift is $\pi/2$ minus the applied phase shift needed to maximize the gain. Because the gain of the Ce:SBN windows varied slightly with position across the cell face, a mask was used to ensure all gain measurements were repeated at exactly the same relative position on the window face. The optical path was passively stabilized during the experiment and all measurements were taken without any source of vibration on the optical table (e.g. oscilloscopes with cooling fans). Packing to dampen acoustic and air current disturbances surrounded optical paths. At coarser grating spacing, a magnified CCD image was used to check the stability of the optical interference pattern. A Verdi laser was used for the two beam coupling experiments due to its long coherence length, a few meters, to be sure that the pump and signal beams were in phase inside the crystal. The intensity of both beams was measured using two photodiodes and an oscilloscope. Each data point, shown in figure 2.5, represents the average of 5 measurements. The Ce:SBN windows were illuminated with a white light source between measurements for approximately 20s to erase any residual grating.

2.8.2 Results

The background small signal gain measurements for the individual windows are shown in figure 2.5. A maximum gain of about 17.4 was measured for a beam separation angle of about 20° (equivalent to a grating spacing of about 1.5μm) in good agreement with [13]. The theoretical fit, also shown in figure 2.5, assumed a Debye screening length of 1.6μm and an effective trap density of 4.3×10^{15} cm^{-3} in agreement with [13].

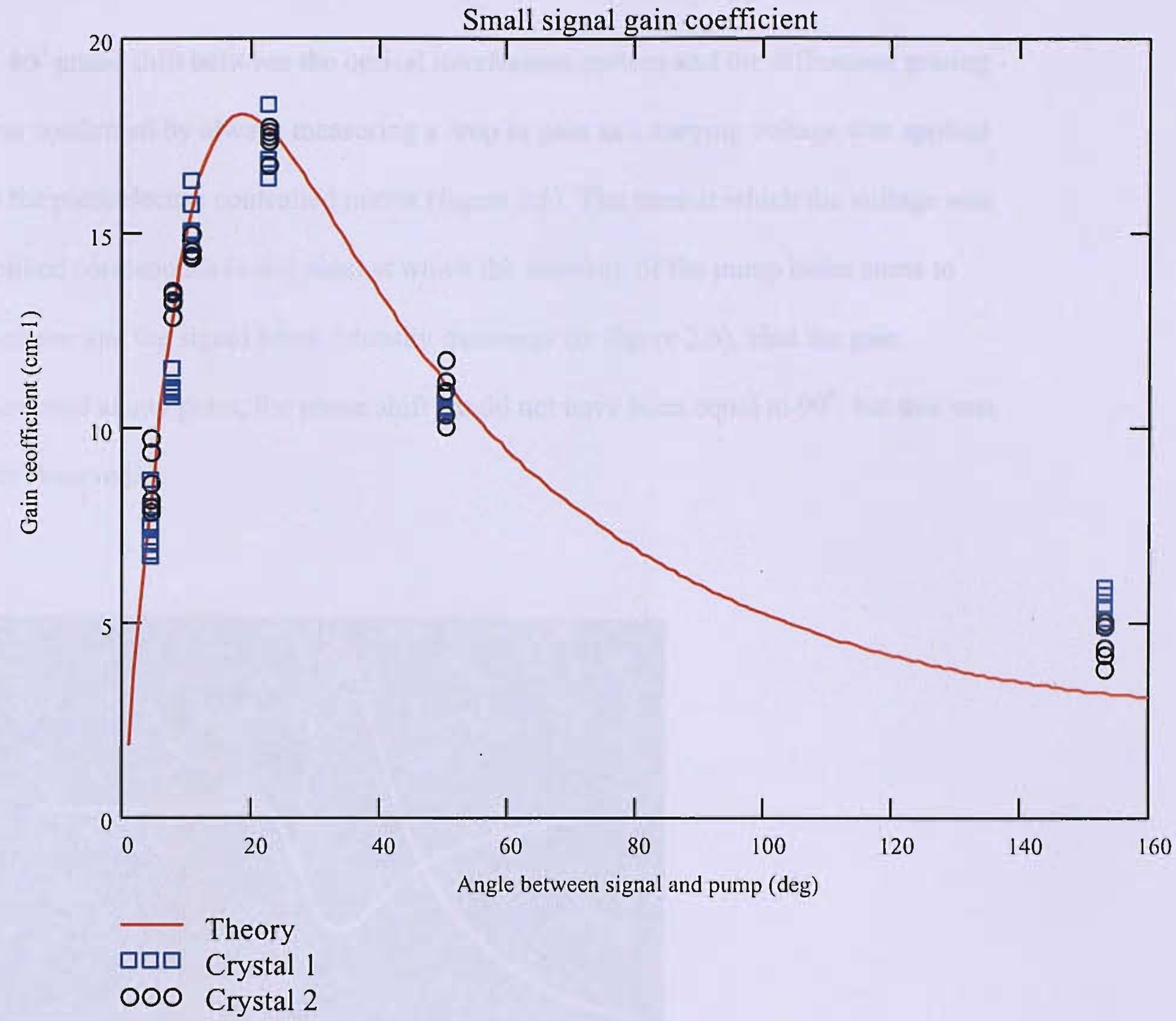

Figure 2.5. Small signal gain characteristics of the Ce:SBN windows.

The spread in data points between the two Ce:SBN windows is unexpected since they come from the same crystal boule and have the same dopant concentration. This spread is likely to be due to non-uniformities within the crystals such as varying trap densities. This is an issue that is discussed in chapter 7. The measured gain at 155^0 was higher than that predicted by theory. This is likely to be due to the increased path length of the laser light inside the crystal at larger beam intersectional angles so that the input laser light experiences a longer gain region.

A 90^0 phase shift between the optical interference pattern and the diffraction grating was confirmed by always measuring a drop in gain as a varying voltage was applied to the piezoelectric controlled mirror (figure 2.6). The time at which the voltage was applied corresponds to the point at which the intensity of the pump beam starts to increase and the signal beam intensity decreases (in figure 2.6). Had the gain increased at any point, the phase shift would not have been equal to 90^0, but this was not observed.

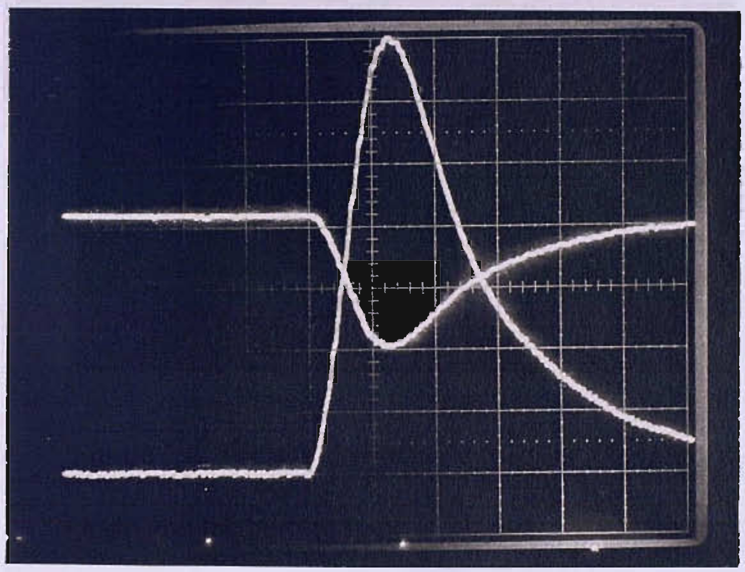

Figure 2.6. The small signal intensity as a function of time. The top trace is the signal beam and the bottom trace is the pump beam (time base 100ms/division).

A 1/e response time of ~120ms was measured, figure 2.7, at a beam intersection angle of 22.0^0. The trace was obtained by erasing any residual gratings with a white light source then allowing the signal beam through the crystal. A shutter was then used to allow the pump beam through the crystal, corresponding to the peak intensity in figure

2.7, the intensity then dropped off as energy was coupled into the signal beam via the photorefractive effect.

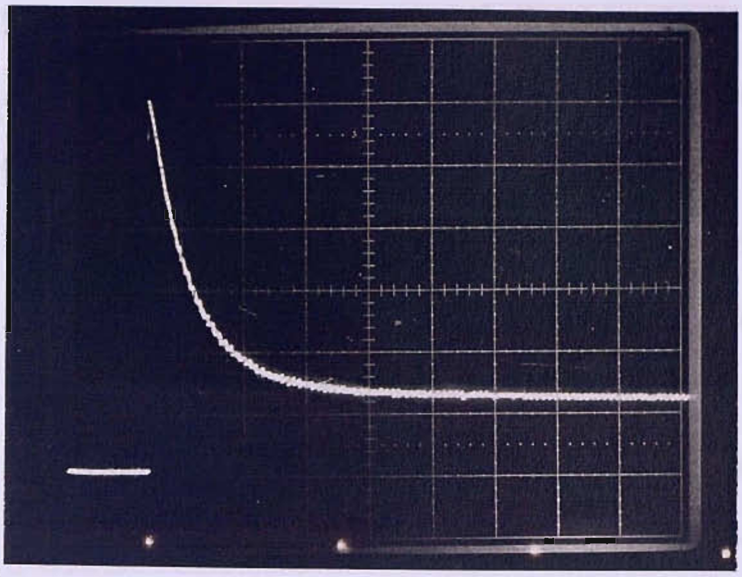

Figure 2.7. The small signal intensity as a function of time for a Ce:SBN window (100ms/div time base).

2.9 Conclusion

The photorefractive effect in Ce:SBN has been characterised using a two beam coupling experiment. The small signal gain has been measured as a function of grating period and found to be in good agreement with theory derived from the standard Kukhtarev equations. The gain was measured over a grating spacing range of 274nm-7µm using 532nm-wavelength continuous wave laser light. A peak small signal gain of ~17.4cm^{-1} was measured at a grating spacing of 1.5 µm. In the next chapter I will use the two Ce:SBN crystals to fabricate an inorganic-organic photorefractive hybrid device.

2.10 References

[1] D.C. Jones, *Wave Interactions in Photorefractive Materials*, DPhil thesis, University of Oxford (1989).

[2] N. V. Kukhtarev, V. B. Markov, S. G. Odulov, M. S. Soskin, V. L. Vinetskii, *Holographic storage in electro-optic crystals. I. Steady state*, Ferroelectrics. 22, 949-960, (1979).

[3] N.V. Kukhtarev, V. B. Markov, S. G. Odulov, M. S. Soskin, V. L. Vinetskii, *Holographic storage in electro-optic crystals. II Beam coupling-light amplification*, Ferroelectrics, **22**, 961-964, (1979).

[4] E. Hecht and A. Zajac, *Optics*, Addison-Wesley Publishing Co. (1979).

[5] L.B. Au and L. Solymar, *Space charge field in photorefractive materials at large modulation*, Optics Letters, **13(8),** 660-662 (1988).

[6] E. Ochoa F. Vachss, and L. Hesselink, *Higher order analysis of the photorefractive effect for large modulation depths*, Journal of the optical society of America A, 3(2), 181-187 (1986).

[7] F. Vachss and L. Hesselink, *Selective enhancement of spatial harmonics of a photorefractive grating*, Journal of the optical society of America B, **5(8)**, 1814-1821 (1988).

[8] F. Vachss and L. Hesselink, *Nonlinear photorefractive response at high modulation depths*, Journal of the optical society of America B, **5(5)**, 690-701 (1988).

[9] P. Refregier, *Two beam coupling in photorefractive $Bi_{12}SiO_{20}$ crystals with moving grating: theory and experiments*, Journal of Applied Physics, **58(1),** 45-57 (1985).

[10] T. Hall, R. Jaura, L. M. Connors, and P. D. Foote, *The photorefractive effect-a review*, Quantum electronics, 10, 77-146 (1985).

[11] Solymar L, Webb D J and Grunnet-Jepsen A, *The physics and applications of photorefractive materials*, Oxford series in optical and imaging science 11, Clarendon Press (1996).

[12] Ewbank M D, Vazquez R A, Neurgaonkar R R and Vachss F, *Contradirectional two-beam coupling in absorptive photorefractive materials: application to Rh-doped strontium barium niobate (SBN:60)*, J. Optical Society of America, **B12,** 87-98 (1995).

[13] Ewbank M D, Neurgaonkar R R and Cory W K, *Photorefractive properties of strontium-barium niobate*, J. Applied Physics, **62,** 374-380 (1987).

Chapter 3 - Inorganic-organic photorefractive hybrid

In this chapter, a liquid crystal layer is used to accentuate the gain from an inorganic photorefractive window. The hybrid photorefractive approach that has been explained in chapter 1 exploits the attractive properties of inorganic crystals and promotes higher overall gain that is available from either device alone. The influence of the space charge field, developed in the inorganic material, upon a liquid crystal layer is described and modelled to make quantitative predictions about the enhanced nonlinear response. A number of hybrid cells with different liquid crystals and alignment layers' are fabricated and characterised. The results demonstrate the enhanced performance. However some of the results were unexpected and these are discussed.

3.1 Preparation of Ce:SBN hybrid cell

The Ce:SBN windows characterised in chapter 2 were used in the experiments reported here. The windows were 20mm x 20mm x 1mm in size with c-axes aligned parallel to one of the 20mm edges. Charge migration is dominated by diffusion in SBN ensuring a 90^{o} phase shift between the interference pattern and the space-charge field at all grating spacings. The lack of optical activity and photovoltaic fields reduces experimental complications and simplifies theoretical estimates of the surface space-charge fields.

The interior surfaces of the Ce:SBN windows were first coated with an appropriate alignment layer. For homeotropically alignment a dilute solution (~0.125 weight % in ethanol) of either HTAB (Hexadecyltrimethylamonium bromide) or Quillon S (Octadecanoata chromic chloride hydroxide) was used. For planar alignment a solution of 0.2mg of PVK (polyvinylcarbazole, average molecular weight of

1,100,000) dissolved in 10mL of chlorobenzene was used. The windows were then spin coated at 5000rpm for 30 seconds and subsequently oven-dried for two hours at temperatures below 50°C (to avoid exceeding the Curie temperature of Ce:SBN, approximately 65°C). When dry, the PVK coated windows were uniaxially rubbed using a velour coated roller. The planar rubbed cell windows were assembled with the rubbing directions anti-parallel to each other to avoid molecular alignment discontinuities arising from any surface molecular tilt. PVK was used in preference to other polymers such as PVA (polyvinyl alcohol) or polyimide because it is robust to rubbing and easy to apply and remove using solvents. Once coated, the cells were assembled with the crystal c-axes parallel to the window edge and perpendicular to the 12.5μm thick copper foil spacers, as shown in figure 3.1.

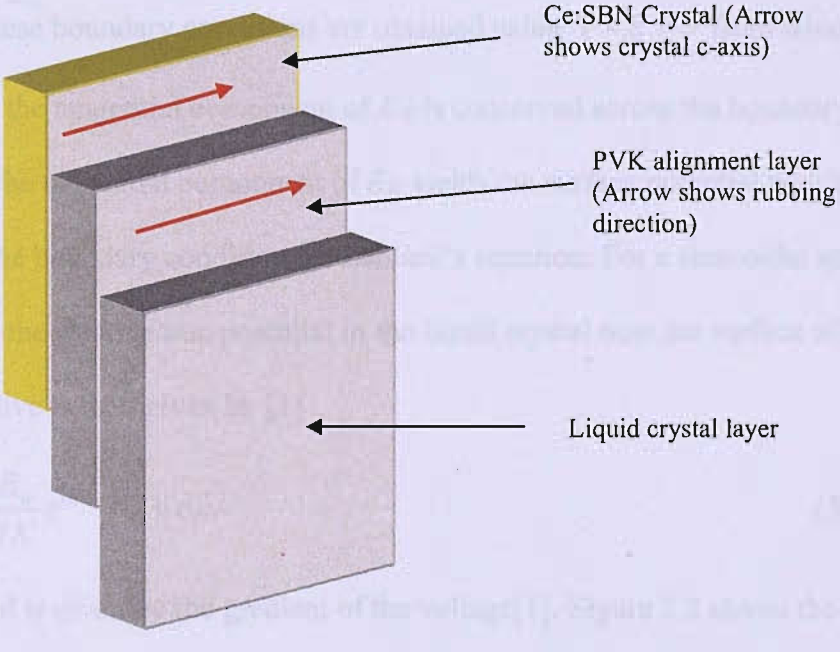

Figure 3.1 Hybrid cell cross-section.

The foil was rolled between a glass cylinder and a glass plate prior to assembly to remove any edge burrs. The spacers extended beyond the ends of the cell allowing it to be trapped between the clips and the cell windows so transverse electric fields could be applied by connecting to the clips rather than the fragile foil. The cells were filled with LC by capillary action through the exposed gap between the two spacer ends of the cell. The pre-tilt of the LC molecules on PVK was 0^0.

3.2 Surface field development and liquid crystal response to surface fields

During two beam coupling in the hybrid cell, a space charge field is developed within the bulk of the photorefractive crystal. This space charge field has a decaying evanescent component in the liquid crystal layer that can be calculated through Maxwell's equation $\nabla \cdot \underline{D} = \rho$. Assuming there are no free charges in the nematic liquid crystal, the above equation leads to Laplace's equation $\nabla^2 V = 0$ where V is the electrostatic potential. This must be solved subject to boundary conditions at the two surfaces. These boundary conditions are obtained using $\nabla \times \underline{E} = 0$ from which it follows that the tangential component of E_W is conserved across the boundary. Integrating the tangential component of E_W yields the surface potential which can then be used as the boundary condition for Laplace's equation. For a sinusoidal space-charge field the electrostatic potential in the liquid crystal near the surface of the photorefractive is then given by [1]

$$V(x,y) = \frac{iE_w}{2K} e^{(iKy - Kx)} + c.c. \qquad (3.1)$$

And the field is given by the gradient of the voltage[1]. Figure 3.2 shows the normalised voltage and field plots for a sinusoidal space-charge field, assuming there are no free charges in the liquid crystal layer. Note that the penetration depth of the field is proportional to the grating spacing and penetrates into the liquid crystal layer with an exponential decay constant of $2\pi/\Lambda$.

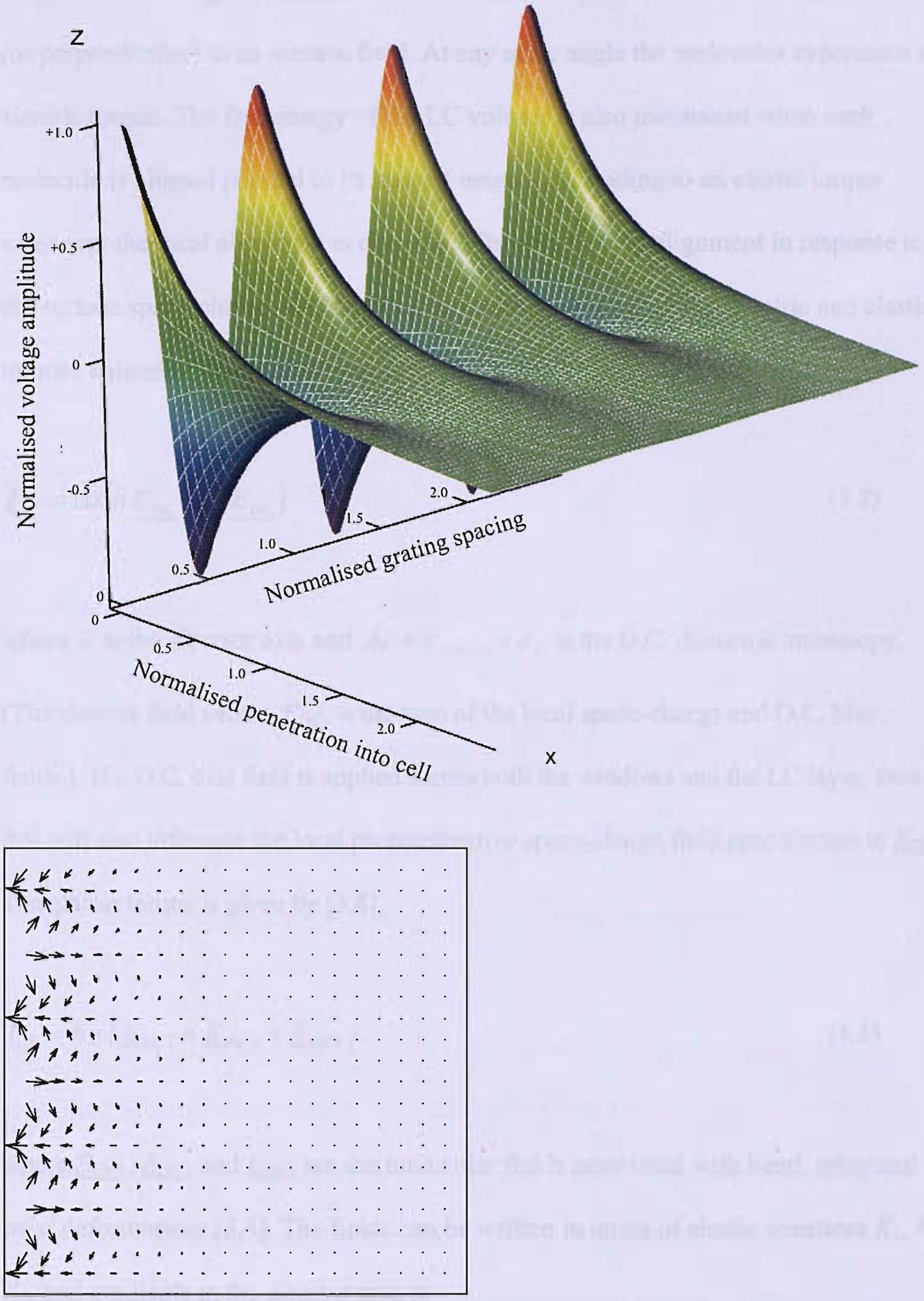

Figure 3.2. Normalized voltage (above) and field (below) plots for a sinusoidal space-charge field in free space.

The potential energy of nematic LCs is minimised when the molecules align parallel (or perpendicular) to an electric field. At any other angle the molecules experience an electric torque. The free energy of the LC volume is also minimised when each molecule is aligned parallel to its nearest neighbour, leading to an elastic torque whenever the local alignment is distorted. The steady state alignment in response to the surface space-charge field reaches equilibrium when the local electric and elastic torques balance. The electric torque, $\underline{F}_E$, is given by [3,4]

$$\underline{F}_E = \Delta\varepsilon\left(\hat{n}.\underline{E_{DC}}\right)\left(\hat{n}\times\underline{E_{DC}}\right) \tag{3.2}$$

where $\hat{n}$ is the director axis and $\Delta\varepsilon = \varepsilon_{parallel} - \varepsilon_{\perp}$ is the D.C. dielectric anisotropy. (The electric field vector, $\underline{E_{DC}}$, is the sum of the local space-charge and D.C. bias fields.) If a D.C. bias field is applied across both the windows and the LC layer, then this will also influence the local photorefractive space-charge field contribution to $\underline{E_{DC}}$. The elastic torque is given by [3,4]

$$\underline{F}_L = \hat{n}\times(\underline{E}_{DC1} + \underline{E}_{DC2} + \underline{E}_{DC3}) \tag{3.3}$$

where $\underline{E_{DC1}}$, $\underline{E_{DC2}}$ and $\underline{E_{DC3}}$ are the molecular fields associated with bend, splay and twist deformations [3,4]. The fields can be written in terms of elastic constants K_1, K_2, K_3, and gradients in the director axis as

$$\underline{E_{DC1}} = K_1\nabla\left(\nabla\cdot\underline{n}\right) \tag{3.4}$$

$$\underline{E_{DC2}} = -K_2\left[A \times \underline{n} + \nabla \times \left(A\underline{n}\right)\right] \tag{3.5}$$

$$\underline{E_{DC3}} = K_3\left[\underline{B} \times \left(\nabla \times \underline{n}\right) + \nabla \times \left(\underline{n} \times B\right)\right] \tag{3.6}$$

Where

$$A = \underline{n} \cdot \left(\nabla \times \underline{n}\right) \tag{3.7}$$

$$\underline{B} = \underline{n} \times \left(\nabla \times \underline{n}\right) \tag{3.8}$$

The local refractive index, *n(x,y)*, of the liquid crystal is modulated according to [3]

$$n(x,y) = \frac{n_0 n_e}{\sqrt{n_0^2 \sin^2(\beta \pm \Phi) + n_e^2 \cos^2(\beta \pm \Phi)}} \tag{3.9}$$

where β is the angle between the beam (signal or pump) and the unperturbed molecular director axis and Φ is the space-charge induced angular tilt.

When the molecular alignment is normal (homeotropic) or parallel (planar) to the cell windows, the index modulation of the LC is independent of the sign of the local space-charge field (assuming the refractive index is symmetric about the molecular director). Under these circumstances, the refractive index profile of the LC layer has twice the spatial frequency of the optical interference pattern, see figure 3.3 (top), causing the diffracted beams to emerge from the cell at angles greater than the incident writing beams. To avoid this, the symmetry of the molecular alignment must be broken by introducing a molecular tilt, see figure 3.3 (bottom), enabling the refractive index modulation to follow the sign of the local space-charge field and generate an index grating with the same spatial frequency as the optical interference pattern. Ideally, the relative direction of the tilt should be chosen such that the local variations of the liquid crystal and window refractive indices are spatially matched, enabling the LC to add to, rather than subtract from the refractive index modulation of the window. This might be affected electrically by applying a transverse D.C. field to the cell causing the liquid crystal molecules to tilt assuming strong anchoring conditions, or in the case of planar alignment, by rubbing the surfaces of the windows at an angle of 45° to the c-axis orientation so that the LC molecules present an asymmetry.

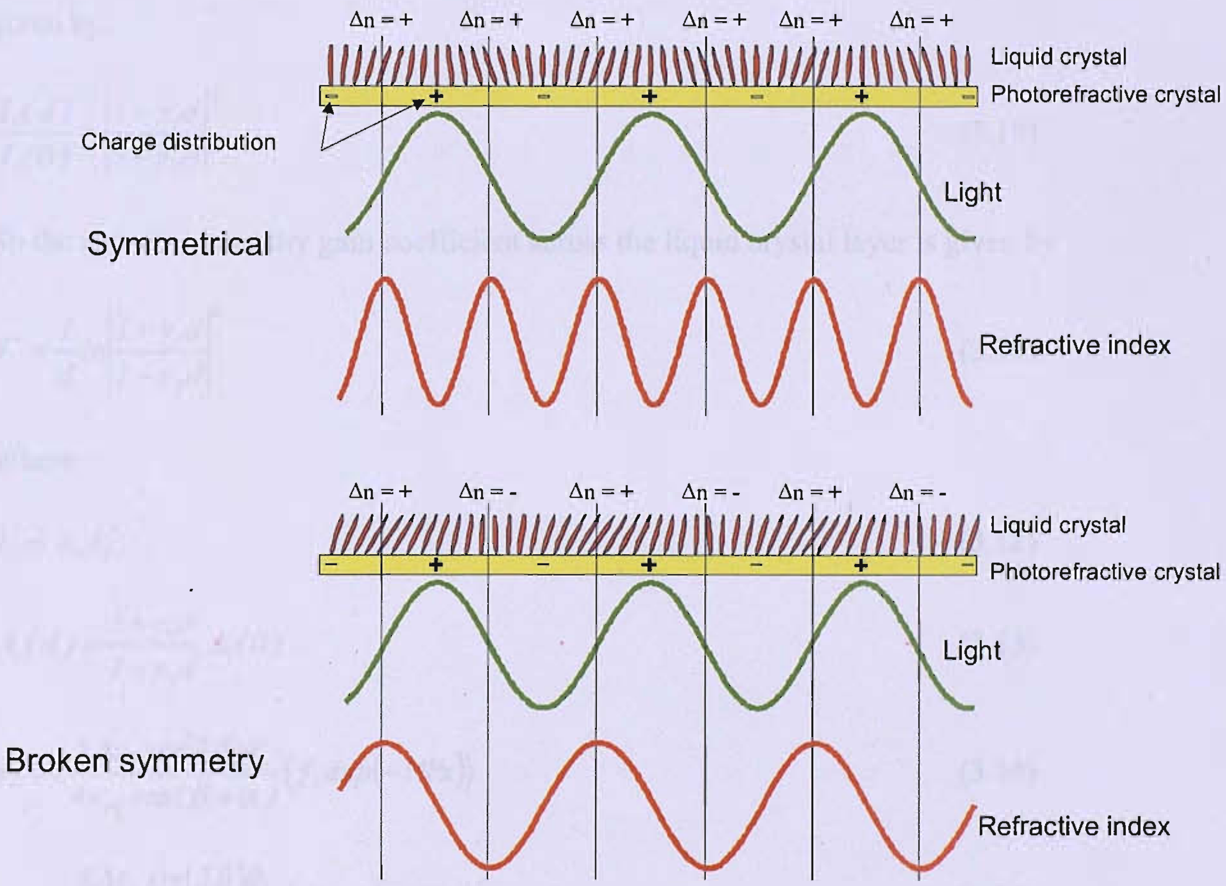

Figure 3.3. Effect of molecular alignment symmetry in the liquid crystal layer

3.3 Two beam coupling in a photorefractive hybrid

An analytical solution for beam coupling in a hybrid photorefractive liquid crystal cell has been developed [5] that offers a route to quantitative gain predictions. The hybrid cell model considers layer(s) of undoped nematic liquid crystal contained between wafers of photorefractive crystal or photoconductors. Reference 5 assumes reorientation of the liquid crystal by the evanescent component of the space charge field propagation from the photorefractive layers, leading to a modulation of the liquid crystal refractive index in the physical way described in the previous sections of this chapter. Coupled wave theory is used to derive the small signal gain as a function of the liquid crystal parameters. The resulting small signal intensity gain is given by:

$$\frac{I_1(d)}{I_1(0)} = \left| \frac{1+\gamma_1 d}{1-\gamma_2 d} \right|^2 \tag{3.10}$$

So the apparent intensity gain coefficient across the liquid crystal layer is given by

$$\Gamma = \frac{1}{d} ln \left| \frac{1+\gamma_1 d}{1-\gamma_2 d} \right|^2 \tag{3.11}$$

Where

$$I_1 = A_1 A_1^* \tag{3.12}$$

$$A_1(d) = \frac{1+\gamma_1 d}{1-\gamma_2 d} A_1(0) \tag{3.13}$$

$$\gamma_1 = i \frac{k \Delta\varepsilon_r \sin(2\beta)\theta_1}{4\varepsilon_{r0} \cos(\beta+\alpha)} \langle f_1 \exp(-i\Psi x) \rangle \tag{3.14}$$

$$\gamma_2 = i \frac{k \Delta\varepsilon_r \sin(2\beta)\theta_1}{4\varepsilon_{r0} \cos(\beta+\alpha)} \langle f_1 \exp(-i\Psi x) \rangle^* \tag{3.15}$$

And

$$\langle f_1 \, exp(-i\Psi x)\rangle = \frac{1}{d}\int_{x=0}^{d} exp(-i\Psi x) f_1(x)dx$$

$$= \frac{K}{d}\frac{exp(1-i\Psi d)}{(exp(2Kd)-1)^2(K-i\Psi)^2(K+i\Psi)^2}\left\{\begin{array}{l} exp(4Kd+i\Psi)(K-i\Psi)^2+exp(i\Psi d)(\Psi-iK)^2 \\ -2\,exp(3Kd)\left[K^2+K^3d-\Psi^2+kd\Psi^2\right] \\ -2\,exp(Kd)\left[-K^2+K^3d+\Psi^2+kd\Psi^2\right] \\ +4K\,exp(2Kd+i\Psi d)\left[(K^2+\Psi^2)d+i\Psi\right] \end{array}\right\}$$

(3.16)

Using equations (3.10-3.16) the small signal gain has been calculated for a hybrid cell comprised of a 3mm photorefractive substrate that is diffusion dominated (e.g. Ce:SBN), an E7 liquid crystal layer, and with a 100nm rubbed polymer alignment layer between the liquid crystal and the photorefractive layer. The Mathematica code used to calculate the gain has been included in appendix 3.1. The relevant material parameters are $\Delta\varepsilon_s = 13.8\varepsilon_0$ (the change in static dielectric constant), $n_0=1.5211$, $n_e=1.7464$, *and* $K_e= 8.2\ pN$ (the elastic constant of the LC molecules)[6].

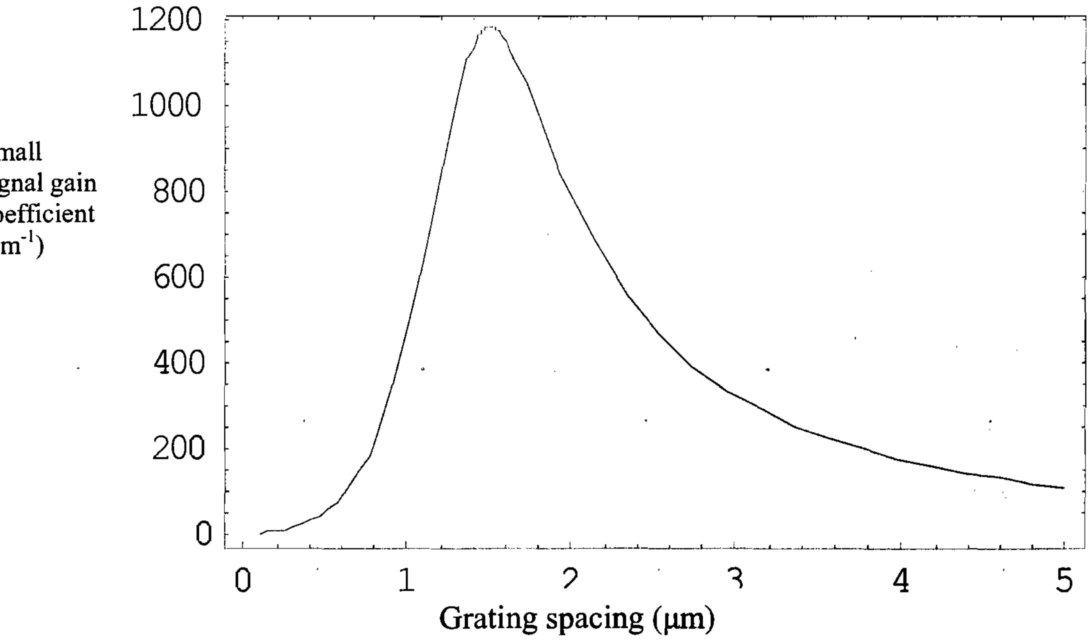

Figure 3.4. The theoretical plot of the small signal gain coefficient as a function of grating spacing for a hybrid photorefractive.

Thus, peak gain co-efficients in the region of ~1200 cm^{-1} are predicted. Caution must be taken as the model assumes small beam intersection angles, strong anchoring conditions with respect to the liquid crystal molecules on the photorefractive window surfaces, and that the internal space charge in the photorefractive is unperturbed by surface effects. Also the derived analytical solution is not exact due to simplification of the torque balance equation [5] by assuming equal values of the bend and splay elastic constants.

3.4 Experimental procedure

The experimental arrangement used to measure the two-beam coupling gain is identical to that described in chapter 2, shown in figure 2.3. The hybrid cell was mounted on an x-y-z translation stage, fitted with a rotation mount allowing lateral translation of the cell during the experiment and placement of the LC interface directly at the point of beam overlap. Etalon effects from the refractive index mismatch between the windows and the LC layer caused the amplified signal beam transmission to vary with cell angle. The cell was nominally aligned normal to the bisector between the two beams the cell angle was adjusted using the rotation stage to maximize the transmission of the amplified signal beam. At low liquid crystal gains, and when the cell was empty, the etalon effects were negligible. However, at high gain the etalon effect became pronounced and careful adjustment was needed to obtain accurate gain measurements (this effect should diminish in a properly engineered cell equipped with anti-reflection coatings). The etalon effect has been noted previously for other high gain photorefractive systems [7].

The gain of the Ce:SBN windows varied slightly with position across the cell face, so a mask was used to ensure all gain measurements were repeated at exactly the same position on the hybrid cell face. An accurate determination of the local window gain for each new measurement set was essential to determine the gain contribution from the liquid crystal layer. Each time a new cell was constructed, the gain characteristics of the empty cell as a function of angle were first measured. The total gain of the filled cell divided by the empty cell gave the gain contribution from the LC layer. For each beam angle and LC system, a simple glass cell of identical thickness and LC alignment was substituted for the hybrid cell to check whether any of the net gain from the hybrid cell arose from direct optical field interaction with the LC system or from induced thermal effects. In all of the experiments no beam coupling, diffraction, scattering or beam degradation was observed; all of the LC gain came exclusively from the Ce:SBN space-charge field induced molecular realignment.

3.5 Results and discussion

3.5.1 Homeotropically aligned hybrid cells

The homeotropically aligned cells were fabricated (with HTAB or Quillon S surfactants) using 5CB, E7 and TL203 LCs. A summary of the LC parameters used is given in table 3.1.

Liquid Crystal	**Nematic to isotropic phase transition temperature (C^0)**	**Birefringence**
5CB	35	0.2
E7	58.2	0.2
TL203	77.4	0.205

Table 3.1. The phase transition temperature and birefringence for the 3 liquid crystals used in this work.

The best performance was obtained for HTAB with 5CB at zero applied volts which gave a maximum cell gain of 160 for an angular beam separation of 14.5°, corresponding to a grating spacing of 2.1μm. At this grating spacing, the combined small signal gain from the two windows was ~ 30 (twice that of a single window). This is equivalent to a small signal gain coefficient of $17cm^{-1}$, using equation 2.35 ($1/(1x10^{-3}x2))x(\ln(30))x(1/100) \sim 17cm^{-1}$). A gain contribution of about 5.3 therefore arises from the 5CB LC (dividing the total gain for the filled cell, 160, by that of the two SBN windows, 30), equivalent to an exponential gain coefficient of about $1300\ cm^{-1}$, using equation 2.35 ($1/(12.5x10^{-6}))x(\ln(5.3))x(1/100) \sim 1300\ cm^{-1}$). Figure 3.5 compares the gain and small signal gain coefficients for the empty cell and the 5CB LC respectively. The peak LC gain occurred at a grating spacing of ~ 2μm, while the peak gain for the Ce:SBN occurred at about 1.6μm. The other combinations which are tabulated in table 3.2 showed similar characteristics, but with lower overall gain. The poorest combination was HTAB and TL203 which generated a maximum LC gain of ~ 1.7 with a 2μm grating spacing, corresponding to a small signal gain coefficient of about $400\ cm^{-1}$.

Peak small signal gain coefficient (cm^{-1})	**Optimum grating spacing (μm)**	**Liquid crystal**	**Alignment layer**
1300	2.0	5CB	HTAB
1650	2.0	E7	PVK
400	2.0	TL203	HTAB

Table 3.2. A summary of the measured peak small signal gain coefficients.

It should be noted that although the gain is justified for the hybrid system, the calculated gain coefficients that represent the gain per unit length might be misleading because the calculation assumes that there is equal gain over the whole length in the hybrid. This is likely to be incorrect due to the non-linear nature of the space charge field which is stronger nearer the surface of the photorefractive. Consequently, more real information about where the gain is occurring is needed.

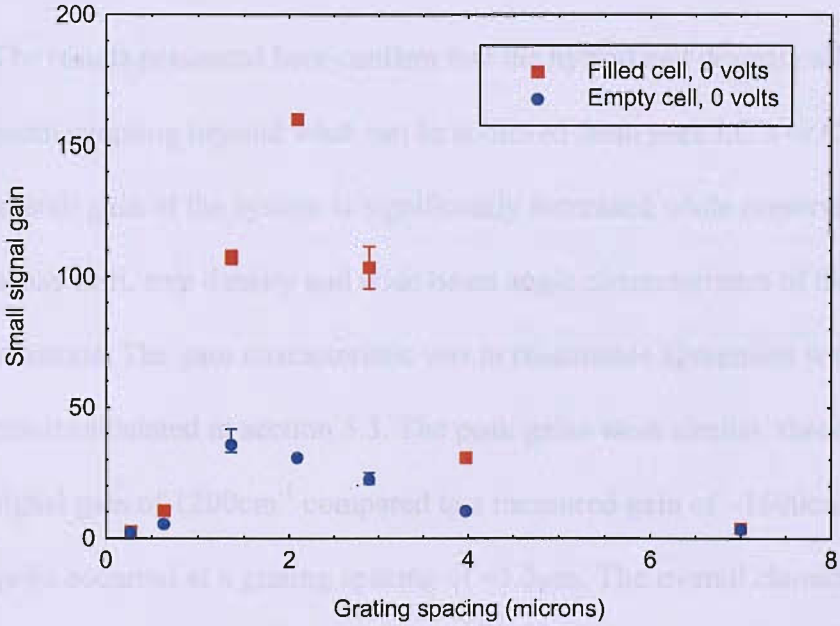

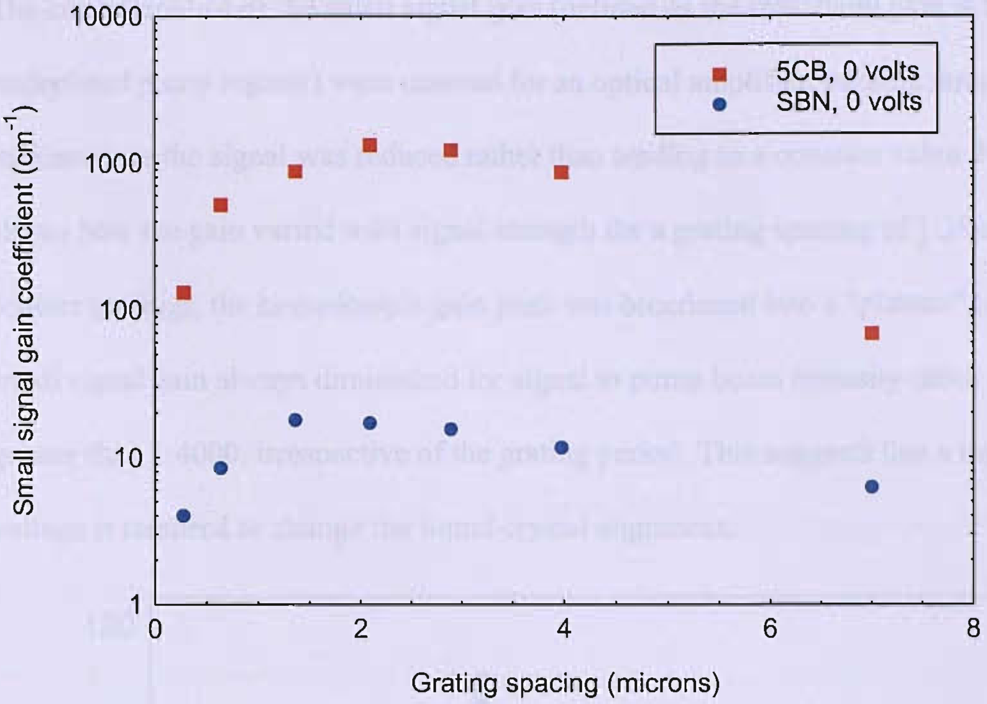

Figure 3.5. Gain characteristic (small signal gain and small signal gain coefficient) characteristic versus grating spacing for a homeotropically aligned hybrid cell, red data points, (HTAB/5CB/Ce:SBN) compared with an empty cell, blue data points.

The results presented here confirm that the hybrid cell dramatically enhances the two beam coupling beyond what can be achieved from pure LC's or Ce:SBN alone. The overall gain of the system is significantly increased while preserving the desirable phase shift, trap density and wide beam angle characteristics of the inorganic substrate. The gain characteristic was in reasonable agreement with the theoretical result calculated in section 3.3. The peak gains were similar, theory predicted a small signal gain of 1200cm^{-1} compared to a measured gain of ~1600cm^{-1}, and both peak gains occurred at a grating spacing of ~1.5μm. The overall characteristics also increased and decayed at similar rates presenting a similar gain trend.

The characteristics of the small signal gain (defined as the maximum gain in the undepleted pump regime) were unusual for an optical amplifier, passing through a maximum as the signal was reduced rather than tending to a constant value. Figure 3.6 shows how the gain varied with signal strength for a grating spacing of 1.36μm. At coarser gratings, the homeotropic gain peak was broadened into a "plateau" but the small signal gain always diminished for signal to pump beam intensity ratios of greater than 1:4000, irrespective of the grating period. This suggests that a threshold voltage is required to change the liquid crystal alignment.

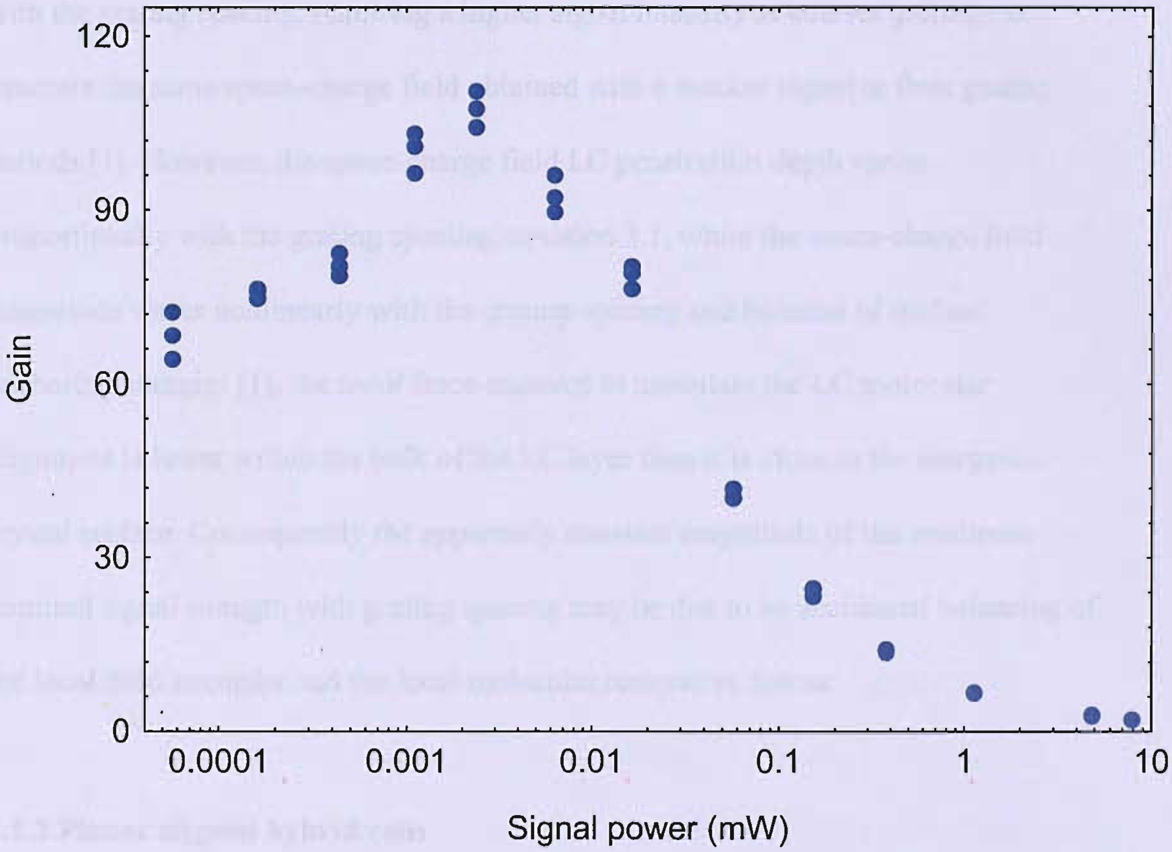

Figure 3.6. Gain versus signal intensity of a HTAB/5CB/Ce:SBN homeotropic hybrid cell

The reduction, rather than saturation, of the gain in the small signal regime for signal to pump ratios > 1:4000 may arise because of a reduction in the Ce:SBN space-charge field at very weak signal levels. If the magnitude of the space-charge field became too weak to significantly affect the local orientation of the LC molecules intra-molecular elastic restoring forces would dominate for very weak signal strengths. However the minimum signal characteristic appeared to be independent of the grating spacing. The minimum signal strength required to maximize the gain was the same for all grating spacings. This suggests that a minimum space-charge field is necessary for reorientation because the local space-charge field strength varies with grating spacing as well as with the beam intensity ratio. The minimum signal strength should scale with the grating spacing, requiring a higher signal intensity at coarser gratings to generate the same space-charge field obtained with a weaker signal at finer grating periods [1]. However, the space-charge field LC penetration depth varies proportionally with the grating spacing, equation 3.1, while the space-charge field magnitude varies nonlinearly with the grating spacing and because of surface anchoring energies [1], the *local* force required to modulate the LC molecular alignment is lower within the bulk of the LC layer than it is close to the inorganic crystal surface. Consequently the apparently constant magnitude of the minimum required signal strength with grating spacing may be due to an accidental balancing of the local field strengths and the local molecular restorative forces.

3.5.2 Planar aligned hybrid cells

Planar aligned cells were made using anti-parallel rubbed PVK with E7. (TL203 did not align successfully with PVK and was not used.) Cells were made with horizontally, vertically and 45° rubbed surfaces (rubbing direction parallel, perpendicular and at 45°, respectively, to the crystal c-axes). Figure 3.7 compares the gain and small signal gain coefficients for the empty and E7 filled hybrid cells respectively for zero applied volts.

The birefringence of the planar aligned LC layer obviated the accurate determination of the gain contribution from the 45° rubbed system. For this case, birefringence from the LC caused the p-polarized light transmitted by the first window to become elliptically polarized. The polarization state of the light subsequently entering the second window could therefore not be accurately determined, especially as the degree of birefringence varied with beam angle. It was also not possible to measure the LC birefringence *in situ* because the second window was itself birefringent, causing a further change in the transmitted beam polarization state. The birefringence was a problem only for the 45° rubbed case - the polarization state remained linear in the p-plane for both the horizontal and vertically rubbed geometries. The LC induced birefringence for the 45° rubbed cell made it impossible to determine the background gain contribution from the windows since the second window gain was reduced by an undetermined amount from the elliptical polarization state of the locally transmitted beams. The 45° rubbed gain coefficient data in figure 3.7 has therefore been presented as two data sets - a minimum gain coefficient calculated by assuming the second window contributed fully to the system gain (i.e. the second window gain was the same as measured for simple p-polarized light), and a maximum gain coefficient calculated by assuming the gain contribution from the second window was *zero*. The gain trend as a function of grating spacing was similar for all rubbing directions. The maximum gain from the E7 (vertically and horizontally rubbed cells) was 7.93, which compares with 5.3 for the homeotropically aligned calls and is equivalent to a gain coefficient of just over 1650 cm^{-1}. Unlike the horizontally and vertically rubbed systems, the 45° rubbed cell did not respond to the 7μm grating period.

Different rubbing directions of the liquid crystal were investigated to present a different asymmetry to the input laser light. The asymmetry enables the refractive index modulation to follow the sign of the local space-charge field and generate an index grating with the same spatial frequency as the optical interference pattern. When the relative direction of the molecular asymmetry is chosen so that the local variations of the liquid crystal and window refractive indices are spatially matched the LC contributes to the refractive index modulation of the window, rather than subtracts.

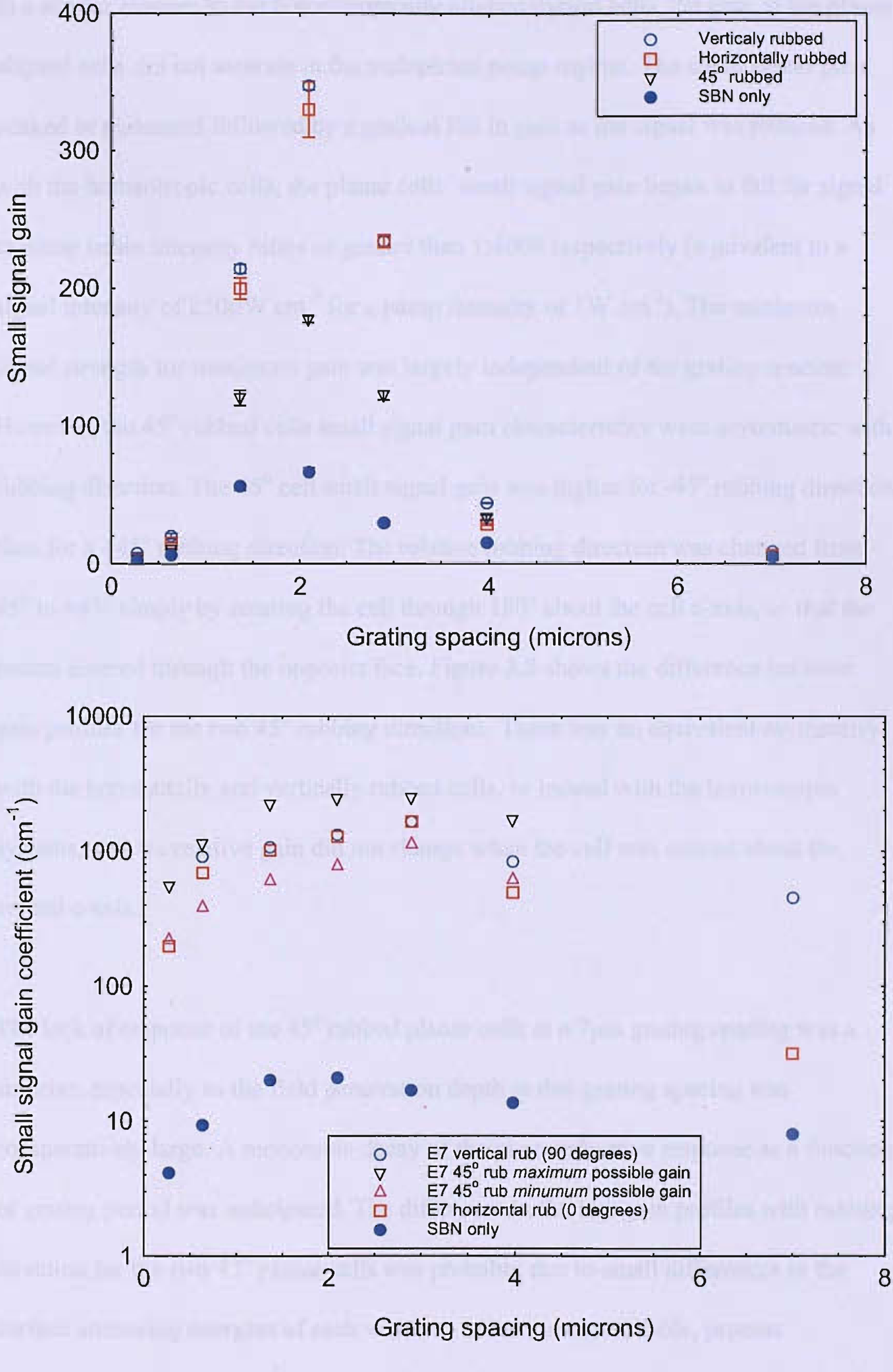

Figure 3.7. Gain (small signal gain and small signal gain coefficient) versus grating spacing for the PVK/E7/Ce:SBN planar hybrid cells at zero volts.

In a similar manner to the homeotropically aligned hybrid cells, the gain of the planar aligned cells did not saturate in the undepleted pump regime. The small signal gain peaked or plateaued followed by a gradual fall in gain as the signal was reduced. As with the homeotropic cells, the planar cells' small signal gain began to fall for signal to pump beam intensity ratios of greater than 1:4000 respectively (equivalent to a signal intensity of 250μW cm^{-2} for a pump intensity of 1W cm^{-2}). The minimum signal strength for maximum gain was largely independent of the grating spacing. However, the 45° rubbed cells small signal gain characteristics were asymmetric with rubbing direction. The 45° cell small signal gain was higher for -45° rubbing direction than for a +45° rubbing direction. The relative rubbing direction was changed from -45° to +45° simply by rotating the cell through 180° about the cell c-axis, so that the beams entered through the opposite face. Figure 3.8 shows the difference between gain profiles for the two 45° rubbing directions. There was no equivalent asymmetry with the horizontally and vertically rubbed cells, or indeed with the homeotropic systems, and the relative gain did not change when the cell was rotated about the crystal c-axis.

The lack of response of the 45° rubbed planar cells at a 7μm grating spacing was a surprise, especially as the field penetration depth at this grating spacing was comparatively large. A monotonic decay of the photorefractive response as a function of grating period was anticipated. The difference in the two gain profiles with rubbing direction for the two 45° planar cells was probably due to small differences in the surface anchoring energies of each window. Minor, uncontrollable, process differences in the spin-coating and rubbing procedures for each window could easily affect the local anchoring energies. The lack of LC birefringence in the vertical and horizontal planar cells allowed a higher net space-charge field in the windows, making these cells less sensitive to minor variations in the surface anchoring energy of each window.

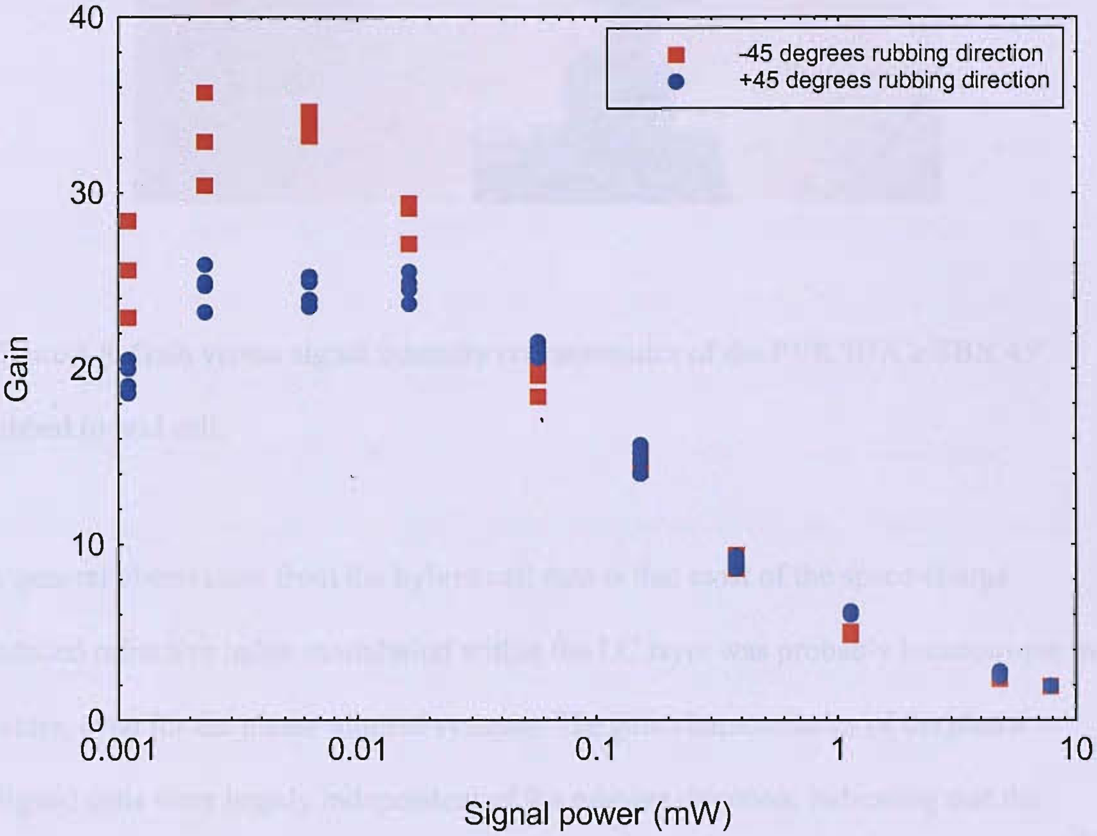

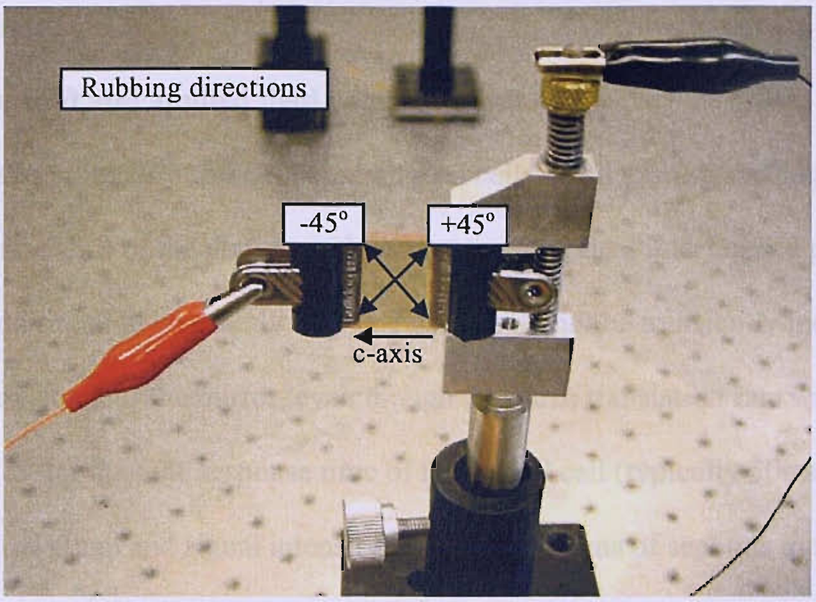

Figure 3.8. Gain versus signal intensity characteristics of the PVK/E7/Ce:SBN 45° rubbed hybrid cell.

A general observation from the hybrid cell data is that most of the space-charge induced refractive index modulation within the LC layer was probably homeotropic in nature, even for the planar aligned systems. The gain characteristics of the planar aligned cells were largely independent of the rubbing direction, indicating that the molecular realignment is unlikely to have been in the plane of the cell windows. In-plane molecular modulation should be zero for horizontal rubbing since the space-charge field would have occurred along the molecular director axis and would not have induced any planar realignment. However, owing to the highly non-uniform field profile away from the inorganic crystal surface, the LC molecules would have experienced torques out of the plane of the cell windows, resulting in a largely homeotropic realignment, irrespective of the initial rubbing direction of the planar cells.

3.6 Discussion

3.6.1. Phase shift and applied field considerations

For both homeotropically and co-planar aligned cells, at all grating spacings (274nm - 7μm) the phase shift of the grating with respect to the optical interference pattern was measured and found to be exactly 90°. The gain could not be transiently increased with any movement of the mirror, even though the piezo translation rate was at least 1,000 times faster than the response time of the hybrid cell (typically 50msec 1/e for 1W cm^{-1} equal pump and signal intensity, and typically tens of seconds in the small signal regime). Any sudden translation of the mirror always decreased the amplified signal power and increased the transmitted pump power in both the small signal regime, and for equal pump and signal. Also at all grating spacings there was no evidence of any Raman-Nath diffraction and the beam coupling appeared to be perfectly Bragg matched for all signal intensities and beam angles. The signal beam was amplified cleanly with no scatter or obvious distortion. Also, both homeotropically and co-planar aligned cells were (unexpectedly) completely unaffected by any applied electric fields, unless the field strength became large enough to disrupt the molecular alignment and cause intracellular scattering. Within experimental errors, the gain, speed of response and the grating phase shift were unaffected by the applied D.C. fields. The alignment disruption at high field strengths confirmed that the field *was* present in the LC layer. At all D.C. field strengths, including zero, there was no sign of a second harmonic grating period for all beam angles.

A surprising observation was that the hybrid cell response was completely unaffected by applied transverse electric fields ranging from 0 to 50Vcm^{-1}, approximately 1/5th of the maximum space charge field (~500Vcm^{-1}) . Theory predicts that the phase shift between the optical interference pattern and the diffraction pattern should change by at least 5^0, a change that should reduce the gain measured by more than 10%. No evidence of higher order grating periods at zero voltage was found, even though under these conditions the LC molecular alignment was nominally symmetric. It is difficult to understand how the beam coupling could remain Bragg matched and unidirectional for symmetrically aligned LC molecules. The implication is that all of the hybrid cells intrinsically had broken symmetries. Given the many alignment schemes and the range of LCs tested, it is difficult to understand how a systematic alignment asymmetry could have occurred. Ce:SBN is not known to generate a significant photovoltaic field which might otherwise have accounted for the apparent molecular asymmetry. If present, a D.C. photovoltaic field would have to have been quite large in order for the applied transverse fields to have little effect. However, the phase shift measurements suggest that there was no significant photovoltaic field as this would have affected the grating phase shift, especially at coarser grating spacings. For the planar rubbed systems the influence of surface molecular tilt as a source of intrinsic alignment asymmetry was considered, although the same argument is difficult to apply to the homeotropic cells. Molecular tilt is a common feature of planar rubbed systems [8,9], even though an obvious surface tilt is not common with PVK rubbed systems, and recently large molecular pre-tilt has been observed on Ce:SBN windows [10]. However, the gain in the hybrid cells was not affected by rotating the hybrid cells about the crystal c-axis, which rules out this possibility. If surface molecular tilt had broken the bulk alignment symmetry, rotation about the crystal c-axis should have reversed the sign of the relative index modulation contribution from the liquid crystal layer. For one propagating direction the LC index modulation would have added to the Ce:SBN index modulation but in the reverse propagation direction the LC index modulation would have *subtracted* from the Ce:SBN index modulation, leading to an asymmetry in the gain profile.

3.6.2. Space charge field considerations

An attempt was made to verify the assumption that the Ce:SBN space-charge field was responsible for the LC alignment modulation by rotating the hybrid cell through 90 degrees so the grating k-vector was orthogonal to the Ce:SBN c-axis but the laser radiation remained p-polarised. This arrangement effectively turns off the electrooptic effect in SBN but the space-charge field remains unaffected. With homeotropically aligned cells, no gain contribution from the LC layer was detected. This observation implies that the space-charge field from the Ce:SBN does not directly influence the LC local molecular alignment as expected and that an electrooptic effect from the window material is required. It is not immediately obvious how an electrooptic response in the cell windows drives the liquid crystal alignment modulation, but the space-charge field may induce a local piezoelectric response in the Ce:SBN which could result in micro-corrugation of the crystal surface which in turn modulates the local alignment of the LC molecules. A piezoelectric response would be sensitive to the local crystal orientation and would account for the lack of gain in the rotated cells. This proposition is investigated in detail in chapter 4.

3.7 Conclusion

The design of hybrid photorefractive systems comprising a nematic liquid crystal layer adjacent to inorganic photorefractive windows has been described. With this arrangement, the underlying photorefractive characteristics are determined by the inorganic window while the total photorefractive gain is significantly enhanced by the LC layer. Using this technique Bragg matched gain coefficients of more than 1600 cm^{-1}, grating periods >300nm, and wide beam intersection angles with perfect 90° phase shifts between the optical and refractive index gratings at normal incidence (without the need for an external field) were obtained. The enhancement was predicted in section 3.2 however the detailed experimentally measured response does not agree with our current theory. The results imply that the local LC refractive index modulation is asymmetric and depends on the existence of a local electrooptic response in the cell windows. This is presently unexplained but may indicate that the LC modulation is driven by space-charge induced piezoelectric surface deformations of the photorefractive crystal windows. This proposition is studied in the next chapter.

3.8 References

[1] G. Cook, C Wyres, M Deer, D Jones, *Hybrid organic-inorganic photorefractives*, SPIE, **5213** (2003).

[2] E. Hecht and A. Zajac, *Optics*, Addison-Wesley Publishing Co. (1979).

[3] I. C. Khoo, *Liquid Crystals*, John Wiley & Sons Inc. (1995).

[4] F. Simoni, *Nonlinear Optical Properties of Liquid Crystals and Polymer Dispersed Liquid Crystals*, Series on Liquid Crystals, Volume 2, World Scientific Publishing Co. Ltd. (1997).

[5] DC Jones, G Cook, *Theory of beam coupling in a hybrid photorefractive-liquid crystal cell*, Optics Communications, **232,** 399-409 (2004).

[6] F. Kajzar, S Bartkiewicz, A. Miniewicz, *Optical amplification with high gain in hybrid polymer liquid crystal structures*, Applied Physics Letters, **74(20)**, 2926-2926 (1999).

[7] Krammer M, Baade T and Kowarschik R, *Etalon effects in wave-mixing experiments with photorefractive crystals*, Applied Physics, **B67**, 583-586 (1998).

[8] Laeri F, Tschudi T, Aibers J, *Coherent cw image amplifier and oscillator using two-wave interaction in a BTO crystal*, Optics Communications, **47(6)**, 387-390 (1983).

[9] Tschudi T, Herden A, Goltz J, Klumb H, Laeri F, *Image amplification by two- and four-wave mixing in BTO photorefractive crystals*, IEEE Journal of Quantum Electronics, 22(8), 1493-1502 (1986).

[10] Sutherland RL, Cook G, and Evans D, *Determination of large nematic pre-tilt in liquid crystal cells with mechanically rubbed photorefractive Ce:SBN windows*, Optics express, 14(12), 5365-5375 (2006).

Appendix 3.1

```
paras:=(
  d=12.5 10^-6;
  l=3 10^-3;
  no=1.5211;
  ne=1.7464;
  de=13.8 8.85 10^-12;
  Ke=(6.4+10)/2  10^-12;
  alpha=1Pi/180;
  betaair=0;
  Vlc=-9;
  Vpr=500;
  lambda=532. 10^-9;)
\!\(\(\(calc := \((\[IndentingNewLine]beta =
    bint /. FindRoot[
      bint \[Equal]
        ArcSin[\[IndentingNewLine]\(betaair/
              Sqrt[no^2\ Sin[bint]^2 + ne^2\ \ Cos[bint]^2]\)/
            no\ ne], {bint, Pi/8}]; \[IndentingNewLine]n =
    no\ ne/Sqrt[
        no^2\ Sin[beta]^2 + ne^2\ Cos[beta]^2]; \[IndentingNewLine]k =
    2  Pi\ n/\((532\ 10^\(-9\))\); \[IndentingNewLine]K =
    2\ 2\ Pi/lambda\ Sin[alpha]; \[IndentingNewLine]Lambdamic =
    2\ Pi/K\ 10^6; \[IndentingNewLine]Ed =
    K\ \ 1.38\ 10^\(-23\)\ 300/\((1.6\ 10^\(-19\))\); \
```

```
\[IndentingNewLine]E0x = Vlc/d; \[IndentingNewLine]E0 =
     Vpr/l\ Sin[beta]; \[IndentingNewLine]Ew =
     E0 + I\ Ed; \[IndentingNewLine]der = \(-no^2\)
      ne^2 \((ne^2 -
           no^2)\)/\((\((no^2 + ne^2)\)/2 + \((ne^2 - no^2)\)/2
             Cos[2  beta])\); \[IndentingNewLine]t1 =
     de\ E0x\ Ew/\((2  K^2  Ke\ Exp[1])\); \[IndentingNewLine]Phi =
     K\ \ Sin[beta]; \[IndentingNewLine]gammad1 = \(-I\)\ k\ der\ Sin[
        2  beta]
      t1/\((4\ n^2
            Cos[beta])\)\[IndentingNewLine]\((\(\[ExponentialE]\^\(1 - \
\[ImaginaryI]\ d\ Phi\)\)
           K \((\(\[ExponentialE]\^\(4
                      d\ K + \[ImaginaryI]\ d\ Phi\)\) \((K - \
\[ImaginaryI]\ Phi)\)\^2 + \(\[ExponentialE]\^\(\[ImaginaryI]\ d\ Phi\)\) \((\
\(-\[ImaginaryI]\)\ K + Phi)\)\^2 - \[IndentingNewLine]2 \( \[ExponentialE]\^\
\(3  d\ K\)\) \((K\^2 + d\ K\^3 - Phi\^2 + d\ K\ Phi\^2)\) -
                 2 \( \[ExponentialE]\^\(d\ K\)\) \((\(-K\^2\) + d\ K\^3 +
                    Phi\^2 +
                    d\ K\ Phi\^2)\) + \[IndentingNewLine]4 \( \
\[ExponentialE]\^\(2  d\ K + \[ImaginaryI]\ d\ Phi\)\)
                 K \((\[ImaginaryI]\ Phi +
                    d \((K\^2 +
                         Phi\^2)\))\))\))\)/\((\(\((\(-1\) + \
\[ExponentialE]\^\(2  d\ K\))\)\^2\) \(\((K - \[ImaginaryI]\ Phi)\)\^2\) \((K \
+ \[ImaginaryI]\ Phi)\)\^2)\); \[IndentingNewLine]gammad2 = \(-I\)\ k\ der\ \
Sin[2  beta]
      t1/\((4\ n^2
            Cos[beta])\)\[IndentingNewLine]Conjugate[\((\(\[ExponentialE]\
\^\(1 - \[ImaginaryI]\ d\ Phi\)\)
            K \((\(\[ExponentialE]\^\(4
                       d\ K + \[ImaginaryI]\ d\ Phi\)\) \((K - \
\[ImaginaryI]\ Phi)\)\^2 + \(\[ExponentialE]\^\(\[ImaginaryI]\ d\ Phi\)\) \((\
\(-\[ImaginaryI]\)\ K + Phi)\)\^2 - \[IndentingNewLine]2 \( \[ExponentialE]\^\
\(3  d\ K\)\) \((K\^2 + d\ K\^3 - Phi\^2 + d\ K\ Phi\^2)\) -
                  2 \( \[ExponentialE]\^\(d\ K\)\) \((\(-K\^2\) +
                     d\ K\^3 + Phi\^2 +
                     d\ K\ Phi\^2)\) + \[IndentingNewLine]4 \( \
\[ExponentialE]\^\(2  d\ K + \[ImaginaryI]\ d\ Phi\)\)
                  K \((\[ImaginaryI]\ Phi +
                     d \((K\^2 +
                          Phi\^2)\))\))\))\)/\((\(\((\(-1\) + \
\[ExponentialE]\^\(2  d\ K\))\)\^2\) \(\((K - \[ImaginaryI]\ Phi)\)\^2\) \((K \
+ \[ImaginaryI]\ Phi)\)\^2)\)]; \[IndentingNewLine]{Log[\((Abs[\((1 +
                  gammad1)\)/\((1 -
                  gammad2)\)]^2)\)]/\((100\ d)\), \
\[IndentingNewLine]Log[\((Abs[\((1 +
                 gammad1)\)]^2)\)]/\((100\ d)\), \[IndentingNewLine]Log[\
\((Abs[1/\((1 + gammad2)\)]^2)\)]/\((100\ d)\)})\)\)\(\[IndentingNewLine]\)
  \)\)
```

Chapter 4 - Off axis gain considerations in a hybrid photorefractive

At the end of chapter 3 the assumptions about the mechanism response for the enhanced performance of inorganic-organic photorefractives hybrid devices was challenged. In this chapter, other possible mechanisms are investigated using a combination of piezoelectric theory, electro-optic theory, atomic force microscopy (AFM), and optical experiments. The underlying physics for this effect is isolated to the inorganic window rather than the liquid crystal layer. This is an important result since these hybrid devices cannot be optimised without a thorough grasp of the underlying physics.

4.1 Background

In the previous chapter (chapter 3), it was assumed that the penetration of space charge field developed in the Ce:SBN window into the liquid crystal layer was directly responsible for molecular reorientation and therefore the refractive index modulation in the liquid crystal layer. To verify this assumption the hybrid cell has been rotated through 90 degrees so that the grating k-vector is orthogonal to the Ce:SBN c-axis. This configuration reduces the refractive index modulation in SBN to zero, since the electro-optic coefficient equals zero ($r_{eff}=0$) but the diffusion field should remain the same. Therefore the response of the liquid crystal layer should remain. However no gain contribution from the LC layer was detected, even though a range of grating spacings have been tested, as shown in figure 4.1. Other effects, discussed in chapter 3, such as minimum dependence on liquid crystal alignment and the 90^0 phase shift in spite of perfect symmetry.

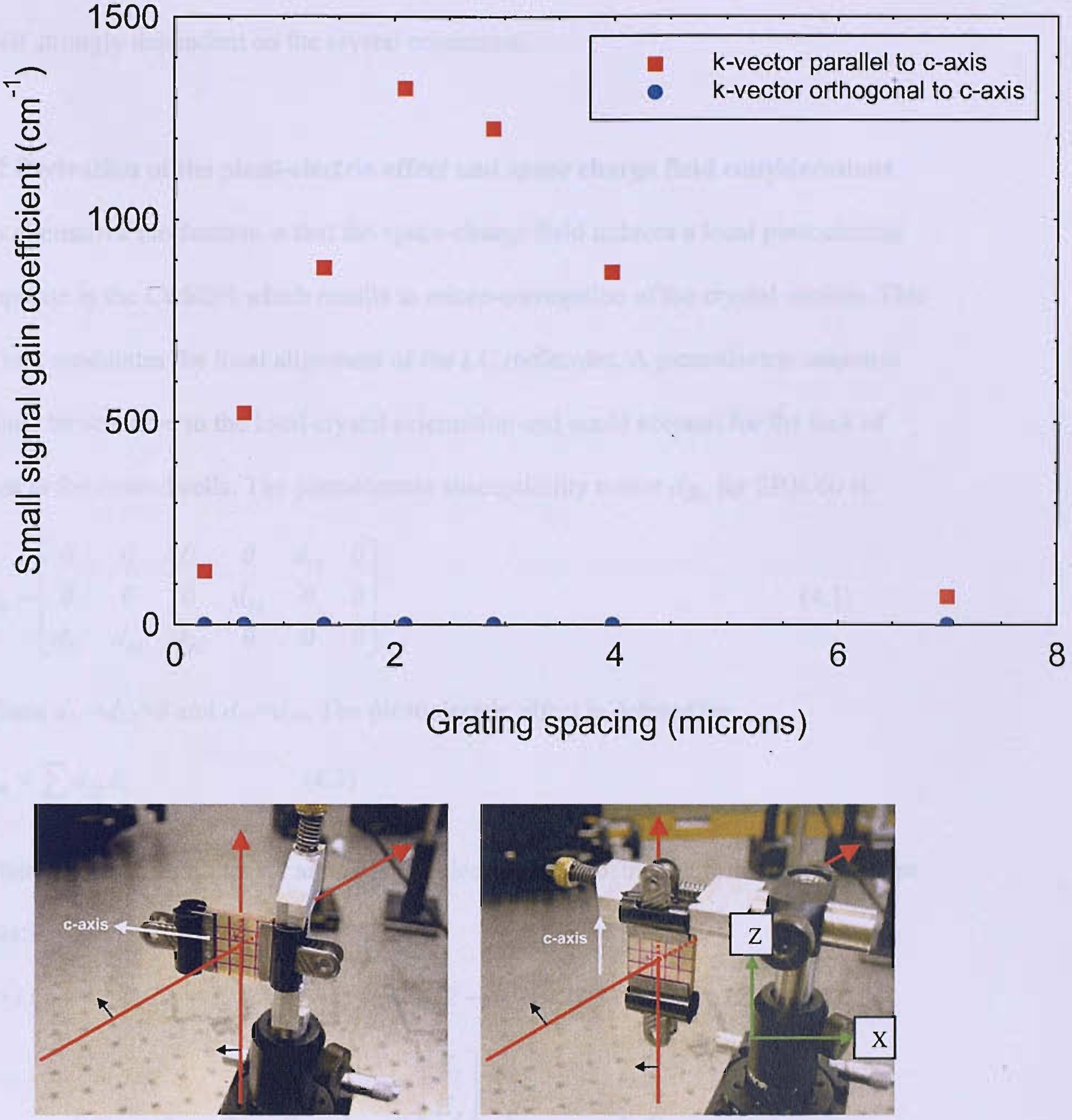

Figure 4.1. Small signal gain as a function of grating spacing (top) for the hybrid device with the grating vector parallel (bottom left) and perpendicular to the crystal c-axis (bottom right).

These observations suggest that the space-charge field from the Ce:SBN does not directly influence the LC molecular alignment or perhaps the space charge field is itself strongly dependent on the crystal orientation.

4.2 Derivation of the piezo-electric effect and space charge field considerations

An alternative mechanism is that the space-charge field induces a local piezoelectric response in the Ce:SBN which results in micro-corrugation of the crystal surface. This in turn modulates the local alignment of the LC molecules. A piezoelectric response would be sensitive to the local crystal orientation and could account for the lack of gain in the rotated cells. The piezoelectric susceptibility tensor d_{ijk}, for SBN 60 is

$$d_{ijk} = \begin{bmatrix} 0 & 0 & 0 & 0 & d_{15} & 0 \\ 0 & 0 & 0 & d_{24} & 0 & 0 \\ d_{31} & d_{32} & d_{33} & 0 & 0 & 0 \end{bmatrix} \qquad (4.1)$$

Where $d_{31}=d_{32}=0$ and $d_{15}=d_{24}$. The piezoelectric effect is defined by

$$S_{jk} = \sum_{jk} d_{ijk} E_i \qquad (4.2)$$

Where S_{jk} is the strain tensor and E_i is the electric field. Using the following subscript notation

$jk=11 \rightarrow 1, jk=22 \rightarrow 2, jk=33 \rightarrow 3, jk=23,32 \rightarrow 4, jk=31,13 \rightarrow 5, jk=12,21 \rightarrow 6$

$$S_{jk} = \sum_{jk} \begin{bmatrix} 0 & 0 & 0 & 0 & d_{15} & 0 \\ 0 & 0 & 0 & d_{24} & 0 & 0 \\ d_{31} & d_{32} & d_{33} & 0 & 0 & 0 \end{bmatrix} \begin{bmatrix} E_1 \\ E_2 \\ E_3 \\ E_4 \\ E_5 \\ E_6 \end{bmatrix} = \begin{bmatrix} d_{15}E_5 \\ d_{24}E_4 \\ d_{31}E_1 + d_{32}E_2 + d_{33}E_3 \end{bmatrix} \qquad (4.3)$$

S_{11}, S_{22}, S_{33} are parallel to x, y, and z respectively. S_{12} is rotation about z of a line element parallel to y. Thus

$$\begin{bmatrix} \Delta x \\ \Delta y \\ \Delta z \end{bmatrix} = \begin{bmatrix} d_{15}E_5 \\ d_{24}E_4 \\ d_{31}E_1 + d_{32}E_2 + d_{33}E_3 \end{bmatrix} \begin{bmatrix} x \\ y \\ z \end{bmatrix} \qquad (4.4)$$

$$\Delta x = d_{15}E_5 x = 0$$

$$\Delta y = d_{24}E_4 y = 0 \qquad (4.5)$$

$$\Delta z = [d_{31}E_1 + d_{32}E_2 + d_{33}E_3]z = d_{33}E_3 z$$

Equation (4.5) implies that a field applied along the crystal c-axis (E_3) would cause extension along the z-axis (see figure 4.1- bottom right- the c-axis is parallel to the z-axis). The piezoelectric coefficients for Ce:SBN are d_{33}=130pm/V and d_{13}=40pm/V which are larger than the same coefficients for Fe:LiNbO$_3$ (d_{31}=d_{15}=5.95 pm/V). Surface corrugations of ~6.5nm in height have been measured [1] in Fe:LiNbO$_3$.

Since Ce:SBN is diffusion dominated, after the optical intensity fringes are created via two beam coupling, the same photoexcitation occurs when the crystal is rotated so that the grating k-vector is at 90^0 with respect to the crystal c-axis. As long as there is a finite diffusion coefficient in this direction, then a space charge field should still develop. If the above theoretical corrugation is present then it will be proportional to this space charge field. Any corrugation should therefore share the same periodicity as that of the optical interference pattern.

4.3 Investigating possible piezo-electric induced surface corrugation

Surface gratings associated with holographic volume gratings in photorefractive crystals of iron-doped lithium niobate have been observed. These have been studied using diffraction of a reflected probe beam and high-resolution phase shifted interferometric profilometry [1]. Both techniques reported that the surface gratings exist in the form of periodical corrugations of the same period as that of the volume grating. The maximum amplitude of the periodical surface relief measured was ~6.5nm. This measurement was made possible by the holographic recording of a volume grating inside the lithium niobate crystal using two linearly polarised beams in a transmission two-beam coupling geometry [1]. The beam intersection angle was chosen to give a grating period of ~13.4μm [1]. The reflection from the faces of the crystal was analysed with a weak randomly polarised probe beam in two ways. Firstly the rear face of the photorefractive crystal, with respect to the writing beams, was coated with an optically absorbing black paint and the probe beam was incident on and reflected from the front face. Secondly, the rear face was coated with a cold-sputtered removable 30nm thick film of gold on which the probe beam was reflected. The surface of the crystal was also inspected with an optic profiler in phase-shifting interferometry mode. The image of the surface contained periodical corrugations. Unfortunately, due to the very short grating lifetime in Ce:SBN compared to the grating lifetimes in Fe:$LiNbO_3$, these techniques cannot be used here. Any probing of the Ce:SBN crystal surface has to be carried out simultaneously with the two-beam writing.

Attempts have been made to overcome the short lifetime in Ce:SBN. Fixed charge gratings have been directly observed with a scanning electron microscope [2]. However the images obtained had a low signal to noise ratio owing to the difficulty of imaging non-conductive surfaces. Therefore no information on the microscopic charge structure was obtained from these experiments. Other attempts have used microphotometric imaging techniques [3] or self-imaging at finite conjugates [4], but none of these methods has given highly resolved images of the microscopic properties.

Ce:SBN has been studied using an atomic force microscope (AFM) [1] to overcome the above issues due to its ability of simultaneously detecting a large variety of surface properties with lateral resolution in the nm-range. The lateral resolution is limited by the tip radius, typically of the order of a few nano-meters.

In collaboration with Drs D Smith & J Gates at Southampton University, the experimental technique reported in reference [1] has been reproduced and used to measure the topography during two-beam coupling process taking place along both the c-axis and also perpendicular to the c-axis in Ce:SBN. Such thorough investigation of different experimental geometries has not been investigated before. Attempts were also made to measure the space charge field in both directions.

4.3.1 Measuring the surface charge distribution and topography of Ce:SBN

In atomic force microscopy a fine tip is attached to the end of a cantilever that is placed near the surface of the sample using a piezoscanner. The electrostatic force between tip and sample is detected by measurement of the bending of the cantilever. An image of the sample surface is obtained by scanning the tip over the sample while keeping the interaction force constant by means of a feedback circuit. In this way the topography can be mapped without touching the surface.

In electrostatic force microscopy (EFM) charges on the surface of an insulating material are detected by measuring the electrostatic force between the surface charge and a probe charge which is periodically supplied onto the conducting tip by applying a sinusoidal voltage between tip and a back electrode [5]. The use of lock-in detection for the force measurement allows the polarity of the surface charge to be determined.

The experimental set up used to measure both the topography and charge distribution is shown below in figure 4.2.

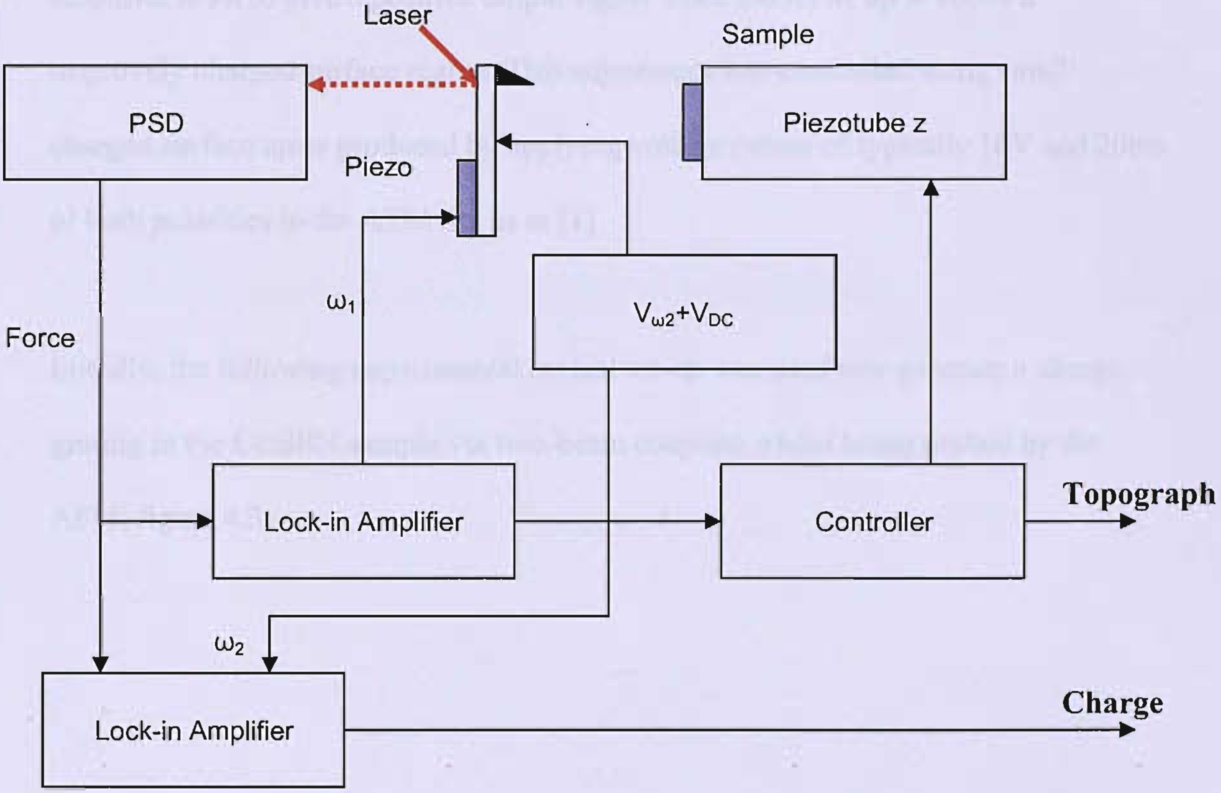

Figure 4.2. Experimental AFM set-up for measuring the topography and charge distribution.

The bending of the cantilever is measured using a laser beam that is reflected from the back of the cantilever onto a position sensitive photodetector (PSD), the topography can be deduced from this measurement. For charge detection, the AFM is used in non-contact mode where the cantilever is excited at its resonant frequency (ω_1~60 kHz) by a piezoelectric transducer. The oscillation amplitude, which is proportional to the force gradient in the vicinity of the surface, is measured with a lock-in amplifier. A feedback circuit keeps the oscillation amplitude constant. Typical tip-sample distances used are <10nm [1]. The sinusoidal voltage applied to the tip for charge detection has an amplitude of 2.5V and a frequency of ω_2=2 kHz. The electrostatic force signal is measured with a second lock-in amplifier at frequency ω_2. The phase of this lock-in amplifier is set to give a positive output signal when the AFM tip is above a negatively charged surface region. This adjustment was controlled using small charged surface areas produced by applying voltage pulses of typically 10V and 20ms of both polarities to the AFM tip, as in [1].

Initially, the following experimental optical set-up was used two generate a charge grating in the Ce:SBN sample via two-beam coupling whilst being probed by the AFM, figure 4.3.

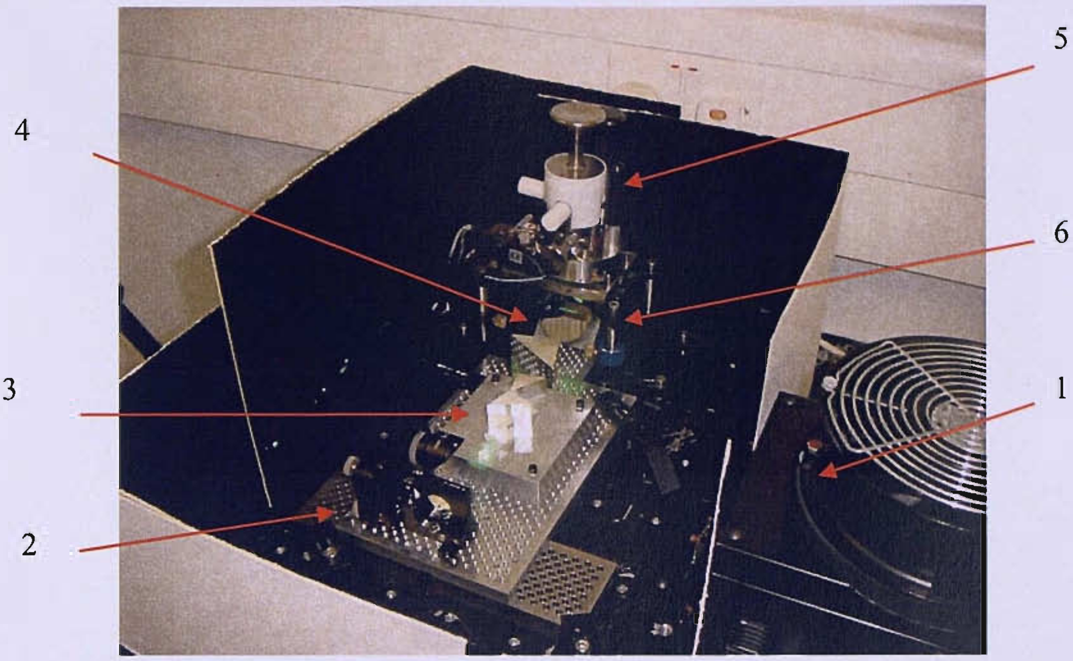

Figure 4.3. The initial experimental set-up used to measure the charge distribution and topography during two beam coupling in Ce:SBN.

The labels in figure 4.3 correspond to the following components: (1) Argon Ion laser (λ~514nm). (2) Periscope. (3) Anamorphic beam expansion [6] to minimise the use of space compared to using a cylindrical lens. (4) A prism used to split the beam, see figure 4.4. (5) AFM. (6) AFM positioning holder.

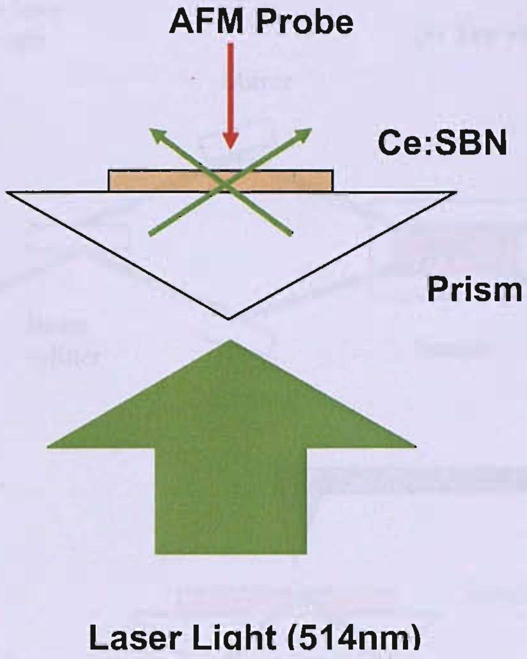

Figure 4.4. A schematic diagram of the resulting two beam coupling arrangement using a prism to split the incident laser light and mount the Ce:SBN window onto.

Initially the signal to noise ratio was rather poor. Noise levels in the topography scans were ~100nm, which greatly exceeds the expected modulation depth (~1-10nm). The problem was subsequently isolated to vibrations from the cooling fans in the Argon ion laser. In addition, a significant amount of unwanted 514nm-laser light was incident on the atomic force microscope's position sensitive photodetector during the two-beam coupling. A new low scattering optical arrangement was required. The experimental set-up was modified at this stage. To avoid mechanical noise from the laser, a separate optical table was used for the AFM and the laser light was delivered through a single mode optical fibre (Thor labs 460 HP). The crystal was illuminated in a total internal reflection geometry to significantly reduce unwanted laser light reaching the photodiode. The modified experimental set-up is shown in figure 4.5.

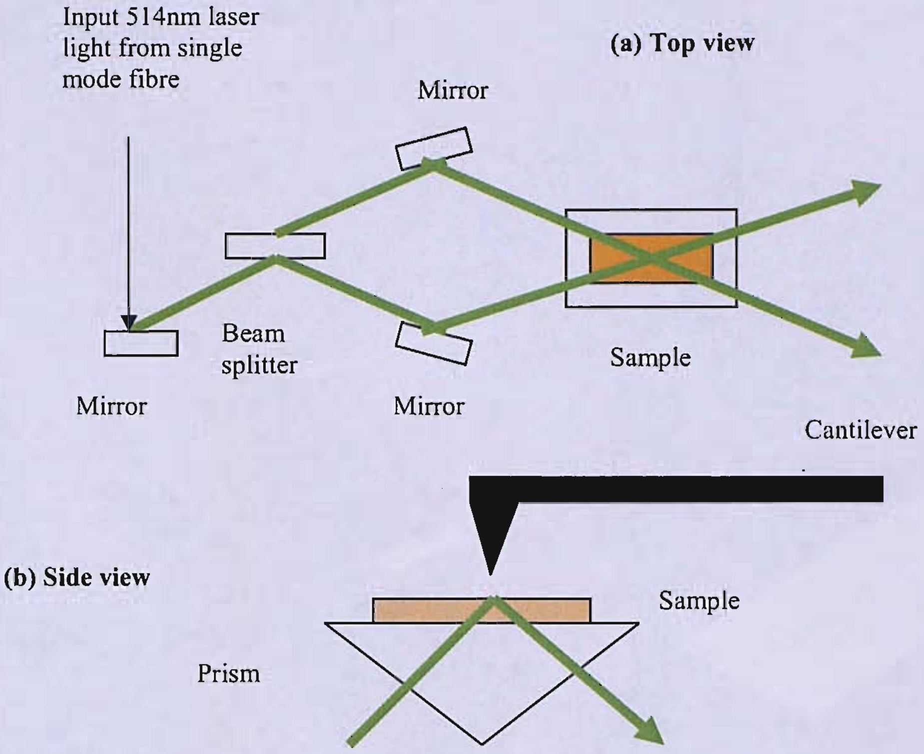

Figure 4.5. (a) Optical set-up for generation of piezoelectrically induced corrugation in Ce:SBN. (b) Enlarged view of the total internal reflection geometry [1].

The angle of intersection between the two beams could be varied to give grating periods between 1.5μm and ~3μm. The polarisation direction was parallel to the plane of incidence. The incident intensity was adjusted to ~1Wcm^{-2}. Using this set-up noise levels were reduced from ~100nm to ~1nm. A photograph of the experimental set-up is shown in figure 4.6.

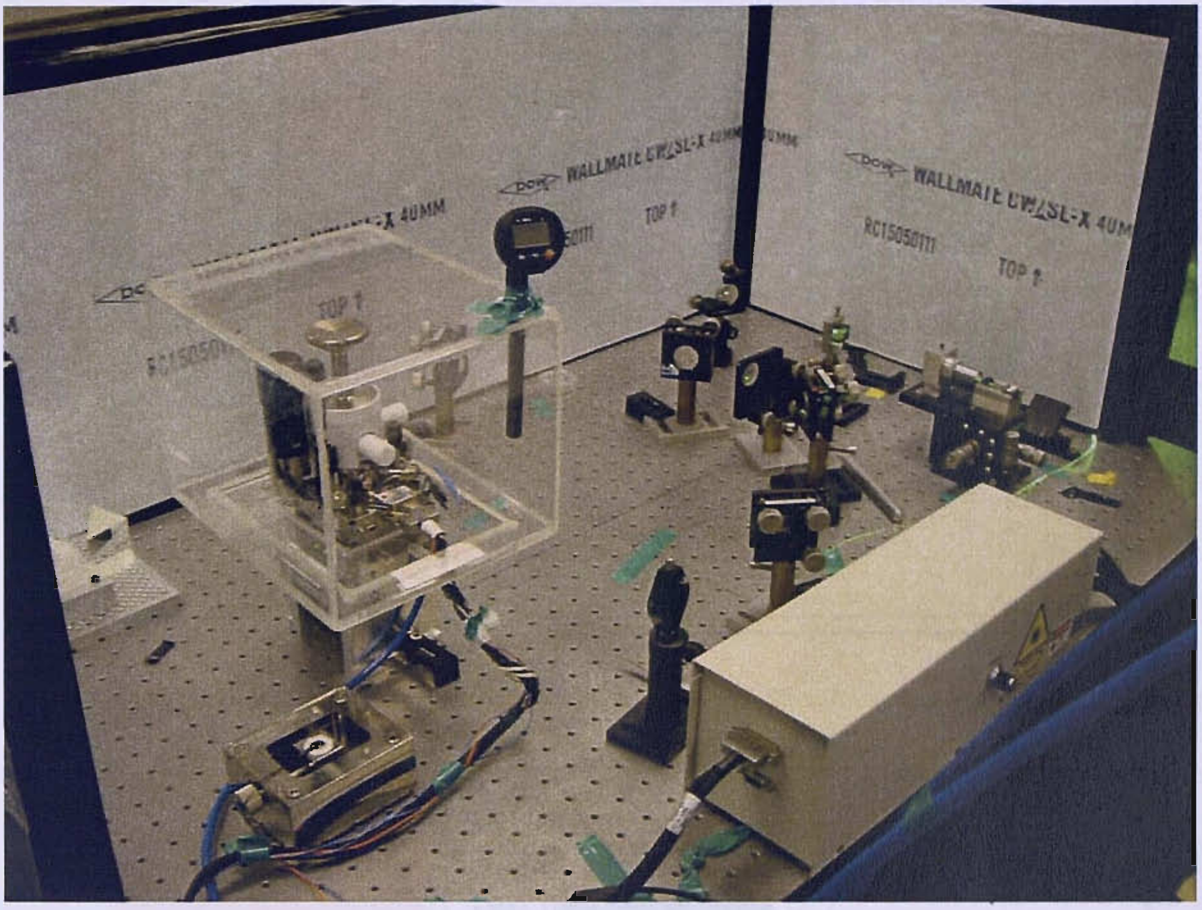

Figure 4.6. A photograph of the experimental set-up used to measure piezoelectrically induced corrugation.

4.3.2 Results

Figure 4.7(a) shows the topography scan taken during two-beam coupling at an optimum grating spacing of 2μm for maximum gain. The beams have equal intensity for maximum modulation. The grating k-vector is perpendicular to the crystal c-axis. Figure 4.7(b) is the corresponding spatial frequency component spectrum.

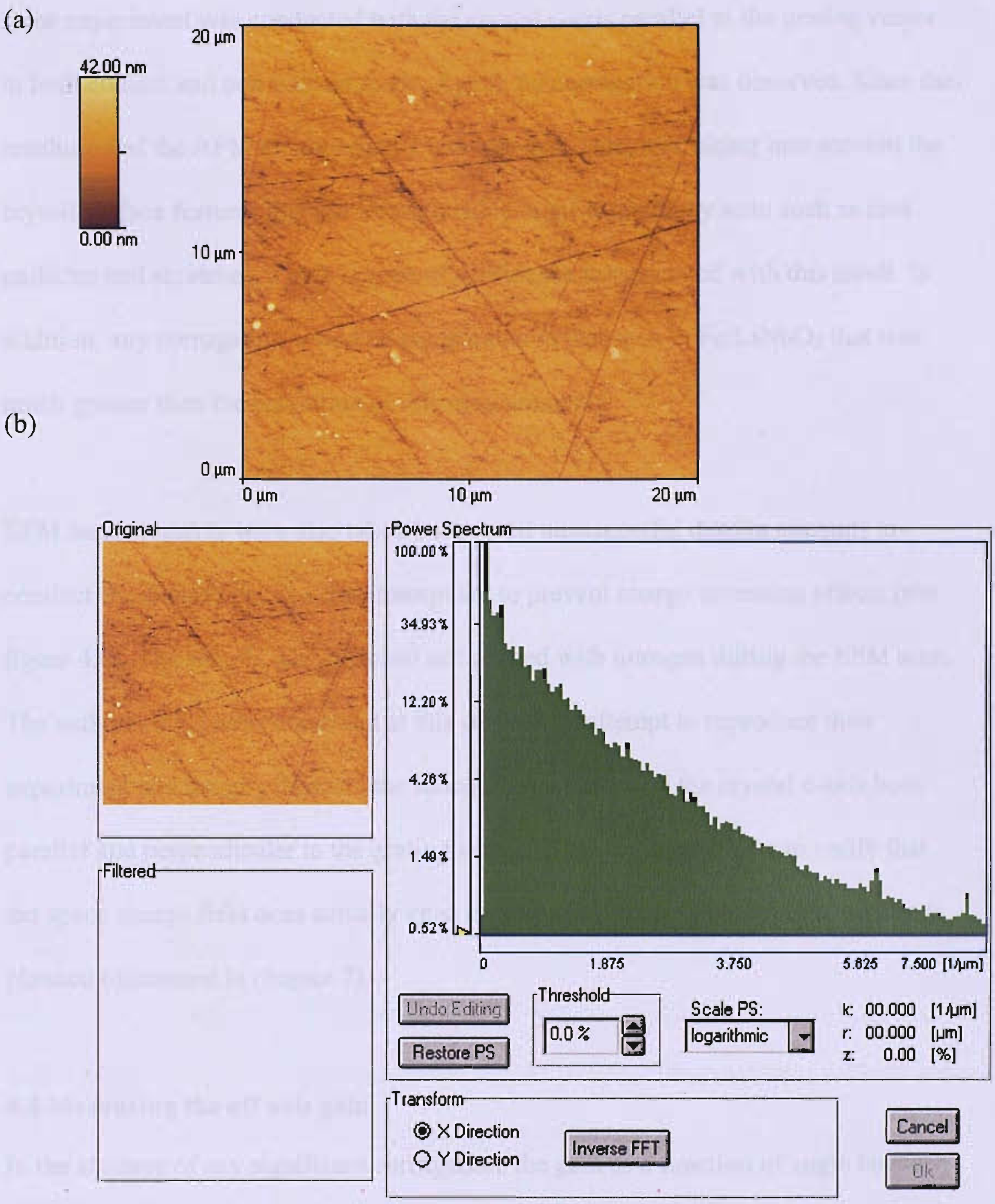

Threshold: 0.0 %

Scale PS: logarithmic

k: 00.000 [1/µm]
r: 00.000 [µm]
z: 0.00 [%]

Transform
● X Direction
○ Y Direction

Figure 4.7. (a) The topography scan taken during two-beam coupling at an optimum grating spacing of 2µm. (b) Corresponding frequency spectrum.

The absence of corrugation in the topography scan and any prominent frequency component in the corresponding frequency spectrum show that the amplitude of the corrugation is <1nm. The resolution was dictated by the signal to noise ratio. The same experiment was conducted with the crystal c-axis parallel to the grating vector in both contact and non-contact mode. Again, no corrugation was observed. Since the resolution of the AFM measurements was less than 1nm, and taking into account the crystal surface features that are clearly visible in the topography scan such as dust particles and scratches, a high degree of confidence is associated with this result. In addition, any corrugation would be comparable to that seen in Fe:LiNbO$_3$ that was much greater than the resolution of this measurement.

EFM measurements were also taken but proved unsuccessful despite attempts to conduct the experiment in a dry atmosphere to prevent charge screening effects (see figure 4.6). The sample was enclosed and purged with nitrogen during the EFM scan. The authors of [1] were contacted at this stage in an attempt to reproduce their experiment and thereby measure the space charge field with the crystal c-axis both parallel and perpendicular to the grating vector. This would enable us to verify that the space charge field does actually exist is both orientations. Future collaboration is planned (discussed in chapter 7).

4.4 Measuring the off axis gain

In the absence of any significant corrugation, the gain as a function of angle between the grating k-vector and the crystal c-axis was measured to obtain a greater insight into the absence of gain at 90^0 in the hybrid cell.

4.4.1 Theory off axis EO effect in Ce:SBN

To predict the expected two beam coupling gain in a Ce:SBN window the effective electro-optic coefficient must be calculated as a function of angle. The effective electro-optic coefficient *r* for Ce:SBN can be written [7]

$$r = \frac{1}{\varepsilon^2} . \underline{\hat{e}_1} . \underline{\underline{\varepsilon}} . \underline{\underline{\underline{r}}} . \underline{\hat{K}} . \underline{\underline{\varepsilon}} . \underline{\hat{e}_2} \tag{4.6}$$

Where

$$\begin{aligned} \underline{E_1} &= E_1 \underline{\hat{e}_1} \\ \underline{E_2} &= E_2 \underline{\hat{e}_2} \\ \underline{E_{sc}} &= E_{sc} \underline{\hat{K}} \end{aligned} \tag{4.7}$$

Where $\underline{\hat{e}_1}, \hat{e}_2$ are unit vectors along the polarisation directions. $\underline{\hat{K}}$ is a unit vector along the grating vector. The effective electro-optic coefficient thus depends on the direction of the K vector, the direction of the polarisation vectors, the electro-optic tensor coefficients and the permittivity tensor components.

$$\varepsilon_1 = \underline{\hat{e}_1} \left(\underline{\underline{\varepsilon}} - \underline{\underline{\varepsilon}}\, \underline{\underline{\underline{r}}}\, \underline{E_0}\, \underline{\underline{\varepsilon}} \right) \underline{\hat{e}_1}, \quad \varepsilon_2 = \underline{\hat{e}_2} \left(\underline{\underline{\varepsilon}} - \underline{\underline{\varepsilon}}\, \underline{\underline{\underline{r}}}\, \underline{E_0}\, \underline{\underline{\varepsilon}} \right) \underline{\hat{e}_2} \tag{4.8}$$

Unfortunately, because the dielectric permittivity is a tensor quantity and not a vector quantity (4.9), in the case of Ce:SBN, the effective electro-optic coefficient is undefined for all angles using equation (4.6), unless dramatic simplifying assumptions are made. However, when the c-axis is parallel to the grating vector it is possible to deduce the effective electro-optic co-efficient (equation 2.32 in chapter 2) and also when the grating vector is orthogonal to the c-axis which is outlined below. Due to the uniaxial symmetry of Ce:SBN the effective electro-optic co-efficients at 180^0 and 360^0 are also known. For uniaxial crystals the dielectric permittivity is

$$\underline{\underline{\varepsilon}} = \varepsilon_0 \begin{pmatrix} \varepsilon_{11} & 0 & 0 \\ 0 & \varepsilon_{22} & 0 \\ 0 & 0 & \varepsilon_{33} \end{pmatrix} \tag{4.9}$$

For SBN $r_{13}=r_{23}=r_{33}$, $r_{42}=r_{51}$ the remaining co-efficients are zero. Using equation (4.13), and inverting, the permittivity when the electric field is in the direction of the c axis (parallel to z) is

$$\underline{\underline{\varepsilon}} = \varepsilon_0 \begin{pmatrix} \varepsilon_{11} + \varepsilon_{11}^2 r_{13} E_z & 0 & 0 \\ 0 & \varepsilon_{22} + \varepsilon_{11}^2 r_{23} E_z & 0 \\ 0 & 0 & \varepsilon_{33} + \varepsilon_{33}^2 r_{33} E_z \end{pmatrix} \tag{4.10}$$

in agreement with [7]. However, when the crystal is rotated 90^0 the electric field vector becomes $(E_1,E_2,0)$, consequently $\Delta\varepsilon$ is not diagonal in form i.e. the old and new principle axes do not coincide. After a principle axis transformation ε becomes [7]

$$\underline{\underline{\varepsilon}} = \varepsilon_0 \begin{pmatrix} \varepsilon_{11} + \varepsilon_{11}^2 r_{13} E_z & 0 & 0 \\ 0 & \varepsilon_{22} + \varepsilon_{11}^2 r_{23} E_z & -\varepsilon_{22}\varepsilon_{11} r_{42} E_y \\ 0 & -\varepsilon_{22}\varepsilon_{11} r_{42} E_y & \varepsilon_{33} + \varepsilon_{33}^2 r_{33} E_z \end{pmatrix} \tag{4.11}$$

Let waves 1 and 2 in the two beam-coupling configuration be incident at angles α and β with respect to the c-axis, with polarisation vectors $\underline{e_1}$ and $\underline{e_2}$. The aim now is to turn the vector differential equation into a scalar one by multiplying the $\underline{\underline{\Delta\varepsilon}}$ tensor by $\underline{e_1}$ from the left and by $\underline{e_2}$ from the right, which serves to replace the two field vectors by their amplitudes [7] and inserting $E_z=0$

$$e_1 \cdot \underline{\underline{\Delta\varepsilon}} \cdot \underline{e_2} = \begin{pmatrix} -\cos\alpha \\ \sin\alpha \end{pmatrix} \begin{pmatrix} -\varepsilon_{22}^2 r_{23} E_z & \varepsilon_{22}\varepsilon_{33} r_{42} E_y \\ -\varepsilon_{22}\varepsilon_{33} r_{42} E_y & -\varepsilon_{22}^2 r_{23} E_z \end{pmatrix} \begin{pmatrix} -\cos\beta \\ \sin\beta \end{pmatrix}$$

(4.12) [7]

$$= \varepsilon_{22}\varepsilon_{11} r_{42} E_y (\sin\alpha\cos\beta - \cos\alpha\sin\beta)$$

Therefore when the grating vector is at 90^0 to the c-axis $\underline{\underline{\Delta\varepsilon}} = 0$ therefore from equation 5.7, the effective electro-optic co-efficient is zero since there is a finite space charge field. No diffraction grating is present and hence the gain is zero. By definition [7]:

$$\Delta\frac{1}{\underline{\underline{\varepsilon}}} = \underline{\underline{r}}E_{sc} \tag{4.13}$$

4.4.2 Experiment

The Ce:SBN hybrid cell, with and without a liquid crystal layer, was mounted onto a computer controlled rotation stage to measure the off axis gain as function of angle with respect to the crystal c-axis (figure 4.8). The beam intersection angle was chosen to give an optimum grating spacing of ~2μm and 532nm wavelength laser light was used but without relay imaging onto the front of the cell for ease. The intensity profile was Gaussian.

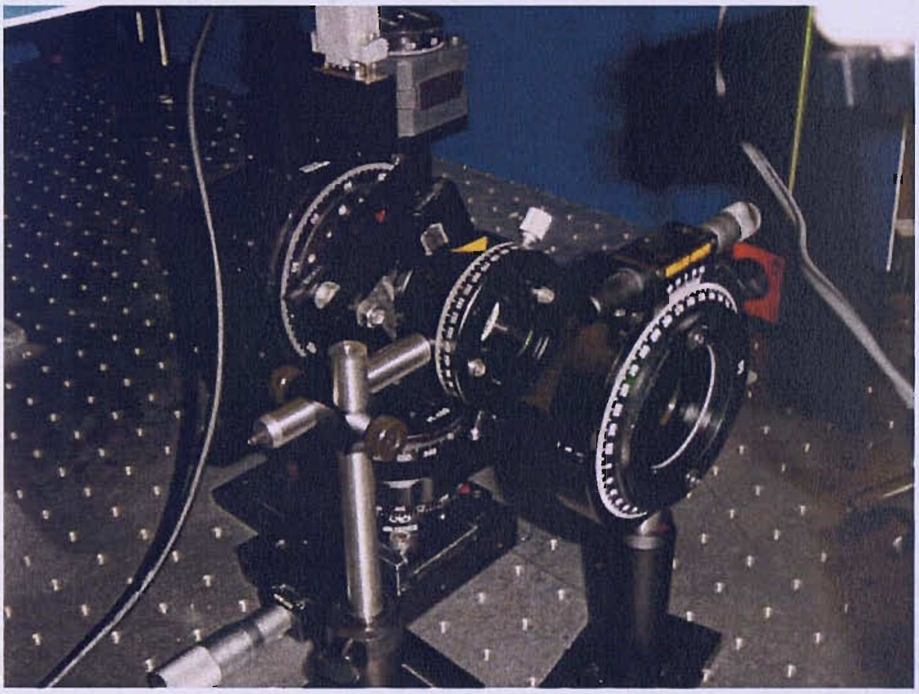

Figure 4.8. The computerised rotational stage used to rotate the hybrid cell.

The incident laser light was p-polarised and remained fixed throughout the experiment. The pump and signal beams were 11mW and 9mW respectively. For homeotropic alignment the interior surfaces of the Ce:SBN windows were coated with HTAB. The cells were assembled with the crystal c-axes parallel to the window edge and perpendicular to the 12.5μm thick copper foil spacers. The cells were filled with E7 LC.

4.4.3 Results

The following gain characteristics for a full and empty hybrid cell (figure 4.9) were obtained using the experimental procedure described in the previous section.

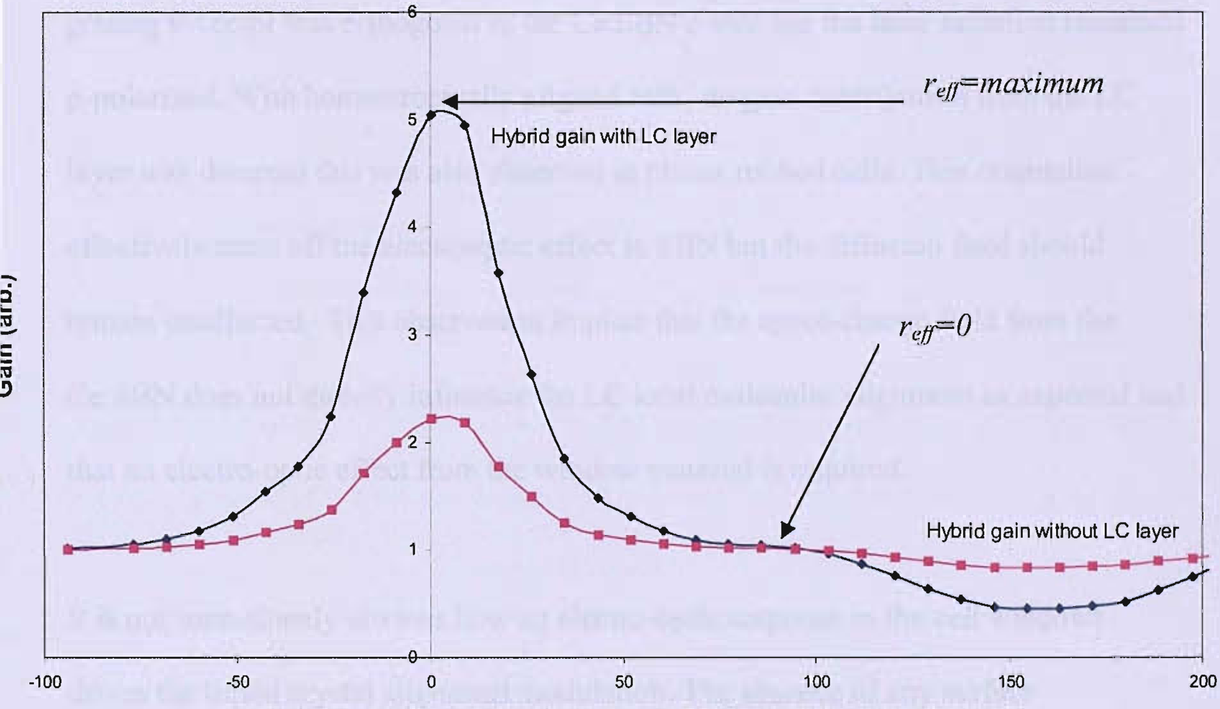

Figure 4.9. The gain as a function of the angle between the grating k vector and the crystal c axis in a hybrid with (blue data points) and without (pink data points) a liquid crystal layer.

The gain direction reverses depending on the sign of the effective electro-optic co-efficient accessed as the cell is rotated. The gain is greatest at 0 and 180^0 where the effective electro-optic co-efficient is greatest (equation 2.32 in chapter 2). The minimum gain angles are consistent with the angles at which the effective electro-optic co-efficient has been shown to be zero, from equation 4.12.

4.5 Discussion

The assumption that the Ce:SBN space-charge field was responsible for the LC modulation was investigated by rotating the hybrid cell through 90 degrees so the grating k-vector was orthogonal to the Ce:SBN c-axis but the laser radiation remained p-polarized. With homeotropically aligned cells, no gain contribution from the LC layer was detected this was also observed in planar rubbed cells. This orientation effectively turns off the electrooptic effect in SBN but the diffusion field should remain unaffected. This observation implies that the space-charge field from the Ce:SBN does not directly influence the LC local molecular alignment as expected and that an electro-optic effect from the window material is required.

It is not immediately obvious how an electro-optic response in the cell windows drives the liquid crystal alignment modulation. The absence of any surface corrugation shown by the AFM measurement implies that the piezoelectric effect is not responsible for coupling the inorganic response to the liquid crystal layer. As a check, the phase shift between the optical interference pattern and the refractive index grating was measured using a piezoelectrically driven mirror, as a function of cell rotation in the hybrid with and without a LC layer.

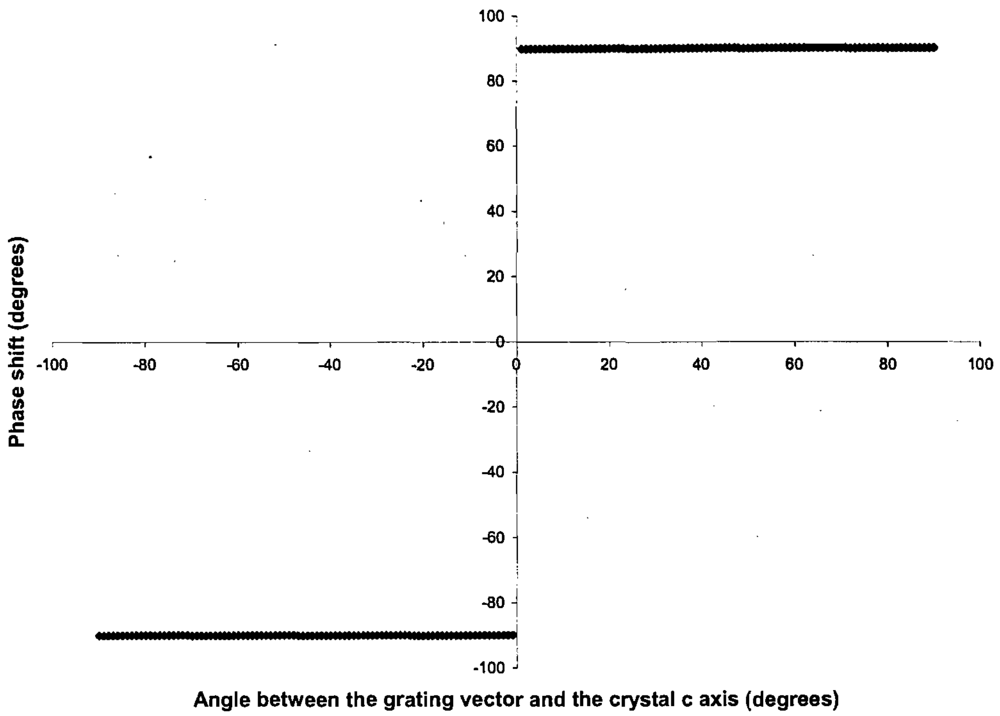

Figure 4.10. Phase shift between the optical interference pattern as a function of cell rotation in the hybrid with and without a LC layer. Zero degrees corresponds to when the c-axis is orthogonal to the grating k vector.

As shown in figure 4.10, the phase shift was either $+90^0$ or -90^0 depending on the sign of the effective electro-optic coefficient being accessed in the diffusion dominated Ce:SBN hybrid. When the c-axis is orthogonal to the grating k vector the effective electro-optic coefficient is zero therefore there is no refractive index grating so the phase shift is also zero.

To consider the possible effect of electrostriction, the two beam coupling gain was measured in a hybrid, filled with and without index matching fluid of similar viscosity and refractive index to the E7 liquid crystal, but no increased gain was detected. This result reinforces the importance of the dipolar nature of the LC molecules in a hybrid cell for gain amplification since this fundamental property was absent in the inert index matching fluid. This result also reinforces the requirement for LC reorientation for gain amplification that requires a driving space charge field rather than an effect that is dependent on electrostriction or piezoelectric effects.

The measured gain as a function of the angle between the grating k vector and the crystal c axis for a hybrid with and without a liquid crystal layer in figure 4.9 implies that the absence of gain at 90^0 is dominated by the Ce:SBN window since the characteristics are identical and in phase. It is still not clear why the refractive index grating in the SBN window is needed for gain to be exhibited by the LC layer. The space charge field created by diffusion should still exist 90^0 and be out of phase with the optical interference pattern at all angles.

To isolate the underpinning mechanism and verify the role of the LC layer, the small signal gain was measured in a planar aligned hybrid cell as a function of temperature. Specifically, the gain was measured through the nematic-isotropic phase transition of the liquid crystal. 5CB was chosen because its phase transition temperature ($35C^0$) is low enough to access without getting close to the Curie temperature of Ce:SBN (approximately 65°C). The crystal would de-pole if this temperature was reached. Figure 4.11 shows the results with and without LC layer.

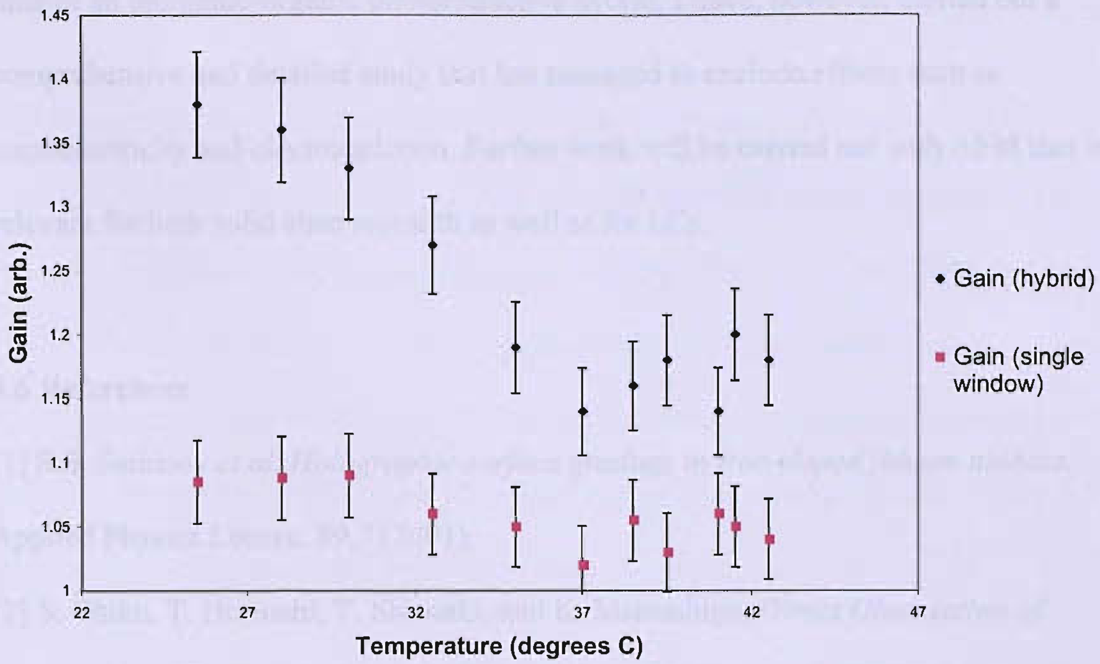

Figure 4.11 The small signal gain as a function of temperature with and without LC layer.

The gain in the hybrid drops significantly, from ~1.40 to ~1.15, as the temperature approaches the phase transition but the gain from the single window is unaffected within the experimental error. The difference in gain, ~0.07, between the hybrid and the single window at the phase transition temperature arises because the two gain measurements were taken at a slightly different place on the aperture of the SBN window i.e. it was due to the non-uniformity of the SBN window. This result implies that the liquid crystal phase and bulk reorientation of the molecules is of key importance to accentuate the gain from an inorganic window.

A satisfactory explanation of the coupling between the inorganic window and the liquid crystal layer has not been achieved. However, to maintain the focus of this thesis upon improving the nonlinear response the next chapter will build upon the concept of hybridisation and use a faster inorganic window to increase the response time of an inorganic-organic photorefractive hybrid. I have, however, carried out a comprehensive and detailed study that has managed to exclude effects such as piezoelectricity and electrostriction. Further work will be carried out with AFM that is relevant for both solid state research as well as for LCs.

4.6 References

[1] S.S. Sarkisov *et al. Holographic surface gratings in iron-doped lithium niobate.* Applied Physics Letters. 89,7 (2001).

[2] S. Chiku, T. Horiuchi, T. Shiosaki, and K. Matsushige, *Direct Observation of Photoinduced Gratings in LiNbO$_3$:Fe Single Crystals Using a Scanning Electron Microscope*, Jpn.J.Appl.Phys.34,5408 (1995).

[3] R.A.Rupp and E.Kratzig, *Investigation of refractive index gratings in electro-optic crystals by a microscope technique*, Phys.Stat.Solidi (a) 72,K5 (1982).

[4] S. C. Som, S. K. Ghorai and A. Satpathi, *Visualization of the photorefractive grating in BSO*, Optical and Quantum Electronics 25,241 (1993).

[5] BD Terris, JE Stern, D. Rugal, and HJ Mamin, *Contact electrification using force microscopy*, Phys.Rev.Lett.63,2669 (1989)

[6] S.D. Fantone. *Anamorphic prism: a new type.* Appl.Opt.30,5008-5009 (1991).

[7] L. Solymar, D.J.Webb, and A. Grunnet-Jepsen. *The Physics and Applications of Photorefractive Materials.* p416-417. Clarendon Press 1996.

Chapter 5 Potassium niobate hybrid photorefractive

In this chapter, two-beam coupling in a new hybrid photorefractive cell comprising a nematic liquid crystal layer influenced by an Fe doped $KNbO_3$ window is described. The use of potassium niobate promotes faster response times than the SBN hybrid device described in chapter 3. Full Bragg matched gain at large beam intersection angles is measured experimentally. The potassium niobate hybrid photorefractive is shown to exhibit perfect 90^o phase shifts between the optical and refractive index gratings, at normal incidence, without the need for an external field.

5.1 Introduction and KN Hybrid cell architecture

Chapter 3 reported a hybrid device that exploited Ce:SBN [1]. This chapter describes a hybrid device in which the refractive index of the LC layer is modulated by an adjacent iron-doped $KNbO_3$ photorefractive crystal. Perfect 90^o phase shifts occur for all grating spacings (274nm – 4μm) and full Bragg matched optical amplification has been achieved. The 90^0 phase shift was measured using the same technique reported in chapter 2 and Bragg diffraction was confirmed due to the presence of 0and +1 diffraction orders only. As with the Ce:SBN hybrid the device is entirely passive in normal incidence operation and no higher order beams are observed. The use of a potassium niobate window is expected to give a faster response time than that with Ce:SBN, which was ~120ms (chapter 2). A schematic of the $Fe:KNbO_3$ photorefractive hybrid is shown in figure 5.1.

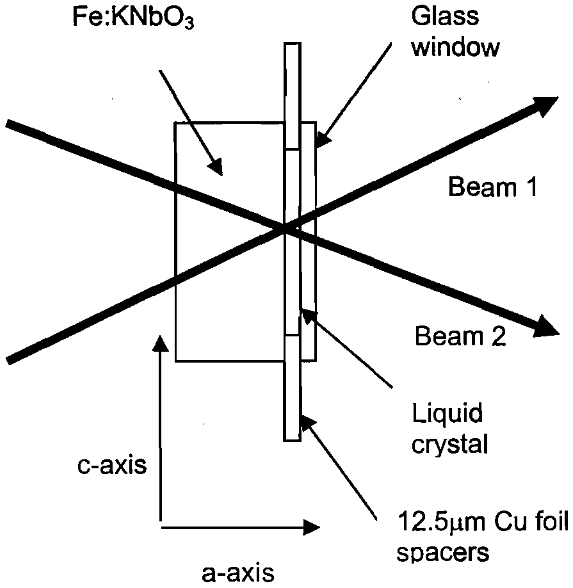

Figure 5.1. A schematic diagram of the $KNbO_3$ photorefractive hybrid and the two beam coupling geometry.

A 6 mm x 6 mm x 8 mm Fe: $KNbO_3$ crystal was used with a planar rubbed 12.5μm thick E7 liquid crystal layer. The crystal orientation is shown in figure 5.1. The a-c plane was chosen so that the single window results could be compared with those reported by [3]. The distance along the a-axis is 6mm. The interior faces of the photorefractive crystal and the glass window were first coated with a solution of 0.2mg of PVK (polyvinylcarbazole, average molecular weight of 1,100,000) dissolved in 10ml of chlorobenzene. The windows were spin coated at 5000rpm for 30s and allowed to dry in a fume cabinet for 3 hours. When dry, the PVK coated windows were uniaxially rubbed along the c-axis using a velour coated roller. The planar rubbed cell windows were assembled with the rubbing directions opposite to each other to avoid molecular alignment discontinuities arising from any surface molecular tilt. Once coated, the cell was assembled with the crystal c-axes parallel to the window edge and perpendicular to the 12.5μm thick copper foil spacers, as shown in figure 5.1. The foil was rolled between a glass cylinder and a glass plate prior to assembly to remove any edge burrs. The cells were filled with LC by capillary action through the exposed gap between the two spacer ends of the cell. The LC molecules were aligned so that their directors were parallel to the crystal c-axis (figure 5.1).

5.2 Two beam coupling in photorefractive hybrid

The physics underpinning the development of two-beam coupling gain inside a photorefractive material and a photorefractive hybrid has already been described in detail in chapters 2 and 3. The below theory, based on that reported in [2], provides a summary of the key equations that enable the gain to be calculated. These equations incorporate the electro-optic contribution specific for Fe: $KNbO_3$, unlike the theory in chapter 2, which is specific for Ce:SBN. The charge relocation properties cause the refractive index grating to be out of phase with the incident light pattern. Under these conditions energy can be transferred from one beam to the other. Crystal orientation and the sign of the dominant carrier determine the direction of the energy transfer. The two beam coupling gain is given by

$$\Gamma = \frac{2\pi n^3 r_{eff} E_w}{\lambda} \tag{5.1}$$

Where n is the effective refractive index, r_{eff} is an effective electro-optic tensor component, and E_w is the space charge field. The effective electro-optic coefficient can be related to the electro-optic tensor component of a fully poled crystal by [2]

$$r_{eff} = F r_{ang} \sigma' \tag{5.2}$$

Where F is a fractional poling factor, σ' is a normalised conductivity, and r_{ang} is the appropriate combination of electro-optic tensor components and angular polarisation factors for a fully poled crystal. There is usually one type of charge carrier, $\sigma' = +1$ for holes, and $\sigma' = -1$ for electrons [3]. The crystal and beam arrangements for the two beam coupling experiment are shown in figure 5.1. The two input beams were incident on the "a" surface of the crystal and were p-polarised so that the effective electro-optic co-efficient is [3]

$$r_{ang} = \frac{n_3^4 r_{33} \cos^2\theta - n_1^4 r_{13} \sin^2\theta}{n^4} \tag{5.3}$$

Where

$$n = \left[\left(\cos^2\theta / n_3^2\right) + \left(\sin^2\theta / n_1^2\right)\right]^{-1/2} \tag{5.4}$$

The space charge is given by

$$E_w = \left[2\pi k_B T / e\right]\left[\Lambda_g / \left(\Lambda_g^2 + \Lambda_0^2\right)\right] \tag{5.5}$$

Where Λ_g is the grating spacing and

$$\Lambda_0 = \left[4\pi\varepsilon\varepsilon_0 k_B T / \left(e^2 N_E\right)\right]^{1/2}$$

is the Debye screening length. Substituting for E_{sc} in equation (5.1) yields the photorefractive gain

$$\Gamma = \left[2\pi k_B T n^3 r_{eff} / \lambda e\right]\left[K_g / \left(K_g^2 + K_s^2\right)\right] \tag{5.6}$$

where $K_g = 2\pi / \Lambda_g$ and $K_s = 2\pi / \Lambda_o$. Using equation (5.5-5.6), the photorefractive gain and the space charge field as a function of angle between the signal and pump beams can be calculated from the following values, in agreement with those published in [3]: r_{eff}=-16.4 pm/V, N_E=0.07 x 10^{16} cm^{-3}, $F\sigma = r_{eff}/r_{33}$=-0.33, ε =55, n_1=2.169,

$n_3=2.28$, $r_{33}=64pm/V$, $r_{13}= 28pm/V$ and $\lambda=532nm$. The Debye screening length Λ_0=2.105μm.

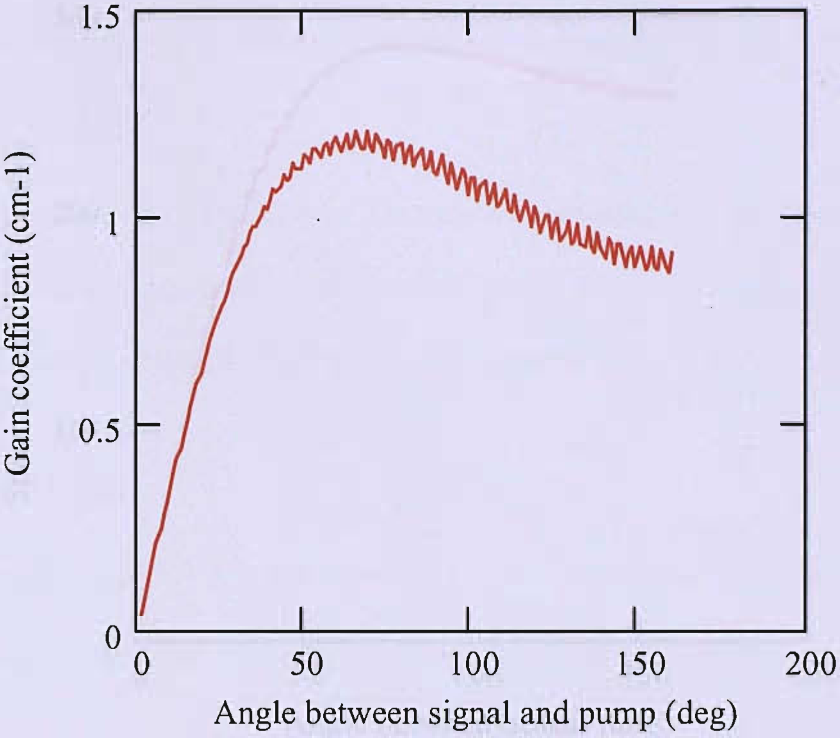

Figure 5.2. The predicted theoretical gain coefficient with a Debye screening length of 2.105μm as a function of angle between the signal and pump beams for Fe:KNbO$_3$. The small oscillations are numerical artefacts.

The small oscillations on the theoretical gain characteristic in figure 5.2 are numerical artefacts due to the limited number of points allowed by the mathematical programme used. They are not physical. It should also be noted that diffusion has been assumed to be dominant in the material over other mechanisms due to observation of a full 90^0 phase shift between the optical interference pattern and the diffraction grating written inside the Fe: KNbO$_3$ crystal. As such Reeve's theory [2], which is a first approximation, has been used that is shown later in this chapter to agree very well with experimental results.

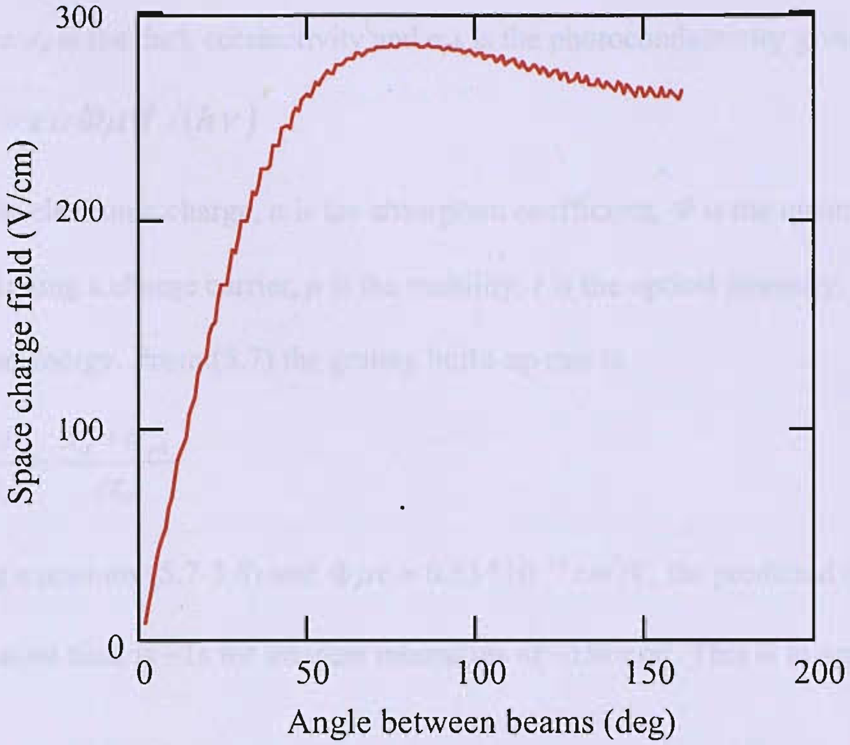

Figure 5.3. The predicted theoretical space charge field as a function of angle between the signal and pump beams for Fe:KNbO$_3$.

The liquid crystal molecules adjacent to the Fe:KNbO$_3$ re-orientate in response to the optical interference pattern in the same way as discussed in chapters 3 and 4 causing a refractive index modulation.

It is now necessary to work out the grating build up time to get a handle on the approximate response time of the hybrid device. Since the LC response time (~1ms) is much faster than that of potassium niobate the hybrid device is dominated by the response time of the potassium niobate window. For fringe spacings large compared to both the charge diffusion length and the Debye screening length, the dielectric relaxation time is a good approximation to the grating buildup time [3,4].

$$\tau_{di} = \varepsilon\varepsilon_0 / (\sigma_d + \sigma_{ph}) \tag{5.7}$$

Where σ_d is the dark conductivity and σ_{ph} is the photoconductivity given by

$$\sigma_{ph} = e\alpha\Phi\mu\tau I / (h\nu) \tag{5.8}$$

e is the electronic charge, α is the absorption coefficient, Φ is the quantum efficiency for exciting a charge carrier, μ is the mobility, I is the optical intensity, and $h\nu$ is the photon energy. From (5.7) the grating build-up rate is

$$\delta = \frac{1}{\tau_{di}} = \frac{\sigma_d + \sigma_{ph}}{\varepsilon\varepsilon_0} \tag{5.9}$$

Using equations (5.7-5.8) and $\Phi\mu\tau = 0.53 * 10^{-10}\, cm^2/V$, the predicted dielectric relaxation time is ~1s for incident intensities of ~1W/cm^2. This is in agreement with [3].

At this stage, before the hybrid device was characterised, the spectral transmission of the Fe: $KNbO_3$ window was measured using a Hewlett Packard 8453 spectrometer to confirm the level of absorption that will take place during two beam coupling in the crystal orientation shown in figure 5.1.

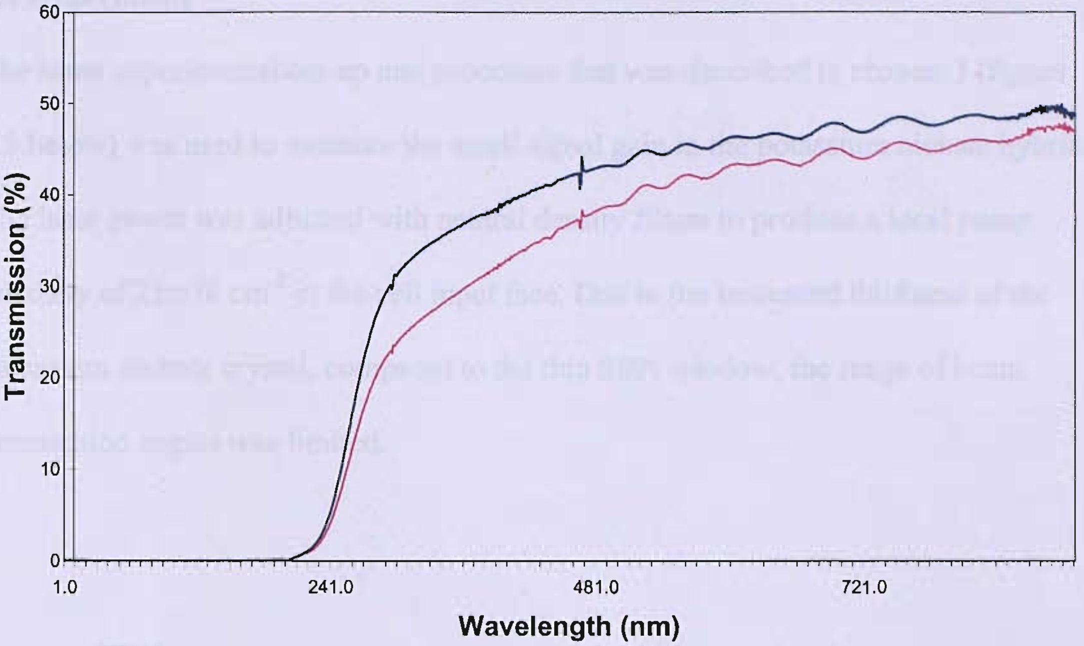

Figure 5.4. The transmission as a function of wavelength for Fe:$KNbO_3$ with the input light polarised parallel (blue line) to the crystal c-axis and perpendicular (pink line).

As shown in figure 5.4, the absorption was ~ 50% at 532nm with the input light polarised parallel to the crystal c-axis, allowing for reflection loss, compared to ~55% in the perpendicular direction. This level of absorption along the crystal c-axis was deemed adequate for demonstration of two beam coupling with only a 5% increase available in the orthogonal direction. This anisotropy in absorption could be due to the asymmetry of the crystal.

5.3 Experiment

The same experimental set-up and procedure that was described in chapter 3 (figure 5.5 below) was used to measure the small signal gain in the potassium niobate hybrid. The laser power was adjusted with neutral density filters to produce a local pump intensity of 25mW cm^{-2} at the cell input face. Due to the increased thickness of the potassium niobate crystal, compared to the thin SBN window, the range of beam intersection angles was limited.

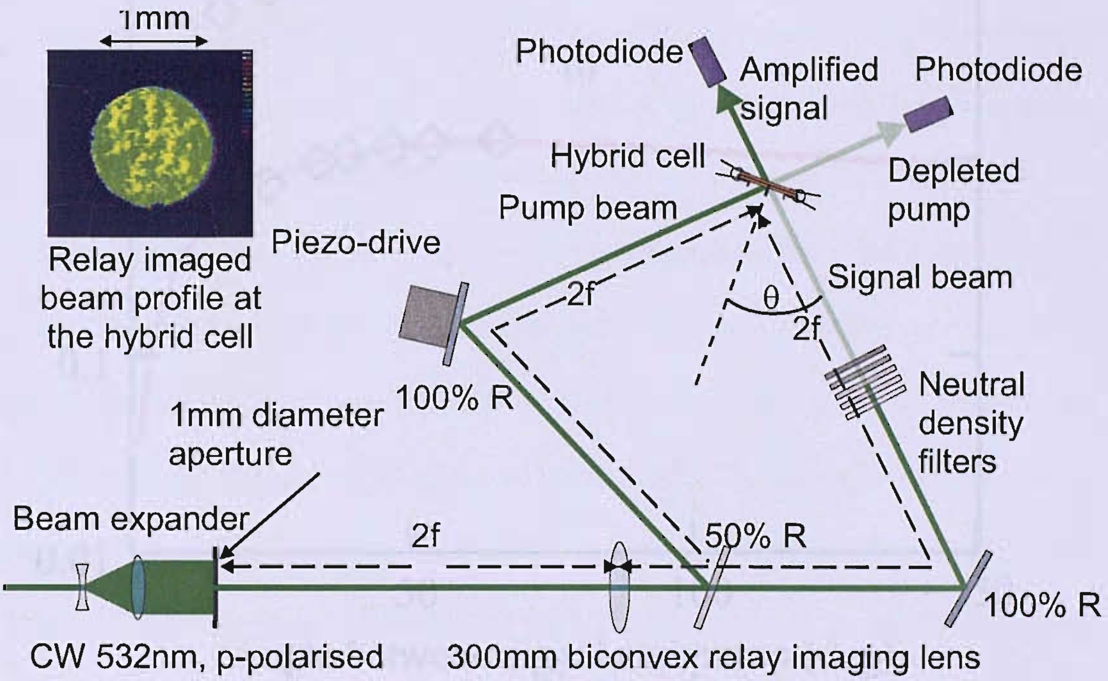

Figure 5.5. Experimental layout used to assess the Fe:KNbO$_3$ hybrid device.

5.4 Results

The small signal gain measurements (defined as the maximum gain in the undepleted pump regime) of the Fe:KNbO$_3$ window, with and without the liquid crystal layer, are shown in figure 5.6 as a function of beam intersection angle. Please note that this angle is not the half angle between the beams, as used in previous chapters. Also, the measured hybrid gain represents the gain coefficient from the 12.5μm liquid crystal layer only.

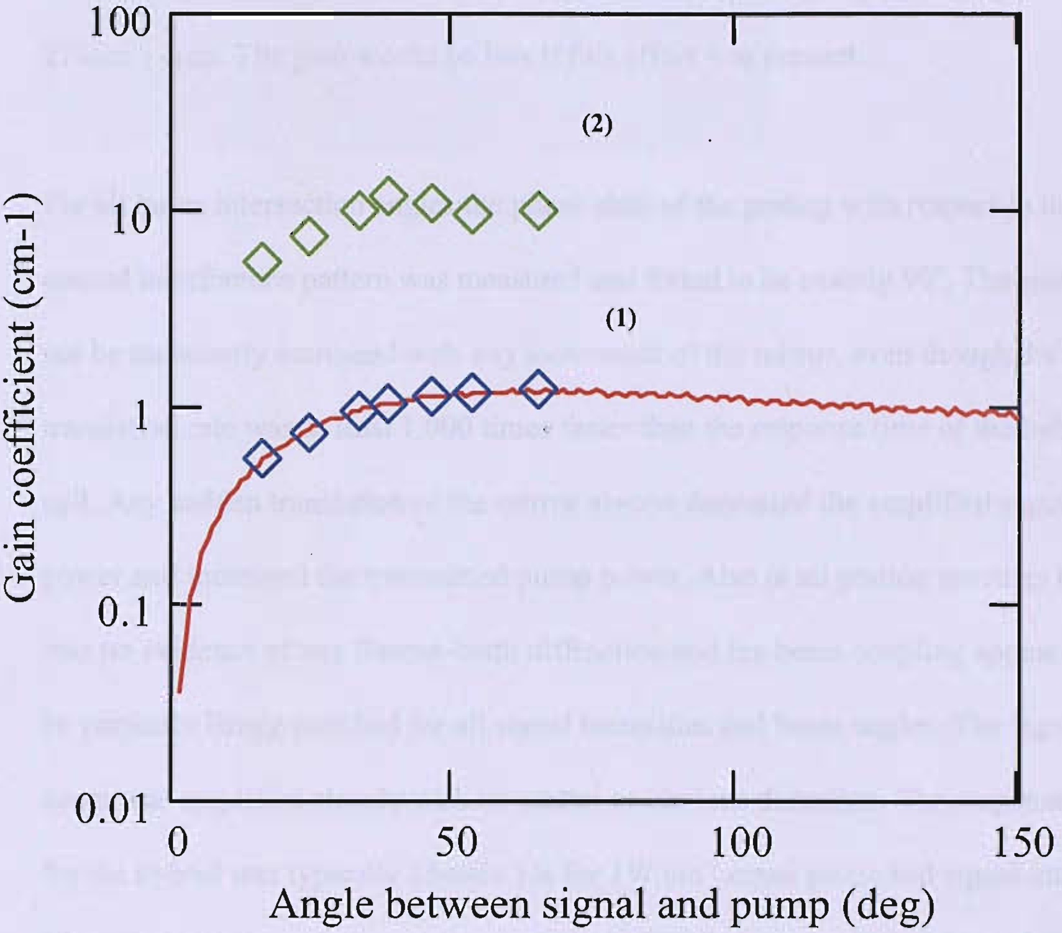

Figure 5.6. The small signal gain coefficient as a function of full beam intersection angle for: (1) a Fe:$KNbO_3$ window and (2) a Fe:$KNbO_3$ hybrid (liquid crystal contribution only). The red curve is the same theoretical characteristic shown in figure 5.2 [5]. The experimental error is within the experimental data point markers.

The experimental measurements for a single Fe:$KNbO_3$ window are in good agreement with theoretical values predicted by [3]. As shown by the very good fit of the theoretical gain characteristic with the measured gain coefficient. This is important as the theoretical fit assumes that the dominant charge is electrons rather than holes. So, as the fit agrees so well with the theory it is likely that this is the case and there is limited electron-hole competition within the grating spacing range of 274nm - 4µm. The gain would be less if this effect was present.

For all beam intersection angles the phase shift of the grating with respect to the optical interference pattern was measured and found to be exactly 90°. The gain could not be transiently increased with any movement of the mirror, even though the piezo translation rate was at least 1,000 times faster than the response time of the hybrid cell. Any sudden translation of the mirror always decreased the amplified signal power and increased the transmitted pump power. Also at all grating spacings there was no evidence of any Raman-Nath diffraction and the beam coupling appeared to be perfectly Bragg matched for all signal intensities and beam angles. The signal beam was amplified cleanly with no scatter or obvious distortion. The response time for the hybrid was typically 15msec 1/e for 1W cm^{-1} equal pump and signal intensity (figure 5.7), and approximately seconds in the small signal regime. For the Ce:SBN hybrid, the response time was typically 50msec 1/e for 1W cm^{-1} equal pump and signal intensity (figure 2.7 in chapter 2), and typically tens of seconds in the small signal regime. The measured response time of 15ms is much faster than the 1s response time predicted by theory. This could be due to a much larger quantum efficiency and mobility in the Fe:$KNbO_3$ crystal than initially predicted.

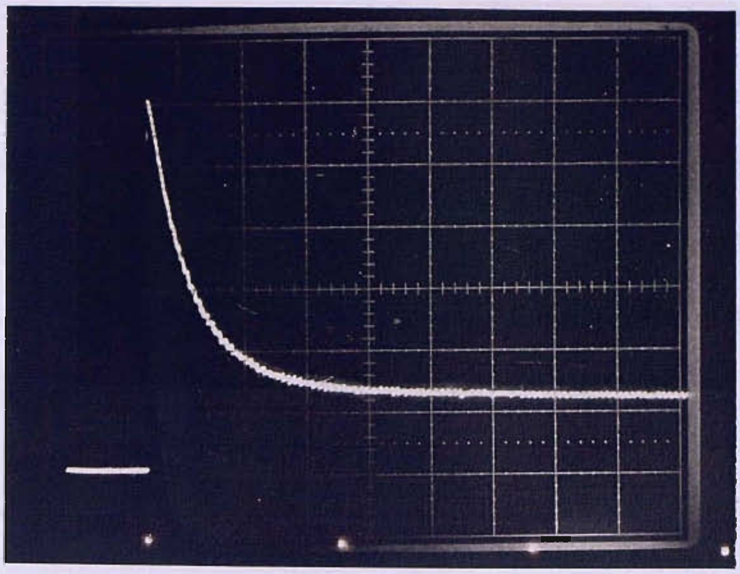

Figure 5.7. The response time characteristic for a Fe:KNbO$_3$ window (30ms/div time base).

5.5 Conclusions

In conclusion, the design of hybrid photorefractive systems comprising a nematic liquid crystal layer adjacent to a Fe:KNbO$_3$ photorefractive window has been described. Similarly as with SBN, with this arrangement, the inorganic window determines the underlying photorefractive characteristics of the whole system while the LC layer significantly enhances the total photorefractive gain. Using this technique full Bragg matched optical amplification has been achieved over wide beam intersection angles, with perfect 90° phase shifts between the optical and refractive index gratings at normal incidence, without the need for an external field. These results show that the data obtained with SBN hybrid systems (in chapter 3) are not specific to SBN. The two beam coupling response of other photorefractives can also be enhanced by a liquid crystal layer. However, the peak gain exhibited by the Fe:KNbO$_3$ hybrid was ~20cm^{-1} compared to a much larger gain of ~1500cm^{-1} for the Ce:SBN hybrid reported in chapter 3 using the same LC and alignment. This difference in gain between the two hybrids is partly due to the large difference in the magnitude of the space charge fields, 500V/cm in the Ce:SBN window compared to ~270V/cm in the Fe:$KNbO_3$ window, and the poor quality of the Fe:$KNbO_3$ crystal (discussed in chapter 7). In addition, I have demonstrated that using potassium niobate, compared to SBN, reduces the overall response time of the inorganic-organic hybrid photorefractive from ~50ms to ~15ms.

5.6 References

[1] G. Cook, C Wyres, M Deer, D Jones *Hybrid organic-inorganic photorefractives*, SPIE vol.5213, 2003.

[2] M.B.Klein et al. Journal of Applied Physics. 57, 4901 (1985).

[3] R.J.Reeves *et al. The photorefractive properties of* $KNbO_3$. The American Physical Society Physical review B. **43** 1 January 1991.

[4] P.Gunter, Phys. Rep. 93, 199 (1982)

[5] M Deer, *Demonstration of an Fe doped KNbO3 photorefractive hybrid*, Applied Physics Letters, **88**, 254107 (2006).

Chapter 6 Demonstration of a tandem contra-directional photorefractive

In this chapter, the theory of the reflection geometry photorefractive effect that was introduced in chapter 1 is discussed and compared with the transmission geometry photorefractive effect, also described in chapter 1. The major advantage of utilising the reflection geometry photorefractive effect over the transmission geometry is finer wavelength selectivity can be achieved and no beam splitting optics are required to create two beam coupling inside the photorefractive crystal. Two beam coupling is achieved by the Fresnel reflection off the rear face of the crystal interfering with the input beam. For applications where there are weight and size constraints, less optical components in a system is very important, and it can keep the design costs down. Fe:$KNbO_3$ and Fe:$LiNbO_3$ have been chosen to investigate here because Fe:$LiNbO_3$ is well known for it's high gain properties [1] and Fe:$KNbO_3$ is very fast [1,3]. Both crystals have been doped with iron because of irons compatibility with the crystal lattice of each material in terms of molecular size and the donor and acceptor states it offers (this has already been discussed in chapter 1). The change in optical density characteristics for Fe:$KNbO_3$ and Fe:$LiNbO_3$ are calculated using standard photorefractive theory in this chapter found in [1]. The change in optical density and response times are then measured for three crystals; a commercially grown piece of Fe:$LiNbO_3$, an in-house grown Fe:$KNbO_3$ crystal, and a commercially grown Fe:$KNbO_3$ crystal. The experimental results agree well with the theoretical values enabling the performance of each material to be assessed. A novel tandem device is then demonstrated that exploits the fast but currently small change in optical density from potassium niobate and the large but slower response of lithium niobate.

6.1 Theory

The aim of the following theory is to derive and calculate the change in optical density of the input intensity relative to the output intensity that is developed via two beam coupling inside a photorefractive window. The change in optical density is derived from the two beam coupling gain. Equations (6.1) to (6.15) can be found in [1].

In the reflection geometry the incident light beams will still create an interference pattern, electrons will be ionised by the photon intensity, and they diffuse, or drift if an electric field is applied along the crystal, and set-up a space charge field. The space charge field will cause a change in the dielectric constant if the appropriate electro-optic coefficients are accessed. Compared to the transmission grating, the main difference is that a reflection grating is obtained that will reflect the incident beam back along its path. The physics is otherwise the same [1] and already discussed in depth in chapter 1.

The field equations discussed in chapter 2 assumed that the two waves are incident symmetrically at angles $+\theta$ and $-\theta$. In this case, the beams are incident at angles θ and $\pi-\theta$. In the transmission configuration the space charge field varied periodically in the z direction and the optical electric fields varied in the x direction. For the reflection geometry both types of field vary in the x direction but the governing coupled wave equations are not affected by the direction in which the space charge field has a periodic variation. The following treatment is from [1]. With new incident angles of θ and $\pi-\theta$ the wave vector $\underline{k}_1$ is still the same but $\underline{k}_2$ is of the form [1]

$$\underline{k}_2 = k\left(-\underline{i}_x \cos\theta + \underline{i}_z \sin\theta\right) \tag{6.1}$$

Resulting in the new coupled wave equations

$$\frac{\partial \varepsilon_1}{\partial x} + j\frac{F k_0}{2\varepsilon_{ro}^{1/2}\cos\theta}\varepsilon_2 = 0 \tag{6.2}$$

$$\frac{\partial \varepsilon_2}{\partial x} + j\frac{F^{*} k_0}{2\varepsilon_{ro}^{1/2}\cos\theta}\varepsilon_1 = 0 \tag{6.3}$$

Where ε_1 and ε_2 are the amplitudes of the electric fields, ε_{r0} is the unperturbed relative optical dielectric constant, and $F= -\varepsilon_{r0}^{2} r_{eff} E_w \varepsilon_1 \varepsilon_2^{*}/I_0$ (see chapter 2 for variable definition). Hence the only change is the sign of the second term of the second differential equation. The modulus and the phase of the optical electric field can now be introduced leading to the differential equations in terms of intensity and phase angle

$$\frac{\partial I_1}{\partial x} + \Gamma\frac{I_1 I_2}{I_1 + I_2}\sin\Phi = 0 \tag{6.4}$$

$$\frac{\partial I_2}{\partial x} + \Gamma\frac{I_1 I_2}{I_1 + I_2}\sin\Phi = 0 \tag{6.5}$$

$$\frac{\partial \Psi}{\partial x} + \frac{\Gamma}{2}\frac{-I_1 - I_2}{I_1 + I_2}\cos\Phi = 0 \tag{6.6}$$

By integrating equation (6.6) and using the fact $(-I_1 - I_2)/(I_1 + I_2) = -1$

$$\Psi = \frac{\Gamma}{2} x\cos\Phi \tag{6.7}$$

where Ψ is the phase difference between beams 1 and 2. Equation (6.7) implies for the reflection case the difference in the phase angles always varies linearly. The solution for the intensities is

$$\frac{I_1(x)}{I_{10}} = \frac{1}{2\beta}\left\{\beta - 1 + \left|\left[(\beta - 1)^2 + 4\beta\exp(-\Gamma x)\right]^{1/2}\right|\right\} \tag{6.8}$$

$$\frac{I_2(x)}{I_{10}} = \frac{1}{2\beta}\left\{\beta - 1 + \left|\left[(\beta - 1)^2 + 4\beta\exp(-\Gamma x)\right]^{1/2}\right|\right\} \tag{6.9}$$

Where β denotes the intensity ratio of beam 1 to beam 2 at $x=0$. β can be expressed in terms of the intensity ratio of the incident beams

$$M = \frac{I_1(0)}{I_2(l)} \tag{6.10}$$

with which β can be expressed as

$$\beta = \frac{M}{1+M}\left[1 + M\,exp(-\Gamma\,l)\right] \tag{6.11}$$

The output to input intensity ratios of the beams can be written as

$$u_1 = \frac{I_1(l)}{I_1(0)} \qquad u_2 = \frac{I_2(0)}{I_2(l)} \tag{6.12}$$

From equations (6.10) and (6.11)

$$u_1 = \frac{1+M}{M + exp(\Gamma\,l)} \tag{6.13}$$

$$u_2 = \frac{1+M}{M + exp(-\Gamma\,l)} \tag{6.14}$$

When considering power conservation it is no longer true that the total beam power is conserved as the two beams move along the x axis, as in the transmission configuration. But it must still be true that the total input power must be equal to the total output power so that the conservation of energy law is obeyed

$$I_1(0)+I_2(l)=I_1(l)+I_2(0) \tag{6.15}$$

6.2 Calculation of gain for Fe doped lithium niobate and potassium niobate

In the reflection geometry the photorefractive effect is ideally suited for use at a focal plane because the Fresnel reflection provides the second beam for optical interference. It is more challenging to use a transmission grating in a focal plane because careful alignment is needed to ensure the two beams are overlapping at the focus. In this geometry it is important to consider the peak intensity at the focal plane that drives the photorefractive effect. The peak intensity at the focus of a lens is dependent on the lens f-number. As the lens f-number is increased, by increasing the focal length of the lens and keeping the beam diameter constant, the peak intensity decreases. As the peak intensity decreases less charge is being excited and trapped. The resulting grating contrast is reduced, and hence the resulting diffraction efficiency is reduced. The reflected beam will therefore be smaller. The peak intensity at the beam focus can be calculated using standard Gaussian beam propagation theory. The radial intensity profile of the focused Gaussian laser beam is given by [1]:

$$I = I_0 e^{-2\left(\frac{r}{\omega_0}\right)^2} \tag{6.16}$$

where r is the local radius and I_0 is the peak intensity at the centre of the Gaussian beam. The total power, P, of a Gaussian beam is given by:

$$P = \int_{r=0}^{\infty} I.2\pi r.dr = 2\pi I_0 \int_0^{\infty} r.e^{-2\left(\frac{r}{\omega_0}\right)^2} dr = 2\pi I_0 \frac{\omega_0^{\,2}}{4} \tag{6.17}$$

The peak intensity is therefore given by:

$$I_0 = \frac{2P}{\pi \omega_0^{\,2}} \tag{6.18}$$

Using equations (6.1-6.14) and (6.16-6.18) the following change in optical density characteristics for iron doped potassium niobate and iron doped lithium niobate have been calculated as a function of lens f-number (the ratio of beam diameter to the lens focal length) using Mathcad. The optical density is given by $OD=log_{10}(I_{input}/I_{output})$. The $1/e^2$ spot radius, ω_0, at the focus of each lens was determined experimentally using a CCD camera to image the focus of the laser beam.

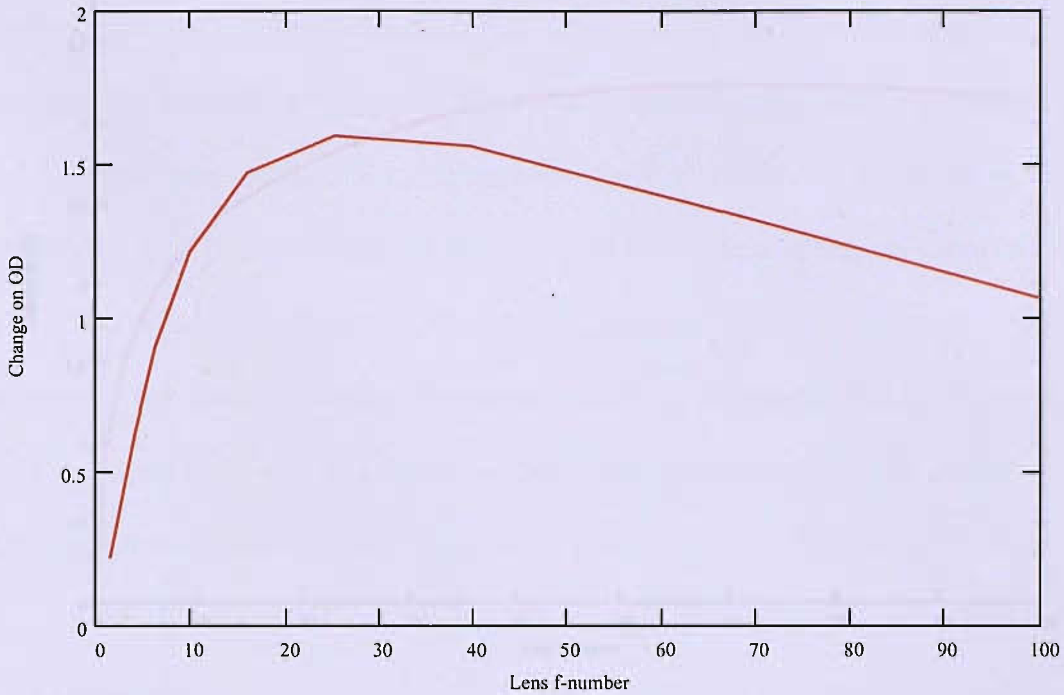

Figure 6.1. Theoretical plot of change in optical density as a function of f-number for a Fe:KNbO$_3$ (0.1% Fe) crystal and a 5mW input power pump beam focused in the middle of the crystal (λ=532nm). The crystal thickness was 5mm.

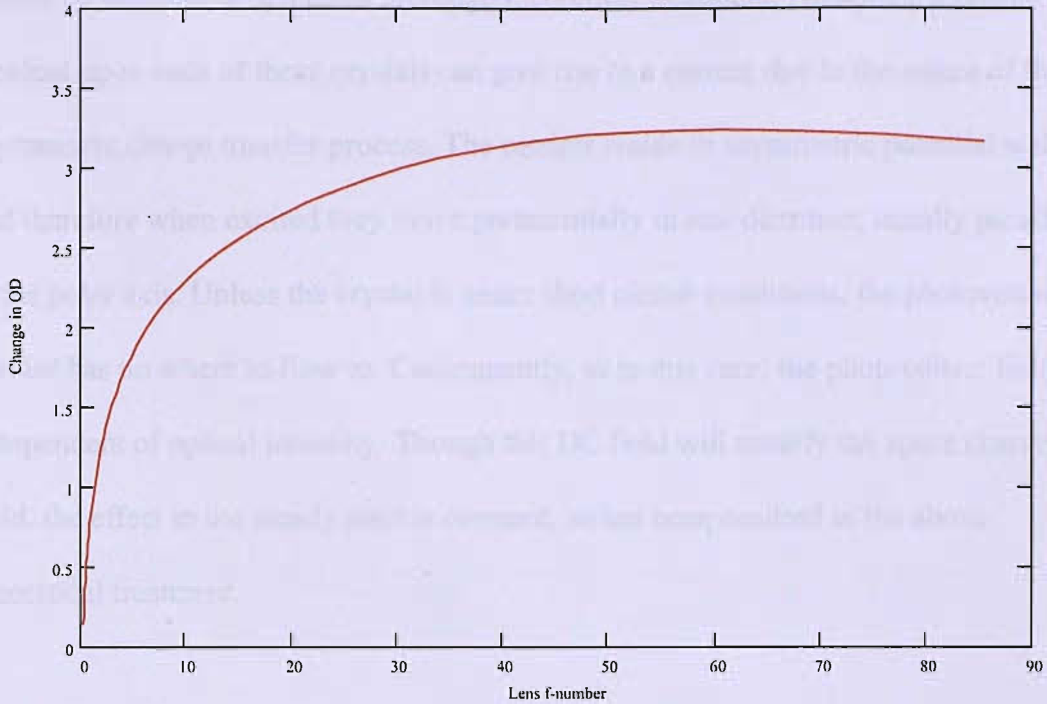

Figure 6.2. Theoretical plot of change in optical density as a function of f-number for a Fe:LiNbO$_3$ (0.05% Fe) crystal and a 5mW input power pump beam (λ=532nm) focused in the middle of the crystal. The crystal was uncoated and 3.6mm thick.

The differences in the two optical density characteristics are due to the difference in the peak gain co-efficient for the two materials. A peak gain co-efficient of 100cm^{-1} was used for Fe:LiNbO$_3$ in agreement with reference [2]. A dark conductivity of 1000Wm^{-2} was used for the optical density characteristic for Fe:LiNbO$_3$ and 3500Wm^{-2} for Fe:KNbO$_3$ in agreement with [1,2]. The use of these fitting parameters provides an efficient means of obtaining a good theoretical fit with experimental data. The change in optical density approaches zero as the f-number approaches zero because of the increase in peak intensity. The dark conductivity increases with intensity and competes against grating formation. However, is should be noted that the photovoltaic effect in Fe:LiNbO$_3$ and Fe:KNbO$_3$ can be very prominent and should be considered in a more thorough theoretical treatment. An optical intensity incident upon each of these crystals can give rise to a current due to the nature of the asymmetric charge transfer process. The carriers reside in asymmetric potential wells and therefore when excited they move preferentially in one direction, usually parallel to the polar axis. Unless the crystal is under short circuit conditions, the photovoltaic current has no where to flow to. Consequently, as in this case, the photovoltaic field is independent of optical intensity. Though this DC field will modify the space charge field, the effect in the steady state is constant, so has been omitted in the above theoretical treatment.

6.3 Experiment

The experimental arrangement used to measure the change in optical density as a function of input lens f-number is shown in figure 6.3. A Faraday isolator was placed between the laser (a 5 W 532nm Coherent Verdi) and the experiment, as the strong photorefractive back-scattered light has been observed to disrupt the frequency locking of the laser in previous experiments. Although the laser output can be adjusted at the control panel, the minimum output of 500mW was too high for this experiment. Therefore the laser power was adjusted using a half-waveplate and polariser combination (both A/R coated at 532nm). This attenuation method also ensured that the laser beam profile remained constant during the experiment. Neutral density (ND) filters were not used because high value ND filters can experience thermal aberrations and low value ND filters introduce interference fringes to the beam (our ND filters were not A/R coated). A further problem with ND filters is angular displacement of the transmitted beam. Most ND filters are not parallel and this causes the transmitted beam to deviate slightly with each new measurement which, although this has little effect in the near field, seriously impacts on the far field measurements. These problems are avoided by using the half-waveplate and polariser combination. The incident laser light was p-polarised.

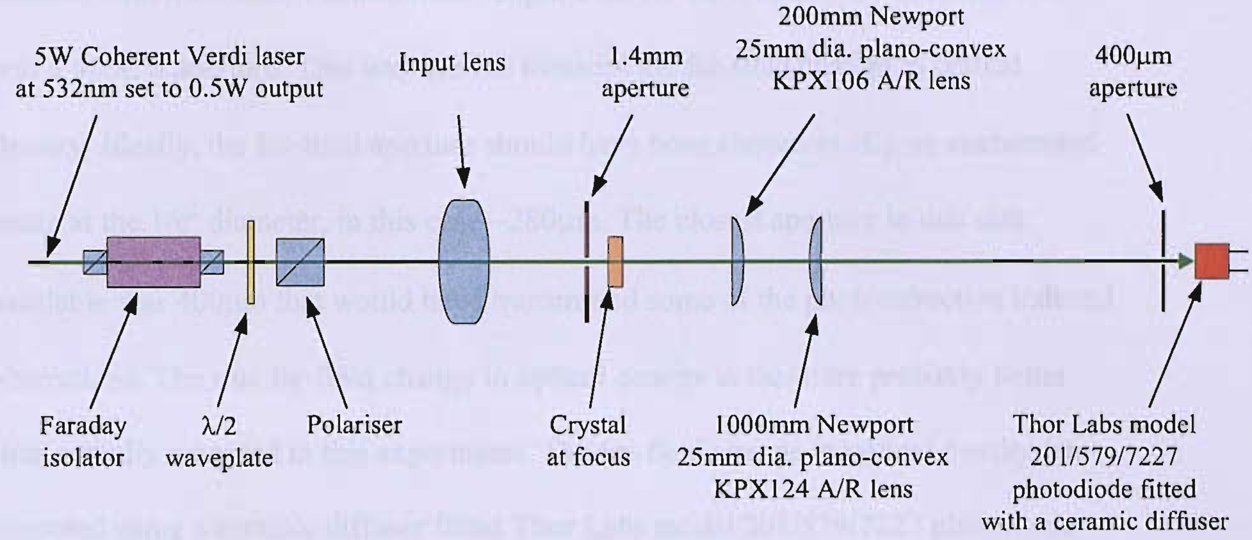

Figure 6.3. The experimental arrangement used for measuring the change in optical density as a function of input lens f-number. The f-number was varied using a range of different focal length input lens.

An appropriate input bi-convex focusing lens was used to focus the beam into the mid-point of the Fe:LiNbO$_3$ or Fe:KNbO$_3$ crystal at the desired f-number. A 1.4mm aperture placed 160mm behind this lens (40mm from the crystal) acted as a shield for weak stray reflections from the surfaces within the input lens. During the experiment the crystals were aligned normal to the input beam such that its Fresnel reflection exactly counter-propagated with respect to the input beam. The crystals were orientated with the positive c-axis face at the rear of the crystal. The rear face of each sample has been marked with a black dot (which can be removed with alcohol).

Owing to the long-term memory of Fe:$LiNbO_3$, the crystal was translated between each measurement to avoid superimposing reflection holograms. After passing through the crystal, the laser beam was first recollimated with a 25mm diameter 200mm focal length Newport brand A/R coated plano-convex lens and then re-focused with a similar 1000mm focal length lens. At the focus of the 1000mm lens was a 400μm aperture. This was used to measure the far-field change in optical density. Ideally, the far-field aperture should have been chosen to clip an unaberrated beam at the $1/e^2$ diameter, in this case ~280μm. The closest aperture to this size available was 400μm that would have transmitted some of the photorefractive induced aberrations. The true far-field change in optical density is therefore probably better than actually recorded in this experiment. The far-field change in optical density was recorded using a ceramic diffuser fitted Thor Labs model 201/579/7227 photodiode connected to an oscilloscope, placed immediately behind the 400μm pinhole aperture.

6.4 Results

Using the above experimental set-up the change in optical density was measured for three crystals; a commercially grown piece of Fe:LiNbO$_3$ (Fe 0.05%), an in-house grown Fe:KNbO$_3$ (Fe 0.01%) crystal, and a commercially grown Fe:KNbO$_3$ (Fe 0.1%) crystal. All three samples are pictured below in figure 6.4.

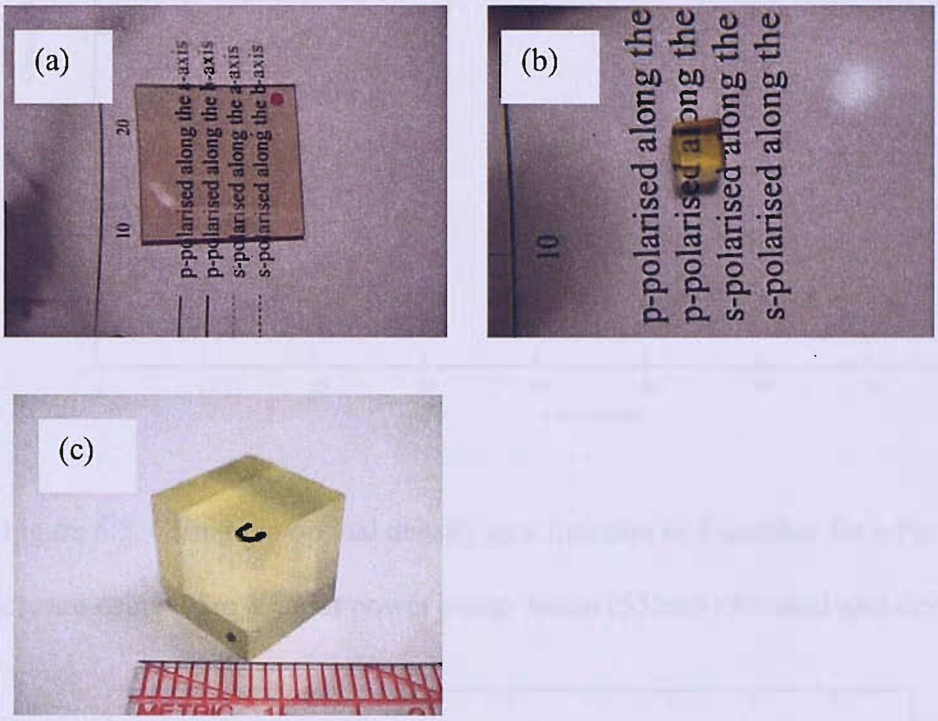

Figure 6.4. (a) A commercially grown piece of Fe:LiNbO$_3$ (Fe 0.05%), (b) an in-house grown Fe:KNbO$_3$ (Fe 0.01%) crystal, (c) and a commercially grown Fe:KNbO$_3$ (Fe 0.1%) crystal.

The following optical density ($OD=log_{10}(I_{input}/I_{output})$) characteristics were measured as a function of input lens f-number using an input pump intensity of 5mW.

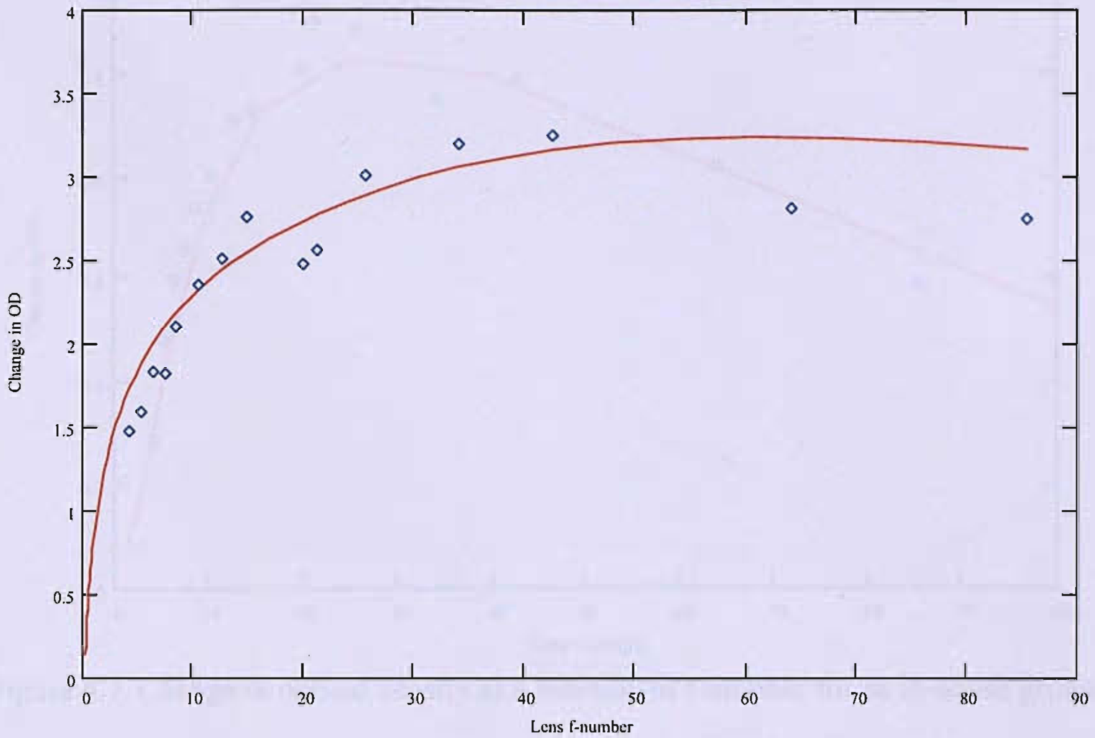

Figure 6.5. Change in optical density as a function of f-number for a Fe:LiNbO$_3$ crystal using a 5mW input power pump beam (532nm) focused mid-crystal.

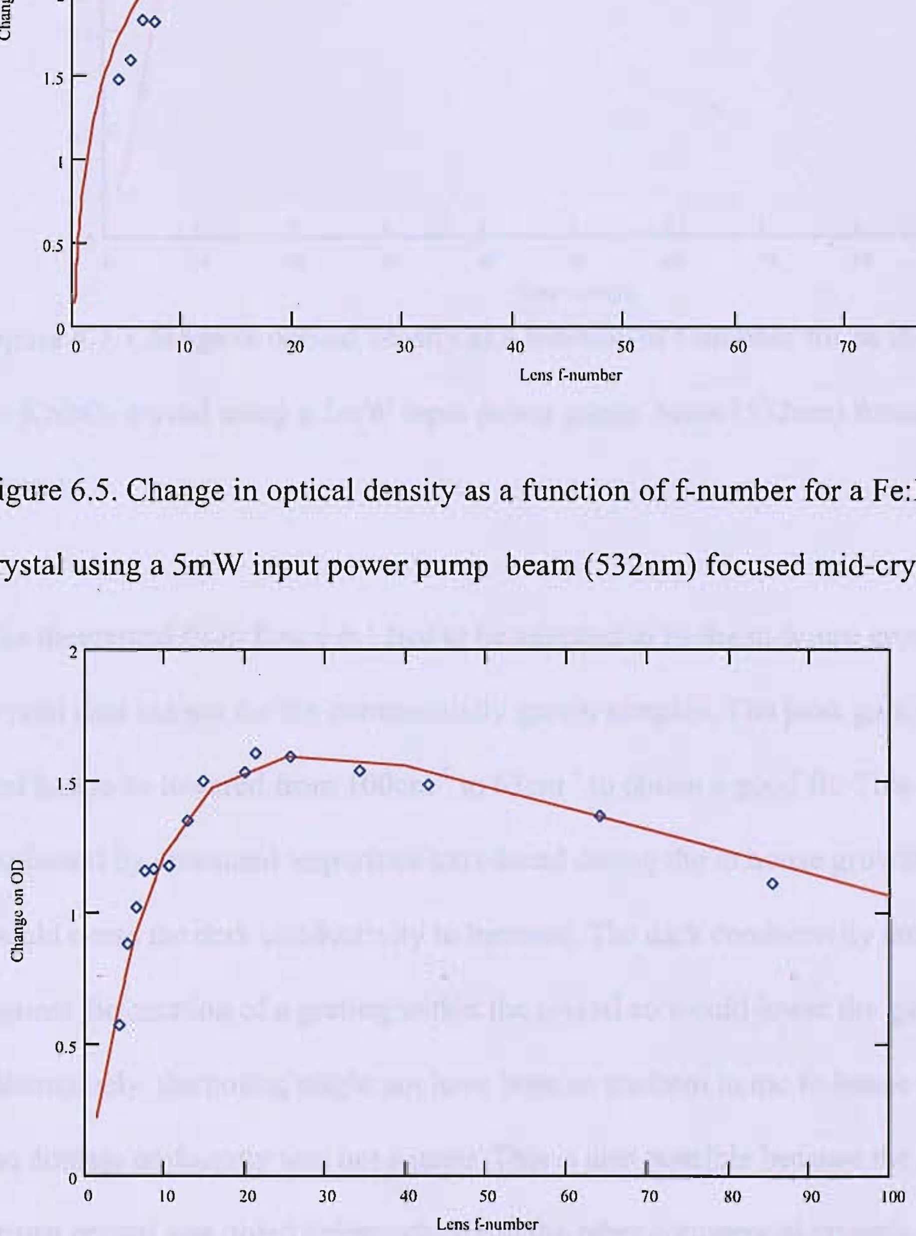

Figure 6.6. Change in optical density as a function of f-number for a Fe:KNbO$_3$ crystal using a 5mW input power pump beam (532nm) focused mid-crystal.

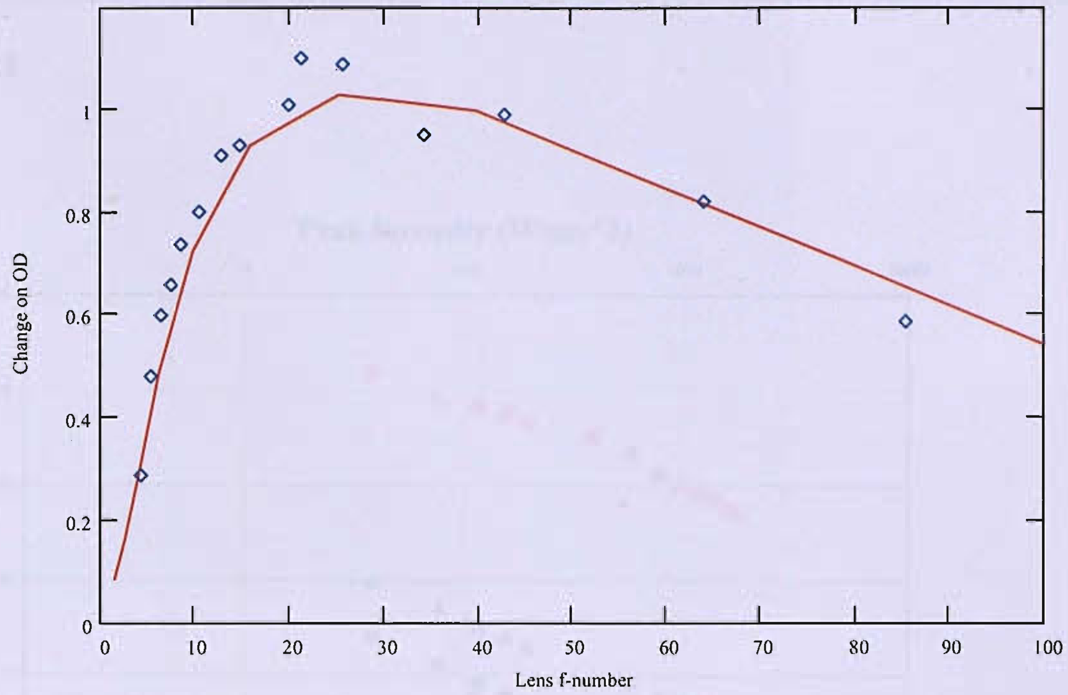

Figure 6.7. Change in optical density as a function of f-number for an in-house grown Fe:KNbO$_3$ crystal using a 5mW input power pump beam (532nm) focused mid-crystal.

The theoretical fit in figure 6.1 had to be adjusted to fit the in-house grown Fe:KNbO$_3$ crystal data but not for the commercially grown samples. The peak gain co-efficient and had to be lowered from 100cm^{-1} to 63cm^{-1} to obtain a good fit. This could be explained by unwanted impurities introduced during the in house growth process that would cause the dark conductivity to increase. The dark conductivity competes against the creation of a grating within the crystal so would lower the gain or alternatively, the poling might not have been so uniform in the in-house crystal so that the domain uniformity was not a good. This is also possible because the in-house grown crystal was poled independently to the other commercial crystals. The 1/e response times were also measured as a function of input intensity using a well corrected 200mm focal length lens (CVI LAP series A/R coated at 532nm), see figure 6.8.

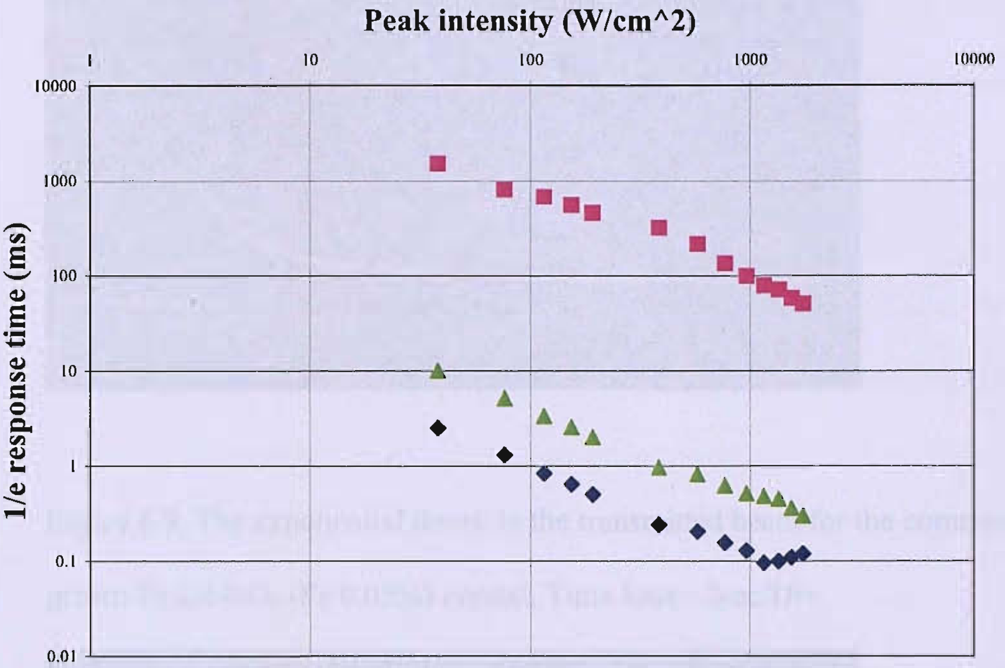

Figure 6.8. The response time as a function of peak intensity for: (pink data points) Commercially grown Fe:LiNbO$_3$ (Fe 0.05%), (green data points) in-house grown Fe:KNbO$_3$ (Fe 0.01%), and (blue data points) commercially grown Fe:KNbO$_3$ (Fe 0.1%).

The measured response time characteristics, in terms of gradient and magnitude, were in agreement with [1,2]. The oscilloscope traces of the exponential decay in the transmitted beam for the commercially grown Fe:LiNbO$_3$ (Fe 0.05%) and Fe:KNbO$_3$ (Fe 0.1%) crystals at an input peak intensity of 100 Wcm^{-2} are shown in figures 6.9 and 6.10 respectively.

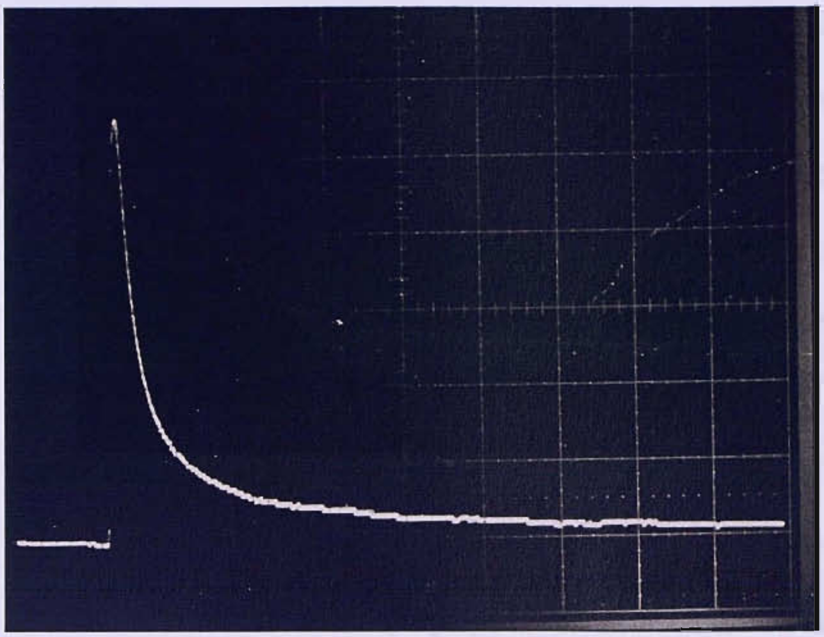

Figure 6.9. The exponential decay in the transmitted beam for the commercially grown Fe:LiNbO$_3$ (Fe 0.05%) crystal. Time base ~2sec/Div.

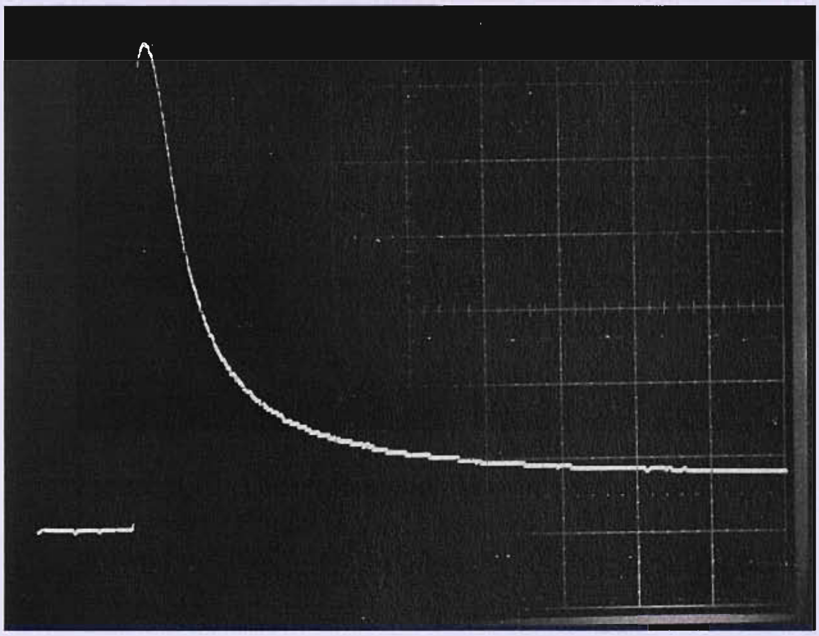

Figure 6.10. The exponential decay in the transmitted beam for the commercially grown Fe:KNbO$_3$ (Fe 0.1%) crystal. Time base 1msec/Div.

The measured change in optical density for both commercially provided samples was in good agreement with the predicted characteristics. However the in-house crystal data was not, the gain, and consequently the change in optical density, was lower. This is likely to be due to differences in the growth process rather than the characterisation since the optical characterisation was the same for both crystals. It would be useful to study the chemical composition of each crystal at this point to establish whether any impurities have been introduced. The development of crystal growth is discussed in chapter 7.

The significance of these results is apparent when compared with the response times of each material. The $LiNbO_3$ crystal offers the much needed high change in optical density for filter applications but on a much longer time scale (~460ms). Whereas the $KNbO_3$, due to its smaller peak gain co-efficient, did not exhibit such high change in optical density, only half that of $LiNbO_3$, but its response time was very fast <10ms. To harness these attractive attributes from both materials the commercially grown crystals of $LiNbO_3$ and $KNbO_3$ were used in tandem, figure 6.11. This concept was investigated to try and combine the optical density and transient response of both materials in a single device. A large f-number lens was chosen (~50) to ensure that the focus was constant throughout the length of both materials and the input peak intensity was adjusted to 10 Wcm^{-2}.

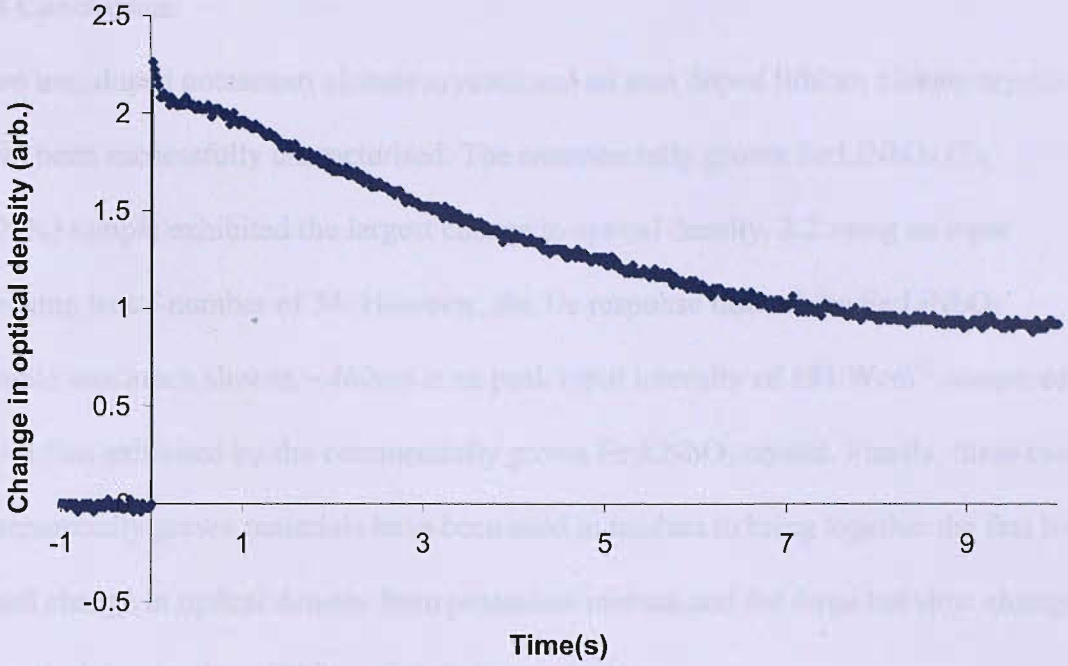

Figure 6.11. The optical density as a function of time for $LiNbO_3$ and $KNbO_3$ used in tandem.

The 532nm laser light was incident on first the $KNbO_3$ crystal and then the $LiNbO_3$ crystal that were held together using an optical mount. As shown in figure 6.11, an initial sharp change in optical density is provided during the first 100ms of exposure. This response time compares closely to the response time measured for $KNbO_3$, using figure 6.8 and extrapolating to a peak intensity of 10 Wcm^{-2}. It can therefore be associated with the $KNbO_3$ crystal. After ~100ms the $LiNbO_3$ becomes dominant and provides characteristic large but slow change in optical density. This result is very important for applications where controlling the optical transmission of a laser beam in a focal plane geometry is required, and where there are weight and volume constraints.

6.5 Conclusions

Two iron doped potassium niobate crystals and an iron doped lithium niobate crystal have been successfully characterised. The commercially grown Fe:$LiNbO_3$ (Fe 0.05%) sample exhibited the largest change in optical density, 3.2 using an input focusing lens f-number of 54. However, the 1/e response time of the Fe:$LiNbO_3$ sample was much slower, ~460ms at an peak input intensity of 191 Wcm^{-2} compared to ~0.5ms exhibited by the commercially grown Fe:$KNbO_3$ crystal. Finally, these two commercially grown materials have been used in tandem to bring together the fast but small change in optical density from potassium niobate and the large but slow change in optical density from lithium niobate in one device.

6.6 References

[1] Solymar L, Webb D J and Grunnet-Jepsen A. *The physics and applications of photorefractive materials,* Oxford series in optical and imaging science 11, Clarendon Press (1996).

[2] G Cook, C.J. Finnan, D.C. Jones, *High optical gain using counter propagating beams in iron and terbium-doped photorefractive lithium niobate*, Appl. Phys. B 68 (1999).

[3] R Ryf, G Montemezzani, P Gunter, *Long dark decay in highly sensitive Ce doped photorefractive KNbO3 crystals*, J.Opt A:Pure Appl. Opt. 3 (2001).

7. Conclusions and future work

7.1 Conclusions

It has been shown that inorganic photorefractive materials have the properties to fulfil the need for a frequency agile optical filter due to their ability to self-activate and host Bragg matched diffraction. The use of Ce:SBN promoted optimum energy transfer conditions for two beam coupling due to the dominance of diffusion within the material, and without the need for applied electric fields to promote charge transfer. The relatively thick inorganic window, much greater than 10 times the wavelength of light, allowed Bragg diffraction. In addition, the abundance of traps allowed a large range of beam intersection angles to be realised.

It was demonstrated for the first time that a liquid crystal layer can be used to dramatically enhance the gain from a Ce:SBN window. This hybridisation enabled peak gain coefficients of ~1600cm^{-1} to be reached compared to ~20cm^{-1} without the liquid crystal layer. This is the first time inorganic-organic hybrid photorefractives have been demonstrated. In addition, the hybridisation technique did not compromise the Bragg diffraction that could be realised with just a Ce:SBN window, the large range of beam intersection angles, the optimal energy transfer conditions, or need an applied electric field.

The underpinning physics, proposed in the literature, to describe the hybrid device physics was challenged due to strong experimental evidence for the presence of another symmetry dependent mechanism. The possible presence of another mechanism has been isolated to the Ce:SBN window rather than the liquid crystal layer through a combination of optical and atomic force microscope experiments. This formed an important step towards the full understanding of the physics within the inorganic photorefractive hybrid.

To achieve a faster inorganic-organic photorefractive hybrid device a different photorefractive material was chosen to influence the liquid crystal layer. The novel demonstration of an iron doped potassium niobate hybrid device has been described. The hybrid exhibited the same desirable attributes as the Ce:SBN hybrid. It was concluded that potassium niobate offers a good route towards increasing the response time of the device. This is important for our applications.

The implementation of a transmission grating optical filter can be complicated because the incident laser light has to be split into two, which requires additional optical components. To alleviate this issue a counter propagating geometry has been studied. Subsequently, a dual device comprising iron doped lithium niobate and iron doped potassium niobate has been demonstrated. By exploiting the large change in optical density of Fe:$LiNbO_3$ and the speed of $KNbO_3$ an enhanced response was achieved.

In summary, three novel photorefractive devices have been developed that are suitable for use as frequency agile optical filters and exhibit greater contrast ratios than previous passive photorefractive materials. The fundamental understanding in an inorganic photorefractive hybrid has been advanced.

7.2 Future work

To push the field forward further and promote further development of the materials and devices reported in this thesis, the research activities described below will be pursued.

7.2.1 Photorefractive hybrid optimisation

Though the inorganic-organic photorefractive hybrid devices developed in this thesis work well no attempt has been made to theoretically model the effect that different liquid crystal parameters have on the overall gain that can be achieved in such a device. The following parameters therefore need to be considered:

- Liquid crystal pre-tilt
- Dielectric permittivity
- Elastic constants
- Phase transition temperature from Nematic to isotropic
- Switching voltage

The influence of the reorientation of the liquid crystal molecules on the driving space charge field also needs to be considered. As the molecules re-orientate the space charge field will be modified. It is important to know how large and significant this modification is on the overall gain. Once predictions for optimal parameters have been made the existence of such a liquid crystal needs to be reviewed and/or the practicality of synthesising such a molecule would need to be considered.

The work in chapter 4 established that the absence of gain, in a Ce:SBN hybrid with the crystal c-axis orthogonal to the grating k-vector, is due to the properties of the Ce:SBN window. It is important to know whether or not the space charge field predicted by theory does actually exist for this orientation. Further electro force microscopy experiments are needed to establish this. Ideally, using the EFM technique reported in chapter 4, the space charge field should be measured during two-beam coupling with the crystal c-axis orthogonal to the grating k-vector and parallel to calibrate the result. If the space charge field is actually absent then charge screening effects should be considered and the diffusion coefficients for Ce:SBN measured.

7.2.2 Dual device assessment for fast optics

The measured change in optical density as a function of time for a dual lithium niobate and potassium niobate device was measured at only one f-number. A large f-number was chosen so that the focus was maintained throughout both materials in order to limit any ambiguity associated with the peak intensity in each material. The focal length required was dictated by the relatively thick pieces of crystal. Using thin crystals will extend the f-number range over which the change in optical density can be measured. Measuring the change in optical density as a function of f-number will be useful to assess what f-number system the dual device is suitable for.

7.2.3 Uniformity improvements

The graph shown below (figure 7.1) is the measured normalised gain across a Fe:$KNbO_3$ crystal aperture. The gain was measured at intervals of 2mm x 2mm squares that make up the full 20mm x 20mm window aperture. The two-beam coupling experimental set-up was identical to that described in chapters 2 and 5 except that the window was mounted on a translational stage.

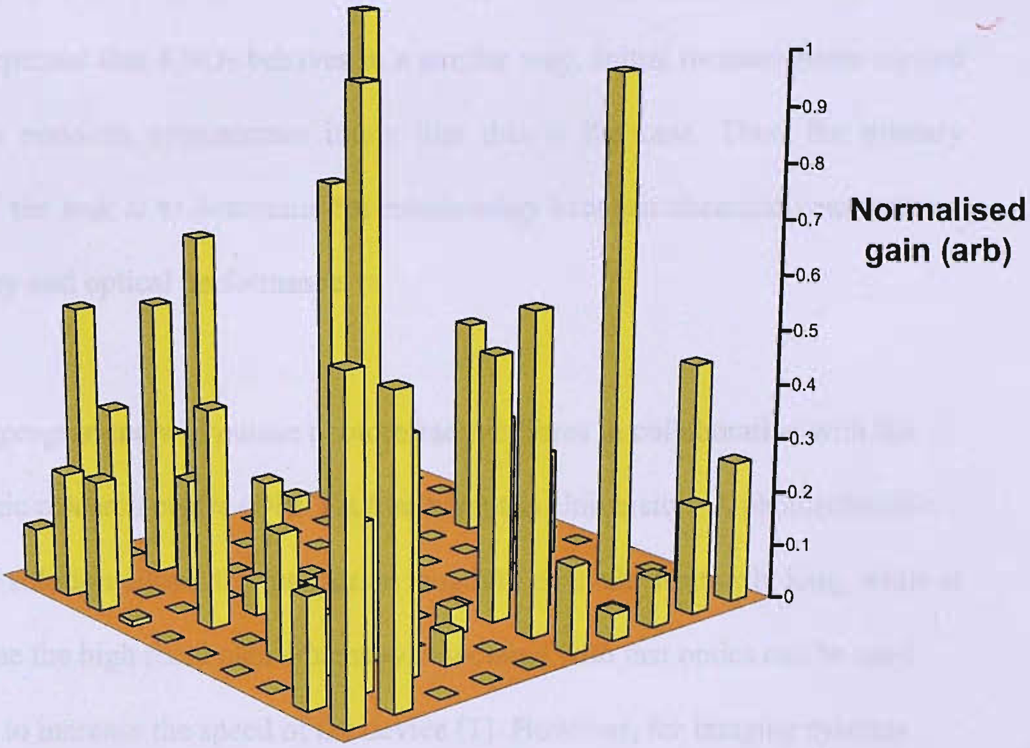

Figure 7.1. The normalised gain profile of a commercially grown Fe:$KNbO_3$ window.

As shown, the gain variance across the crystal window is large and in many places it's close to zero. For $KNbO_3$ devices to be of benefit this non uniformity must therefore be resolved. For this reason the author has initiated two research programmes; one that aims to improve the photorefractive performance uniformity across the aperture of a $KNbO_3$ window and another that will aim to improve photorefractive performance for fast optical systems.

The first programme is developing a novel chemical route for producing iron doped potassium niobate (Fe:KNO_3) crystals. Potassium niobate has been identified as a very promising photorefractive material. However, commercially available samples vary considerably in photorefractive performance. The photorefractive properties of lithium niobate (Fe:$LiNbO_3$) are known to vary with crystal stoichiometry and it would be expected that KNO_3 behaves in a similar way. Initial measurements carried out under a previous programmes imply that this is the case. Thus, the primary objective of the task is to determine the relationship between chemical composition, stoichiometry and optical performance.

The second programme will pursue photorefractive fibres in collaboration with the optoelectronic research centre (ORC) at Southampton University. A photorefractive optical fibre solution allows the interaction length to be made arbitrarily long, while at the same time the high focal plane intensity associated with fast optics can be used beneficially to increase the speed of the device [1]. However, for imaging systems single fibres are of little use and many such fibres are needed, arranged in a spatially coherent array. The optical imaging resolution is determined by the individual fibre sizes and by the array packing density, while the individual fibre diameter and the overall interaction length govern the ability to filter laser light. Unfortunately photorefractive crystal fibres are extremely difficult, costly, and time-consuming to produce [2]. It is impractical with present material production techniques to follow this route. The research is therefore following a strategy of incorporating active photorefractive material particles into a passive glass host. If successful, this route should allow photorefractive fibre production using established telecom fibre technologies, greatly easing the manufacture of devices and dramatically reducing the cost of ownership. Figure 7.2 illustrates the concept.

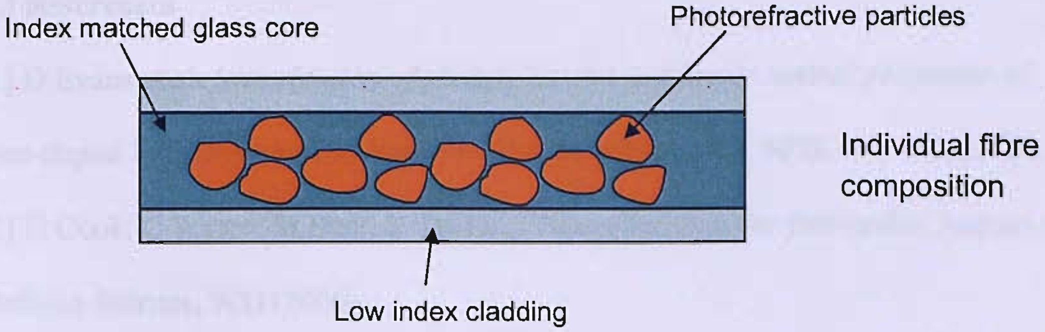

Figure 7.2. Photorefractive glass-particle matrix fibre concept.

A successful glass host material for Fe:LiNbO$_3$ must have the following properties:

- Higher refractive index than Fe:LiNbO$_3$ to guide light through the active particles
- Chemically compatible with Fe:LiNbO$_3$
- Lower melting point/viscosity so that the particles of Fe:LiNbO$_3$ do not dissolve in the host
- Lower conductivity so that the Fe:LiNbO$_3$ particles can be poled

In conclusion, a novel inorganic-organic photorefractive hybrid concept has been demonstrated experimentally using two different inorganic windows, Ce:SBN and Fe:KNbO$_3$. This is an important contribution to the field of photorefractives as this technique has been shown to provide a means of significantly increasing the gain from an inorganic crystal whilst still harnessing the attractive attributes associated with inorganic materials. For many applications, increased gain is always advantageous and sought after. In addition, the separate demonstration of this hybridisation with two different inorganic materials implies that the technique will work with any inorganic material that can support both a diffraction grating and space charge field that are out of phase with an optical interference pattern generated by two beam coupling. This discovery paves the way for tailoring the performance of future inorganic-organic hybrid devices by careful material choice.

7.3 References

[1] D Evans et al. *Investigation of photorefractive nonlinear optical properties of iron-doped lithium niobate in bulk and fiber configurations,* SPIE vol. 4462, 2002.

[2] G Cook, C Wyres, M Deer, L Taylor, *Photorefractives for fast optics*, Journal of Defence Science, **9(2)** (2004).

Appendix: List of Publications

M Deer, *Demonstration of an Fe doped KNbO3 photorefractive hybrid*, Applied Physics Letters, **88**, 254107 (2006).

G Cook, C Wyres, M Deer, L Taylor, *Photorefractives for fast optics*, Journal of Defence Science, **9(2)** (2004).

G. Cook, C Wyres, M Deer, D Jones, *Hybrid organic-inorganic photorefractives*, SPIE, 5213, (2003). **An invited paper that was edited/reviewed by I.C. Khoo.**

Conference presentations

M Deer, *Photorefractives for Fast Optics*, selected to present at Britain's Top Younger Scientists, Engineers and Technologists competition, House of Commons (2006).

M Deer, *Photorefractives for Fast Optics*, invited international photorefractive workshop, South Carolina (2005).

M Deer, *Hybrid organic-inorganic photorefractives*, invited international photorefractive workshop, Florida (2004).

M Deer, *Hybrid organic-inorganic photorefractives*, IOP meeting, Young researchers in optics, London (2003).